THESE DE DOCTORAT

Soutenue à Aix-Marseille Université
le 30 Mars 2022 par

Julio José BALBIN ARIAS

Investigation of the dependency of separatrix density of tokamaks as a function of engineering parameters

Discipline
Sciences pour l'Ingénieur

Speciality
Fluids Physics and Mechanics

Doctoral School 353
Sciences pour l'Ingénieur: Mécanique, Physique, Micro et Nanoélectronique

Laboratory
Institut de Recherche sur la Fusion par confinement Magnétique
CEA-Cadarache, 13108
Saint-Paul-lez-Durance, France

Composition du jury

Prof. Giuseppe CALABRO Università de la Tuscia	Rapporteur
Prof. Roman ZAGORSKI Narodowe Centrum Badan Jadrowych (NCBJ)	Rapporteur
Dra. Francesca TURCO Columbia University General Atomics	Examinatrice
Prof. Assoc. Paolo INNOCENTE CNR - Consorzio RFX	Examinateur
Prof. Eric SERRE CNRS	Président du jury
Dr. Nicolas Fedorczak IRFM - CEA	Examinateur
Dr. Guido CIRAOLO IRFM - CEA	Directeur de thèse
Dr. Jerome BUCALOSSI IRFM - CEA	Co-Directeur de thèse

Affidavit

I, undersigned, Julio Balbin Arias, hereby declare that the work presented in this manuscript is my own work, carried out under the scientific direction of Dr. Guido Ciraolo and Dr. Jerome Bucalossi, in accordance with the principles of honesty, integrity and responsibility inherent to the research mission. The research work and the writing of this manuscript have been carried out in compliance with both the french national charter for Research Integrity and the Aix-Marseille University charter on the fight against plagiarism.

This work has not been submitted previously either in this country or in another country in the same or in a similar version to any other examination body.

Aix-En-Provence, 30th March 2022.



Cette œuvre est mise à disposition selon les termes de la Licence Creative Commons Attribution - Pas d'Utilisation Commerciale - Pas de Modification 4.0 International.

Dedicado a mi madre, Maria.

"Caminante, son tus huellas
el camino y nada más;
Caminante, no hay camino,
se hace camino al andar.
Al andar se hace el camino,
y al volver la vista atrás
se ve la senda que nunca
se ha de volver a pisar.
Caminante no hay camino
sino estelas en la mar."

Antonio Machado

Acknowledgements

Comenzaré agradeciendo a mi madre por no haberme desamparado nunca y haberme guiado y querido siempre desde que era un niño, sabemos lo que hemos pasado y sólo queda la huella del camino que decidimos superar. También mencionar a mis hermanos, Claudia y Sebastian, y lo mucho que los amo, y de los cuales he recibido un apoyo incondicional.

I would like to start by thanking my supervisors Dr. Guido Ciraolo and Dr. Jerome Bucalossi because they changed my life by choosing me and gave me a unique opportunity, I can never thank them enough for what they did for me. In spite of all the adversities of different kinds that were present from the beginning to the end, they always supported me and I will be infinitely grateful to them. Also I would like to thank Valerie Icard for speaking to me in Spanish and always treating me in a very understanding and kind way, I was able to feel comforted even if it was just for a few minutes when I was feeling bad, and how not to thank my friend Julien Denis who received me in an incredible way and understood me from the first minute, he understood me and supported me, maybe I have not said him it before, but I admire him a lot and in my moments of weakness I have been inspired by him to continue.

Likewise I would like to give a special greeting to Dr. Humberto Torreblanca because he gave me the opportunity to start a first experience in fusion during my stay in DIII-D and he has always guided me selflessly, he is like a father in the path of fusion. I would also like to thank Dr. Francesca Turco who helped me learn about CEA and IRFM, and extend my thanks and greetings to the entire DIII-D team for being wonderful while I shared with

them. I would also like to thank Claudia and Juan Fernando for the time shared in San Diego and the experiences that followed, which are memories that I carry in my mind and heart.

I would like to thank all the people who have given me from an advice to a talk in order to improve my thesis work, the JET team, the TCV team with an outstanding salute to Olivier and Davide, Dr. Jamie Gunn and Dr. Christophe Guillemaut for supporting me in the analysis of the Langmuir probes, all the IRFM staff because they were always very polite and kind.

I would like to salute all my colleagues with whom I have shared experiences in different ways, Elisabetta, Serafina, Valeria, Jorge, Samuele, Elias, Mathieu, Rui, Raffaele, Alberto, Matteo, Hao, Giacomo, but I would like to make a parenthesis to highlight my office colleagues Eléonore and Manuel for simply being fantastic colleagues and friends. In addition, I would like to extend my greetings outside IRFM to my friends from the Spanish-language lunches, Alex, Francisco, Juan, Felipe, Giorgio, and especially Bernardo with whom I shared so much and with whom I was able to avoid madness during our conversations in the middle of the pandemic.

No puedo olvidarme de saludar a mi abuela, tíos y a mis dos hermosos sobrinos que pronto tendré el privilegio de conocer. Destaco el rol que mi primo, Deiver, ha tenido al compartir junto a mi este último año del doctorado y con el cual he vivido experiencias reconfortantes.

Quiero destacar a Liz, mi compañera, con la cual intentamos de manera valiente traspasar la barrera de la distancia y el tiempo.

The road to my dreams and goals has been long and challenging, but as I reach this first

step I can contemplate the beautiful road I have traveled and all that I have been able to learn, for which I would never change my decisions or the people who have helped me to achieve my goals.

To Finish, with this thesis I hope to contribute with my tiny grain of sand in this immense desert of knowledge.

Abstract

A viable magnetic fusion power plant has to combine very high plasma density and temperature in the core region, in order to maximize fusion reactions, with cold plasma conditions in the peripheral region compatible with long life expectancy of plasma-facing components. In this thesis, we examine this crucial issue for magnetic fusion research by adopting an approach based on the analysis of a large set of experimental data on H-mode plasmas from the JET and TCV tokamaks, in order to obtain a scaling law for the relationship between top pedestal density and separatrix density as a function of engineering parameters. The choice to examine this density ratio is motivated by the fact that, on the one hand, the density at the top pedestal is an indicator of core confinement and device performance, and on the other hand, the separatrix density has a strong impact on divertor conditions, indicating whether safe conditions for divertor targets are achievable or not.

After a brief review of the main parameters of the JET and TCV tokamaks and the diagnostics considered for this study, the data analysis is presented, starting from the method developed for the determination of the separatrix density. As it is well known, this is a very difficult task and many approaches are used to determine this density, which in fact requires locating the position of the separatrix in the measured radial density profile. The method that is developed in this study is based on power balance considerations. This method relies on the choice of the heat flux expression and non-negligible differences in the separatrix densities are observed depending on this choice. In order to estimate the impact on the position of the separatrix and thus on the separatrix density, the power balance method was applied

to numerical simulations obtained with the SOLEDGE-EIRENE [1, 2] transport code for a JET configuration considering several heat flux expressions. The position of the separatrix obtained with the power balance method is compared to the known position from the mesh-grid built on a given magnetic equilibrium and used for running the simulation. With this type of verification, it is shown that for typical JET H-mode discharges considered in this study, the power balance method using a kinetically corrected Spitzer expression works very well.

In a second step, the analysis of JET H-mode discharges considered for this work is detailed. A first analysis of the dataset shows that some engineering parameters cannot be considered as independent for our analysis because many discharges were performed considering the same typical values of these parameters, such as the toroidal magnetic field and the plasma current. Thus, two main engineering parameters are first identified and will be used for the scaling law on the ratio of the separatrix density to the top pedestal one, namely the plasma current I_P and the total injected power P_{TOTAL}. This first scaling law seems to predict the experimental data quite well for low and medium values of the separatrix density, while at high density a strong discrepancy appears. In order to get further insight on such behavior the discharges were analyzed in terms of divertor magnetic configuration. A clear difference is observed between experiments with a corner-corner divertor magnetic configuration compared to the horizontal-vertical ones or vertical-vertical ones. This result suggests the introduction a parameter taking into account the quality of confinement. In this way, a better agreement between predictions and experimental results is obtained for both low and high-density values. Finally, the same type of study is performed on TCV and a scaling law taking into account both devices is derived.

Résumé

Une centrale de fusion magnétique viable doit combiner une densité et une température de plasma très élevées dans la région centrale, afin de maximiser les réactions de fusion, avec des conditions de plasma froid dans la région périphérique compatibles avec une longue durée de vie des composants en contact avec le plasma. Dans cette thèse, nous examinons cette question cruciale pour la recherche sur la fusion magnétique en adoptant une approche basée sur l'analyse d'un large ensemble de données expérimentales sur les plasmas en mode H des tokamaks JET et TCV. Nous voulons déterminer une loi d'échelle en fonction des paramètres ingénieur pour la relation entre la densité piédestal, i.e. en haut de la barrière externe qui caractérise le mode H, et la densité séparatrice, c'est-à-dire dans la zone du plan médian équatorial, au point de passage entre lignes magnétiques fermées et ouvertes. Le choix d'examiner ce rapport de densité est motivé par le fait que, d'une part, la densité piédestal est un indicateur de la qualité du confinement du plasma central et des performances du dispositif, et d'autre part, la densité séparatrice a un fort impact sur les conditions du divertor, indiquant si des conditions sûres pour les cibles du divertor sont réalisables ou non.

Après un bref rappel des principaux paramètres des tokamaks JET et TCV et des diagnostics considérés pour cette étude, l'analyse des données est présentée, en commençant par la méthode développée pour la détermination de la densité à la séparatrice. Comme on le sait, il s'agit d'une tâche très difficile et de nombreuses approches sont utilisées pour déterminer cette densité, qui nécessite en fait de localiser la position de la séparatrice dans le profil de densité radial mesuré. La méthode qui est développée dans cette étude est basée sur des

considérations d'équilibre de puissance. Cette méthode repose sur le choix de l'expression du flux thermique et des différences non négligeables dans les densités des séparatrices sont observées en fonction de ce choix. Afin d'estimer l'impact sur la position de la séparatrice et donc sur la densité de la séparatrice, la méthode du bilan de puissance a été appliquée à des simulations numériques obtenues avec le code de transport SOLEDGE-EIRENE [1, 3] pour une configuration JET en considérant plusieurs expressions de flux de chaleur. La position de la séparatrice obtenue avec la méthode du bilan de puissance est comparée à la position connue de la grille de maillage construite sur un équilibre magnétique donné et utilisée pour exécuter la simulation. Avec ce type de vérification, il est démontré que pour les décharges typiques en mode H du JET considérées dans cette étude, la méthode du bilan de puissance utilisant une expression de Spitzer corrigée cinétiquement fonctionne très bien.

Dans un deuxième temps, l'analyse des décharges en mode H du JET considérées dans ce travail est détaillée. Une première analyse de l'ensemble des données montre que certains paramètres techniques ne peuvent pas être considérés comme indépendants pour notre analyse car de nombreuses décharges ont été réalisées en considérant les mêmes valeurs typiques de ces paramètres, tels que le champ magnétique toroïdal et le courant plasma. Ainsi, deux paramètres techniques principaux sont d'abord identifiés et seront utilisés pour la loi d'échelle sur le rapport entre la densité de la séparatrice et celle du socle supérieur, à savoir le courant plasma I_P et la puissance totale injectée P_{TOTAL}. Cette première loi d'échelle semble prédire assez bien les données expérimentales pour des valeurs faibles et moyennes de la densité de la séparatrice, alors qu'une forte divergence apparaît pour une densité élevée. Afin de mieux comprendre ce comportement, les décharges ont été analysées en fonction de la configuration magnétique du divertor. Une nette différence est observée entre les expériences avec une configuration magnétique du divertor en coin par rapport aux configurations horizontales-verticales ou verticales-verticales. Ce résultat suggère l'introduction d'un paramètre prenant en compte la qualité du confinement. De cette manière, un meilleur

accord entre les prédictions et les résultats expérimentaux est obtenu pour les valeurs de basse et haute densité. Enfin, le même type d'étude est réalisé sur le TCV et une loi d'échelle prenant en compte les deux dispositifs est dérivée.

Contents

List of Figures **xviii**

List of Tables **xxiv**

1 Introduction **2**

2 Transport in edge tokamak plasmas **5**

2.1 Braginskii fluid equations 5

2.1.1 Collision operator 7

2.1.2 Conservation of momentum and energy 8

2.1.3 Fluid Equations 10

2.2 From Braginskii equations to the two-point model 15

2.2.1 Conservative form of the momentum equation 16

2.2.2 Heat transfer inside the SOL 18

2.2.3 Density regimes 21

2.2.4 The sheath-limited regime 23

2.2.5 The high-recycling regime 24

2.2.6 The transition between the sheath-limited and the high-recycling regime 25

2.3 The modified Two Point Model 28

2.3.1 Separatrix temperature determination using the Two Point Model . . 30

2.4 Pedestal region and edge barrier in H-mode 33

2.4.1 High confinement regime and ELMs 35

2.4.2 Quality of confinement and H98 factor 37

3 Experimental setup: the JET and TCV tokamaks 38

3.1 Heating system and principles of Neutral Beam Injection 41

3.1.1 Neutral Beam in JET 42

3.1.2 Neutral Beam in TCV 43

3.2 High-resolution Thomson scattering 44

3.2.1 Principles 44

3.2.2 HRTS at JET 46

3.2.3 HRTS at TCV 48

3.3 Gas puffing and divertor electric probes in JET 50

4 Determination of the separatrix position 54

4.1 Determination of the separatrix position at outer mid-plane using a power balance method 54

4.1.1 Application to a JET discharge 56

4.1.2 Parallel heat flux expressions and verification on a SOLEDGE2D numerical simulation 58

5 Investigation of the dependency of midplane separatrix density in H-mode as a function of engineering parameters for JET tokamak 63

5.1 JET dataset 64

5.2 Determination of a scaling law 69

5.2.1 Further investigation of dataset and dependencies from engineering and plasma parameters 71

5.3 JET dataset analysis with respect to divertor magnetic configuration 77

5.3.1 Analysis of plasma discharges in Corner-Corner divertor magnetic configuration 79

5.3.2 Analysis of plasma discharges in Vertical-Horizontal divertor magnetic configuration . . . 81
5.3.3 Separatrix density and temperature analysis in terms of divertor magnetic configurations . . . 83
5.4 JET dataset analysis under H_{98} parameter . . . 85
5.5 Scaling law taking into account the H_{98} parameter . . . 88
5.6 Two point model comparison . . . 90
5.7 Investigation of density behavior in a series of SolEdge 2D transport code simulations . . . 94
5.7.1 P_{SOl} scan on S2D . . . 94
5.7.2 Extra parameters variation on S2D . . . 98

6 Interpretation of H-mode dataset for TCV tokamak 100
6.1 TCV discharges . . . 100
6.1.1 TCV discharges . . . 103
6.1.2 Global scaling law: TCV + JET . . . 109

7 Summary and Conclusions 111

A Drude theory of thermal conductivity applied to plasma 116
A.1 Electric field by effect of gradient of temperature - (Seebeck effect-Drude model) 118
A.2 Relaxation Processes . . . 119
A.2.1 Momentum loss . . . 119
A.2.2 Thermal distribution collisions . . . 120
A.2.3 e $\Longrightarrow$ i collisions . . . 120

Bibliography 123

List of Figures

2.1 Two-point model illustration. 30

2.2 Radial profiles of (a) electron temperature from core plasma Thomson scattering data (triangles and x-symbols), and electron cyclotron emission (ECE, horizontal bars), (b) ion temperature from CHERS, and (c) electron density from core plasma Thomson scattering in L-mode (875 ms, dashed line) and H-mode (1150 ms, solid line). Figure from [L. Schmitz et al. Nucl. Fusion, 52, 2012.]. This two regimes might be interpreted like two bifurcated states of plasma depending of the operation conditions 36

3.1 Neutral Beam Injection mechanism 42

3.2 Neutral Beam scheme 43

3.3 Neutral Beam scheme in TCV 44

3.4 Neutral Beam scheme in JET 47

3.5 HRTS in TCV 49

4.1 Electron temperature and density profiles for JET pulse number 89248. . . . 56

4.2 Electron temperature (left panel) and density (right panel) poloidal profiles computed with SOLEDGE2D simulations for JPN94210-1040. The separatrix is indicated with dotted black curve 60

4.3 Electron temperature (left panel) and density (right panel) poloidal profiles computed with SOLEDGE2D simulations for JPN94210-1060. The separatrix is indicated with dotted black curve 61

4.4 Separatrix positions given by the different heat flux models on electron temperature and density profile for JET pulse number 94210 with conditions of modeling 1040. 62

4.5 Separatrix positions given by the different heat flux models on electron temperature and density profile for JET pulse number 94210 with conditions of modeling 1060. 62

5.1 Left panel: dataset plotted in the $I_P\,(MA)$ - $B_T\,(T)$ plane. One can observe that in the largest part of the discharges the liner relationship between B_T and I_p, indicating an "operational preference" over the dataset. Right panel: dataset plotted in the $I_P\,(MA)$ - $P_{TOTAL}\,(MW)$ plane indicating that the plane is well covered with the and allowing for using these two enginnering parameters in the scaling law 65

5.2 (Left panel: Plot of the dataset in terms of top pedestal density $n_{e,PED}$ as a function of I_P, displaying an impact of I_P on the quality of confinement. Right panel: Plot of the dataset in terms of $n_{e,PED}$ as a function of the total injected power P_{TOTAL}, showing an overall liner relationship between these two quantities 65

5.3 JET dataset under consideration plotted in terms of electron separatrix density as a function of pedestal density. The dataset is enclosed by two limits set like $30\% \leq n_{e,SEP} \leq 80\%$. 66

5.4 JET dataset under consideration plotted in terms of electron separatrix temperature as a function of pedestal density. In the figure is pointed out in red dashed line the averaged electron separatrix temperature, $140\,eV$ 67

5.5 JET dataset under consideration plotted in terms of electron separatrix temperature as a function of separatrix density. The range of $T_{e,SEP}$ is reduced for $n_{e,SEP} \geq 3.0 \times 10^{19}\mathrm{m}^{-3}$. 68

5.6 Comparison of experimental $n_{e,SEP}$ (determined using power balance method), and $n_{e,SEP}$ provided by the scaling law referenced in equation 5.1. There are values for, $n_{e,SEP}(\text{DATA}) \geq 5 \times 10^{19}\text{m}^{-3}$, out of trend that can be affected to unconsidered parameters. 70

5.7 The framework of I_P versus B_T is used like background to colored the data as function of λ_q and P_{RAD}, thus homogeneous subsets can be identified like those pointed out as 1st subset and 2nd subset. These two subsets can be employed to observe the evolution of magnitud like $n_{e,SEP}$, e.g., as function of unconsidered parameter like P_{TOTAL}. 71

5.8 The framework of I_P versus B_T with a 3D perspective. 72

5.9 This is a representation of one subset $I_P - B_T$ with small variations for B_T and I_P. The coloring of P_{SOL} allows to split this subset in two new sets where the range of P_{SOL} is wide. 73

5.10 These two graphics show an increasing of $n_{e,SEP}$ while P_{SOL} increases and show small variations of $T_{e,SEP}$ respect to P_{SOL}. 73

5.11 These two graphics evidence that $n_{e,SEP}$ and $T_{e,SEP}$ increase while P_{SOL} is incresing. There are $T_{e,SEP}$ values, $\geq 100\,eV$ and $\leq 140\,eV$, for which P_{SOL} takes low and high values. 74

5.12 This is a representation of a subset where I_P and B_T have been reduced in their ranges keeping a wide range of P_{SOL}. 75

5.13 These two graphics show an increasing $n_{e,SEP}$ and $T_{e,SEP}$ while P_{SOL} has increased holding a wide range of P_{SOL}. 76

5.14 Poloidal section of JET. The Corner-corner (C-C), Vertical-Horizontal (VT-5) and vertical-vertical magnetic configurations are represented with green, blue and pink dashed lines respectively, referring to three particular discharges as mentioned in the inset of the figure. Horizontal black line crossing bidimensional wall profile (blue solid line) represents midplane Thomson scattering diagnostic; red squares in the divertor region represent Langmuir probes. . . 78

5.15 The $n_{e,SEP}$ as a function of $n_{e,PED}$ with classification with respect to three $I_P(MA)$ in Corner-Corner configuration. 79

5.16 The $n_{e,SEP}$ as a function of $n_{e,PED}$ with classification for $B_T(T)$ in Corner-Corner configuration. 80

5.17 The $n_{e,SEP}$ as a function of $n_{e,PED}$ with classification for $P_{SOL}(MW)$ in Corner-Corner configuration. 80

5.18 The $n_{e,SEP}$ as a function of $n_{e,PED}$ with classification for $B_T(T)$ in Vertical-Horizontal configuration. 81

5.19 The $n_{e,SEP}$ as a function of $n_{e,PED}$ with classification for $I_P(MA)$ in Vertical-Horizontal configuration. 82

5.20 The $n_{e,SEP}$ as a function of $n_{e,PED}$ limited by $n_{e,SEP}/n_{e,SEP}|_{min}$ (upper dashed black line) and $n_{e,SEP}/n_{e,SEP}|_{max}$ (lower dashed black line). 83

5.21 The $n_{e,SEP}$ as a function of $n_{e,PED}$ limited by $n_{e,SEP}/n_{e,SEP}|_{min}$ (upper dashed black line) and $n_{e,SEP}/n_{e,SEP}|_{max}$ (lower dashed black line). The internal dashed lines represent the average of each one of the sub-datasets correspondingly to Corner-Corner, Vertical-Horizontal and Vertical-Vertical configuration. 84

5.22 $T_{e,SEP}$ as a function of $n_{e,PED}$. 84

5.23 H_{98} as a function of $n_{e,SEP}$. 86

5.24 H_{98} as a function of $n_{e,PED}$. 86

5.25 H_{98} as a function of $n_{e,SEP}/n_{e,PED}$. 87

5.26 The experimental separatrix density versus the expectation from scaling law of equation 5.2. The dashed line represents 89% of exected value. 89
5.27 $T_{e,SEP}$ as a function of $n_{e,SEP}$ and the TPM comparison for C-C magnetic configuration. 90
5.28 $T_{e,SEP}$ as a function of $n_{e,SEP}$ and the TPM comparison for VT-5 magnetic configuration. 91
5.29 $T_{e,SEP}$ as a function of $n_{e,SEP}$ and the TPM comparison for V-V magnetic configuration. 91
5.30 Separatrix positions given by power balance method for JPN94210-1040. . . 94
5.31 Electron temperature and density poloidal profiles for JPN94210-1040. . . . 95
5.32 Separatrix positions given by power balance method for JPN94210-1050. . . 95
5.33 Electron temperature and density poloidal profiles for JPN94210-1050. . . . 96
5.34 Separatrix positions given by power balance method for JPN94210-1060. . . 96
5.35 Electron temperature and density poloidal profiles for JPN94210-1060. . . . 97

6.1 TCV pulse number 61850 is displaying a H-mode regime on the profiles of electron density and temperature. The separatrix position provided by the magnetic reconstruction, solid vertical line, and that one by power balance method, dotted red line, are referenced on this graphic. 101
6.2 TCV pulse number 61932 is displaying a H-mode regime on the profiles of electron density and temperature. The separatrix position provided by the magnetic reconstruction, solid vertical line, and that one by power balance method, dotted red line, are referenced on this graphic. 102
6.3 The average of electron separatrix is $80\,eV$ and for $n_{e,PED} \geq 6.0 \times 10^{19}\mathrm{m}^{-3}$ the range of $T_{e,SEP}$ is reduced. 103
6.4 Total TCV dataset for eletron separatrix and pedestal densities. The dataset is enclosed by two limits set like $19\% \geq n_{e,SEP}/n_{e,PED} \geq 62\%$. 104
6.5 The $n_{e,SEP}$ displays a faint but clear decreasing by effect of an incresing of I_P. 105

6.6 (LEFT) Almost constant relation between $B_T\,(T)$ and $I_P\,(MA)$, set with some pulses working with $B_T = 1.325$T. (RIGHT) Growing trend between $P_{TOTAL}\,(MW)$ and $I_P\,(MA)$ remarking that both factors can increase effectiveness of fusion reaction and consequently an increasing of confinement quality but with some pulses within region $[300\,\mathrm{KA}, 380\,\mathrm{KA}]$ that might represents pulses operating under $B_T = 1.325\,\mathrm{T}$. 106

6.7 (LEFT) Growing relation between $n_{e,PED}$ and I_P, displaying a prolific impact of I_P on the quality of confinement. (RIGHT) A direct relation of $n_{e,PED}$ and P_{TOTAL} exposing a beneficial effect of increasing P_{TOTAL} on quality of confinement but some pulses for high P_{TOTAL}, $\in [2.0\,\mathrm{MW}, 2.5\,\mathrm{MW}]$, might be associated to $B_T = 1.325$T. 106

6.8 The experimental separatrix density versus the expectation from scaling law of equation in 6.1. The dashed line represents 72% of the expected value. . . 107

6.9 The $T_{e,SEP}$ increases while P_{SOL} increases and for low values of P_{SOL}, $\in [0.31\,\mathrm{MW}, 0.89\,\mathrm{MW}]$, then $T_{e,SEP}$ follows the trend leads by two-point model decreasing $T_{e,SEP}$ by effect of an increasing $n_{e,SEP}$. 108

6.10 The correspondence between the separatrix electron density from scaling law and the empirical one show an acceptable agreement with some points for higher density out of trend that can be related with closer to detached density regimes being mis-described by the Kinetic-corrected Spitzer expression for the parallel heat flux. 110

List of Tables

2.1 Values set for two-pint model illustration. 31

3.1 Technical Values of JET tokamak 39

3.2 Technical Values of TCV tokamak 40

3.3 Langmuir probes summary in JET 51

4.1 Comparison between the electron temperature and density at the separatrix position estimated with the power balance method using the kinetically-corrected heat flux expression and the separatrix position given by soledge meshgrid, indicated with (S2D). 59

5.1 Averaged values for the two-point model comparison in C-C configuration. . 71

5.2 Averaged values for the two-point model comparison in C-C configuration. . 72

5.3 Averaged values for the two-point model comparison in C-C configuration. . 90

5.4 Averaged values for the two-point model comparison in V-V configuration. . 92

5.5 Summary of simulated pulses in SOLEDGE2D based on JPN 94210 97

5.6 Transition between JPN9420-1040 to JPN9420-1050. 97

5.7 Transition between JPN9420-1040 to JPN9420-1060. 98

5.8 Transition between JPN9420-1050 to JPN9420-1070. 98

5.9 Transition between JPN9420-1060 to JPN9420-1080. 98

5.10 Transition between JPN9420-1050 to JPN9420-1090. 99

6.1 Summary of parameters for the determination of the radial separatrix position on TCV pulses 61850 and 61932. The resulting separatrix positions are shown in figures 6.1 and 6.2. 101

Chapter 1

Introduction

A viable magnetic fusion power plant has to combine very high plasma density and temperature in the core region, in order to maximize fusion reactions, with cold plasma conditions in the peripheral region compatible with long life expectancy of plasma-facing components. More precisely, as stated by the Lawson criterion, three quantities have to be maximized for achieving burning plasmas in the hot core region of the device, i.e. plasma density, plasma temperature and energy confinement time [4]. In that respect and since the beginning of fusion plasma research a strong effort is devoted to improve our understating and control of core plasma behavior. In particular a lot of studies focus on the mechanisms at the origin of turbulent transport, one of the main responsible for the degradation of plasma energy confinement time, still too short for achieving burning plasmas in today machines. On the other side, the technological limits of wall materials in contact with the plasma at the boundary of the device impose a maximum heat flux impacting the plasma facing components of about 10 $\mathrm{MW/m^2}$ [4, 5] in steady-state conditions, and with very low plasma temperatures (few eV). For this reason, many experimental, numerical and theoretical studies are ongoing to find the most efficient way for controlling the power loads on the plasma facing components, keeping at the same time the core region as hotter as possible. In this manuscript, we try to give a contribution in this direction considering an approach based on the analysis of a large experimental dataset of H-mode plasmas coming from JET and TCV tokamaks, in order to obtain a scaling law of the relationship between top pedestal density and separatrix density

as a function of engineering parameters.

Before stepping into the analysis of JET and TCV data, we present in chapter two and three some element of context useful for the following part of the manuscript. In chapter two we recall the derivation of 3D fluid Braginskii equations [6, 7, 8, 9] starting from the kinetic ones. Then we present quite extensively the so-called two-point model [10], a 0-D model very useful for the global understating of plasma behavior in the edge region of a tokamak. In particular, we present the two limit cases of hot and cold scrape off layer (the boundary layer caracterised by the interaction of the plasma with the wall) and how from the model we can obtain predictions on target temperature and density with respect to upstream quantities. A more general relationship between temperature and density at the upstream position is also presented in function of the input power, being this result of interest for the successive experimental study [11].

In chapter three, we present the experimental setup of JET and TCV, the two devices we have considered for the analysis of H-mode plasmas. We present first the principles of neutral beam injection (NBI) heating system and then we detail how it is implemented in JET and TCV. We also give some details on the gas puffing system and the Langmuir probe system used for measurements into the divertor region. A section is devoted to the presentation of the main diagnostic system we have used for our studies, i.e. the High resolution Thomson scattering system. This diagnostics provides plasma density and temperature profiles in the pedestal region at the outer midplane, from which we can determine the density at the top of the pedestal and at the separatrix.

The determination of the separatrix position is a very difficult task and many approached are used to determine it [12, 13, 14, 15, 16, 17, 18]. In chapter four we vriefly recall the standard method based on magnetic measurements and numerical solvers on Grad-Shafranov equation. Because this method can produce large error bars on the determination of the separatrix, we present a second method based on power balance considerations. This method relies on the heat flux expression that is taken into account and this choice can produce

non-negligible differences in the estimation of the separatrix position. In order to have a sort of validation of the heat flux expression that is considered in the analysis of the experimental data, we apply the power balance method to numerical simulations obtained with the transport code SOLEDGE-EIRENE [1, 2, 3] for a JET configuration.

In chapter five we focus on the study of H-mode plasmas in JET-ILW tokamak, matching the conditions of core, outer mid-plane, and divertor zone for reaching a reliable scaling law to propose an optimal scenario. The core and outer mid-plane during an H-mode operation are linked through pedestal zone. One can consider top pedestal density, $n_{e,PED}$, and electron separatrix density at the outer mid-plane, $n_{e,SEP}$, respectively as parameters representative because the first is a good indicator for the quality of core confinement and the second gives an idea of divertor conditions and heat flux flowing towards the targets once the input power is known. Providing a scaling law with $n_{e,PED}$ and $n_{e,SEP}$, is then of particular interest because it embeds information both on core confinement and divertor conditions. Furthermore, we will consider the dataset of JET-ILW during H-mode plasmas analyzing the impact of different magnetic configurations, and trying to include this information, if relevant, into the scaling law. The engineering parameters we will consider are the main ones, e.g. toroidal magnetic field, plasma current, input power and H98.

In chapter six, we perform the same kind of study as in chapter five but on TCV tokamak. The choice of investigating H-mode plasmas in JET and TCV is motivated from the fact that will allow us to have information on scaling law both from a large device as JET as well as from a medium size tokamak as TCV. In other terms, the dataset will cover a large range of engineering parameters, providing hopefully a more general scaling law.

Chapter 2

Transport in edge tokamak plasmas

In this chapter first we briefly recall the derivation from kinetic equations of Braginskii fluid equations for plasma transport. These 3D equations for density, momentum and energy are widely used for describing plasma transport at the edge of tokmak devices. They are then simplified using a large set of assumptions in order to obtain the so called two-point model, which is described in details and it will be used further in the manuscript to give an insigth to experimental results and their interpretation. In the final part of the chapter we describe the pedestal region at the edge of tokamak plasma in the high-confinement regime and the H_{98} parameter for the classification of the quality of the confinement.

2.1 Braginskii fluid equations

As a starting point we introduce few concepts that are used in the kinetic approach. Each particle can be represented as a point in six-dimensional phase space $\left(\overline{\mathbf{r}}, \overline{\mathbf{v}}\right)$ [6, 7, 19, 20, 8, 9]. In order to describe a very large number of particles a possible choice is to use the distribution function, defined as:

- $f_a\left(\overline{\mathbf{r}}, \overline{\mathbf{v}}; t\right)$: distribution function of a particle species 'a' is defined as the number of particles of that species per unit volume in phase space near the point $\overline{\mathbf{z}} = \left(\overline{\mathbf{r}}, \overline{\mathbf{v}}\right)$ at time t.

- $f_a\left(\overline{\mathbf{r}}, \overline{\mathbf{v}}; t\right) d^3\mathbf{r} d^3\mathbf{v}$: is the number of particles in the volume element $d^3\mathbf{r} d^3\mathbf{v}$ surrounding

the point $\big(\overline{\mathbf{r}}, \overline{\mathbf{v}}\big)$.

The number density of particles (in real space) is given by the integral of the distribution function over the velocity space:

$$\int f_a\big(\overline{\mathbf{r}}, \overline{\mathbf{v}}; t\big) d^3\mathbf{v} = n_a\big(\overline{\mathbf{r}}; t\big) \tag{2.1}$$

The equations of motion are:

$$\begin{aligned} \dot{\overline{\mathbf{r}}} &= \overline{\mathbf{v}} \\ \dot{\overline{\mathbf{v}}} &= \frac{e_a}{m_a}\big(\overline{\mathbf{E}} + \overline{\mathbf{v}} \times \overline{\mathbf{B}}\big) \end{aligned} \tag{2.2}$$

The flow velocity of particles in phase space can thus be represented by $\dot{\overline{\mathbf{z}}} = \big(\dot{\overline{\mathbf{r}}}, \dot{\overline{\mathbf{v}}}\big)$ [7, 9]:

$$\frac{\partial f_a}{\partial t} + \frac{\partial}{\partial \overline{z}}\big(\dot{\overline{z}} f_a\big) = 0, \qquad \text{which is the Liouville expression where} \tag{2.3}$$

$$\begin{aligned} \overline{\nabla}_z &= \begin{pmatrix} \overline{\nabla}_r \\ \overline{\nabla}_v \end{pmatrix} \\ \dot{\overline{z}} &= \begin{pmatrix} \overline{\mathrm{v}} \\ \frac{e_a}{m_a}\big(\overline{E} + \overline{\mathrm{v}} \times \overline{B}\big) \end{pmatrix} \end{aligned} \tag{2.4}$$

The second term is the six-dimensional divergence of the phase-space particle flux $\dot{\overline{z}} \cdot f_a$. More explicity, we have the so-called Vlasov equation, derived as follows:

$$\frac{\partial f_a}{\partial t} + \frac{\partial}{\partial \overline{z}}\big(\dot{\overline{z}} f_a\big) = 0 \tag{2.5}$$

$$\frac{\partial f_a}{\partial t} + \begin{pmatrix} \overline{\nabla}_r & \overline{\nabla}_v \end{pmatrix} \begin{pmatrix} \overline{\mathrm{v}} f_a \\ \frac{e_a}{m_a}\big(\overline{E} + \overline{\mathrm{v}} \times \overline{B}\big) f_a \end{pmatrix} = 0 \tag{2.6}$$

$$\frac{\partial f_a}{\partial t} + \overline{\nabla}_r \cdot \big(\overline{v} f_a\big) + \overline{\nabla}_v \cdot \big(\frac{e_a}{m_a}(\overline{E} + \overline{\mathrm{v}} \times \overline{B}) f_a\big) = 0 \tag{2.7}$$

$$\frac{\partial f_a}{\partial t} + \overline{\mathrm{v}} \cdot \overline{\nabla}_r f_a + \frac{e_a}{m_a}\big(\overline{E} + \overline{\mathrm{v}} \times \overline{B}\big)\overline{\nabla}_v f_a = 0, \tag{2.8}$$

$$\text{where} \quad \overline{\nabla}_v \cdot \big(\overline{E} + \overline{\mathrm{v}} \times \overline{B}\big) = 0. \tag{2.9}$$

- Here $\overline{E}$ and $\overline{B}$ are the total electric and magnetic fields. Close to each charged particle

in the plasma these fields are too strong like the fields created by an individual particle in its neighborhood. In other words, $\overline{E}$ and $\overline{B}$ fluctuate strongly on short length scales comparable to Debye length, and the fluctuations are caused by discreteness of the charged distribution. However, from a macroscopic description of the plasma, we can ignore small-scale fluctuations, and instead regard $\overline{E}$ and $\overline{B}$ as large-scale fields. Therefore, we understand $\overline{E}$ and $\overline{B}$ being average of electric and magnetic fields over many Debye lengths. The effects of short-range electromagnetic fluctuations or collisions, on the distribution function are instead lumped into what we call the collision operator.

2.1.1 Collision operator

We now introduce the collision operator and its properties in the case of magnetized tokamak plasma [7, 19].

$$C_a(f_a) = \frac{\partial f_a}{\partial t}|_{collisions} \Big\} \begin{array}{l} \textit{effects of short-range} \\ \textit{electromagnetic fluctuations,} \\ \textit{or collisions, on the distribution function.} \end{array} \tag{2.10}$$

This object is relegated to the right-hand side of the kinetic equation:

$$\begin{aligned} \frac{\partial f_a}{\partial t} + \overline{\mathrm{v}} \cdot \overline{\nabla} f_a + \frac{e_a}{m_a}\big(\overline{E} + \overline{\mathrm{v}} \times \overline{B}\big)\frac{\partial f_a}{\partial \overline{\mathrm{v}}} &= C_a(f_a) \\ &= \frac{\partial f_a}{\partial t}|_{collisions} \end{aligned} \tag{2.11}$$

where $\overline{E}$ and $\overline{B}$ hence forth denote the average fields. For Coulomb collisions we shall see that C_a is a Fokker-Planck operator, the corresponding operator for a gas is the Boltzmann operator. The kinetic equation is often called the Fokker-Planck equation. If collisions are ignored it becomes to Vlasov equation.

The Collision operator is

$$C_a = \Sigma_a C_{ab}(f_a, f_b) \tag{2.12}$$

is a sum of contributions from collisions with each particle species $'b'$, including $b = a$, and

we expect it to satisfy certain conservation rules.

For instance, since collisions change only the velocity of the interacting particles, the density should not be affected by collisions.

$$\begin{aligned}\frac{\partial}{\partial t}\Big(\int f_a d^3v\Big)|_{coll} &= \int \Big(\frac{\partial}{\partial t} f_a|_{coll}\Big) d^3v \\ &= \int \big(C_a\big) d^3v \\ &= \int \Sigma_b C_{ab}\big(f_a, f_b\big) d^3v \\ &= \Sigma_b \int C_{ab}\big(f_a, f_b\big) d^3v\end{aligned} \tag{2.13}$$

$$\frac{\partial n_a}{\partial t}|_{collisions} = 0 \Rightarrow \int C_{ab}\big(f_a\big) d^3v = 0 \tag{2.14}$$

2.1.2 Conservation of momentum and energy

We move to the derivation of momentum and energy equations. Firstly we consider:

- Taking $\overline{\mathrm{v}}$ like the average velocity of species $'a'$ after collision with species $'b'$.

- Assuming that even when velocities of species $'a'$ and $'b'$ after collisions would be different, that difference is not huge and the collective velocity of species $'a'$ might be represented like $+\overline{\mathrm{v}}$, and $-\overline{\mathrm{v}}$ for species $'b'$ [6].

$$\begin{aligned}\vec{P}_{mom} &= m_a\overline{\mathrm{v}} n_a - m_b\overline{\mathrm{v}} n_b = const \\ \frac{\partial}{\partial t}\vec{P}_{mom} &= m_a\overline{\mathrm{v}}\frac{\partial}{\partial t} n_a - m_b\overline{\mathrm{v}}\frac{\partial}{\partial t} n_b = 0 \\ 0 &= m_a\overline{\mathrm{v}}\frac{\partial}{\partial t}\int f_a d^3v - m_b\overline{\mathrm{v}}\frac{\partial}{\partial t}\int f_b d^3v \\ 0 &= \Big(m_a\int \overline{\mathrm{v}}\frac{\partial}{\partial t} f_a d^3v\Big) - \Big(...\Big) \\ 0 &= m_a\int \overline{\mathrm{v}}\frac{\partial}{\partial t} f_a d^3v - m_b\int \overline{\mathrm{v}}\frac{\partial}{\partial t} f_b d^3v\end{aligned} \tag{2.15}$$

The collisions between $'a'$ and $'b'$ show us that an increase of f_a is followed by a decrease of f_b and vice versa. Then $-\partial f_b/\partial t > 0$ and

$$\begin{aligned}
0 &= m_a \int \overline{\mathrm{v}} \frac{\partial}{\partial t} f_a d^3v + m_b \int \overline{\mathrm{v}} \frac{\partial}{\partial t} f_b d^3v \\
0 &= \int m_a \overline{\mathrm{v}} C_a\big(f_a\big) d^3v + \int m_b \overline{\mathrm{v}} C_b\big(f_b\big) d^3v \\
0 &= \int m_a \overline{\mathrm{v}} \Sigma_b C_{ab}\big(f_a, f_b\big) d^3v + \int m_b \overline{\mathrm{v}} \Sigma_a C_{ab}\big(f_a, f_b\big) d^3v \\
0 &= \big(... + \int m_a \overline{\mathrm{v}} C_{ab} d^3v + \big) + \big(... + \int m_b \overline{\mathrm{v}} C_{ba} d^3v + \big)
\end{aligned} \tag{2.16}$$

C_{ab} and C_{ba} are related due to b-a coll.

- Terms $m_a \overline{\mathrm{v}} C_{ab}$ and $m_b \overline{\mathrm{v}} C_{ba}$ represent a generalization of momemtum collisions because the term $m_b \overline{\mathrm{v}}$ indicates the momentum term for $'b'$ and the term C_{ba} is releated with the probalility of collision between $'b'$ and $'a'$ [7]. Then the momentum conservation between particles $'a'$ and $'b'$ linked with collision terms give us:

$$\begin{aligned}
\int m_a \overline{\mathrm{v}} C_{ab} d^3v + \int m_b \overline{\mathrm{v}} C_{ba} d^3v = 0 \\
\int m_a \overline{\mathrm{v}} C_{ab}\big(f_a\big) = - \int m_b \overline{\mathrm{v}} C_{ba}\big(f_b\big)
\end{aligned} \tag{2.17}$$

Analogously for Energy:

$$\int \frac{m_a v^2}{2} C_{ab}\big(f_a\big) d^3v = - \int \frac{m_b v^2}{2} C_{ba}\big(f_b\big) d^3v \tag{2.18}$$

Due to force that species $'a'$ exerts on species $'b'$ is equal in magnitude and with opposite orientation to exerts from $'b'$ to $'a'$, and that no net energy is produced by collisions. Taking $a = b$

$$\begin{aligned}
\int m_a \overline{\mathrm{v}} C_{aa}\big(f_a\big) d^3v = 0 \\
\int \frac{m_a v^2}{2} C_{aa}\big(f_a\big) d^3v = 0
\end{aligned} \tag{2.19}$$

Another important property of the collision operator is that it drives the distribution function toward local thermodynamic equilibrium, s shifted Maxwellian distribution.

$$
\begin{aligned}
&f_{M_a}(\overline{r},t) = n_a(\overline{r},t)\Big(\frac{m_a}{2\pi T_a(\overline{r},t)}\Big)^{3/2}\exp\frac{m_a\big[\overline{\mathrm{v}}-\overline{\mathrm{V}}_a(\overline{r},t)\big]}{2T_a(\overline{r},t)}\\
&n_a : \text{density}\\
&\overline{\mathrm{V}}_a : \text{average velocity}\\
&T_a : \text{temperature}
\end{aligned}
\tag{2.20}
$$

The collision operator vanishes if, and only if, all species have the same mean velocity and temperature. In one species, $C_{aa}(f_{M_a})$ for arbitrary average velocity $\overline{\mathrm{V}}_a$, manifesting Galilean invariance of the collision operator [7, 8].

$$
\begin{aligned}
&C_{aa}(f_{M_a}) = 0 \quad \} \quad C_{a'a'}(f_{M_{a'}}) = 0\\
&a \text{ and } a' \text{ are particles of the same system,}\\
&\text{then we have a } \overline{R}\in\mathbb{R}^3,\\
&\text{where: } \overline{r_{a'}} = \overline{R}_0 + \overline{r}_a.\\
&\Rightarrow C_{aa'}(f_{M_{a'}}) = 0 \longleftrightarrow C_{aa}(f_{M_a(\overline{R}_0+\overline{r}_a)}) = 0, \forall\overline{R}_0\in\mathbb{R}^3
\end{aligned}
\tag{2.21}
$$

2.1.3 Fluid Equations

Most useful information from the distribution function f_a is conteined in its first moments, i.e., integrals over velocity space of f_a multiplied by different functions of $\overline{v}$. The 'zeroth' moment is the density [9]:

$$
n_a(\overline{r},t) = \int f_a(\overline{r},\overline{v},t)d^3v \tag{2.22}
$$

and moments of higuer order are defined as follow:

$$
\langle A\rangle_{f_a} = \frac{1}{n_a}\int A f_a d^3v. \tag{2.23}
$$

The macroscopic fluid velocity is now defined by

$$
\overline{V}_a(\overline{r},t) = \langle\overline{v}\rangle_{f_a} \tag{2.24}
$$

and it is equal to the average of any particle of species 'a' in a random point in space. The velocity of a random particle differs from its average velocity by $\overline{v}' = \overline{v} - \overline{V}_a$. The temperature is T_a and $3T_a/2$ represents the average of kinetic energy associated with random velocities [7]:

$$\begin{aligned}
\frac{3}{2}T_a(\overline{r},t) &= \langle \frac{m_a \overline{v'}_a}{2} \rangle_{f_a} \\
&= \langle \frac{m_a}{2}\big(\overline{v} - \overline{V}_a\big)\big(\overline{v} - \overline{V}_a\big) \rangle_{f_a} \\
&= \frac{m_a}{2}\langle v^2 \rangle - m_a \langle \overline{v} \cdot \overline{V}_a \rangle + \frac{m_a}{2} V_a^2 \\
&= \frac{m_a}{2}\langle v^2 \rangle - m_a \overline{V}_a \langle \overline{v} \rangle + \frac{m_a}{2}\langle V_a^2 \rangle \\
&= \frac{m_a}{2}\langle v^2 \rangle - \frac{m_a}{2} V_a^2 .
\end{aligned} \tag{2.25}$$

Taking the moment of $m_a v^2/2$,

$$\begin{aligned}
\langle \frac{m_a v^2}{2} \rangle &= \frac{1}{n_a}\int \frac{m_a v^2}{2} f_a d^3 v \\
\int \frac{m_a}{2} v^2 f_a d^3 v &= \frac{m_a n_a \langle v^2 \rangle}{2} \\
&= \frac{3}{2} n_a T_a + \frac{m_a n_a}{2} V_a^2
\end{aligned} \tag{2.26}$$

we have found that total energy is the addition of kinetic energy associated with the average velocity and the thermal energy.

Fluid equations are formed by taking analogous moments to the kinetic equations;

$$\begin{aligned}
\frac{\partial n}{\partial t} + \overline{\nabla} \cdot (n\overline{v}) &= 0 \\
\frac{\partial mn\overline{v}}{\partial t} + \overline{\nabla} \cdot \Pi &= n_e(\overline{E} + \overline{v} \times \overline{B}) + \int m\overline{v} C(f) d^3 v, \\
\frac{\partial}{\partial t}\big(\frac{3nT}{2} + \frac{mnV^2}{2}\big) + \nabla \cdot Q &= en\overline{E} \cdot \overline{V} + \int \frac{mv^2}{2} c(f) d^3 v
\end{aligned}$$

where we dropped the species index and introduced the following notation for the flux of momentum and energy

$$\Pi_{ij} = \langle mnv_i v_j \rangle_{f_a}, \quad Q = \frac{mn}{2}\langle v^2 \overline{\mathrm{v}} \rangle_{f_a}.$$

Working with the equation for the distribution f_s:

$$\frac{\partial f_s}{\partial t} + \overline{\nabla} \cdot (\overline{\mathrm{v}} f_s) + \overline{\nabla_v} \cdot \big[\frac{z_s e}{m_s}(\overline{E} + \overline{\mathrm{v}} \times \overline{B}) f_s\big] = \Sigma_{s'} C_{ss'}\big[f_s, f_{s'}\big],$$

$$\Big(\frac{\partial f_s}{\partial t} + \overline{\nabla} \cdot (\overline{\mathrm{v}} f_s) + \overline{\nabla_v} \cdot \big[\frac{z_s e}{m_s}(\overline{E} + \overline{\mathrm{v}} \times \overline{B}) f_s\big] = \Sigma_{s'} C_{ss'}\big[f_s, f_{s'}\big]\Big) \times X(\overline{\mathrm{v}})$$

with $X(\mathrm{v})$ as function of v

$$\int X(\overline{\mathrm{v}}) \frac{\partial f_s}{\partial t} d^3v + \int X(\overline{\mathrm{v}}) \overline{\nabla} \cdot (\overline{v} f_s) d^3v + \int X(\overline{\mathrm{v}}) \cdot \overline{\nabla}_v \Big[\frac{z_s e}{m_s}\big(\overline{E} + \overline{\mathrm{v}} \times \overline{B}\big) f_s\Big] d^3v =$$

$$\Sigma_{s'} \int X(\overline{\mathrm{v}}) C_{ss'}[f_{s'}, f_{s'}] d^3$$

$$\frac{\partial}{\partial t} \int X(\overline{\mathrm{v}}) f_s d^3v + \overline{\nabla} \cdot \big(\int X(\overline{\mathrm{v}}) f_s \overline{\mathrm{v}} d^3v\big) + X(\overline{\mathrm{v}}) \frac{z_s e}{m_s}\big(\overline{E} + \overline{\mathrm{v}} \times \overline{B}\big) f_s|_{-\infty}^{+\infty} =$$

$$+ \int \frac{z_s e}{m_s}\big(\overline{E} + \overline{\mathrm{v}} \times \overline{B}\big) f_s \overline{\nabla}_v X(\overline{\mathrm{v}}) d^3v + \Sigma_{s'} \int X C_{ss'}[f_s, f_{s'}] d^3v$$

$$\frac{\partial}{\partial t} \int X(\overline{\mathrm{v}}) f_s d^3v + \overline{\nabla} \cdot \big(\int X(\overline{\mathrm{v}}) f_s \overline{\mathrm{v}} d^3v\big) =$$

$$\int \frac{z_s e}{m_s}\big(\overline{E} + \overline{\mathrm{v}} \times \overline{B}\big) f_s \overline{\nabla}_v X(\overline{\mathrm{v}}) d^3v + \Sigma_{s'} \int X C_{ss'}[f_s, f_{s'}] d^3v \tag{2.27}$$

For $X = 1$:

$$\frac{\partial}{\partial t} n_s + \overline{\nabla} \cdot (n_s \overline{u}_s) = 0 \quad \text{with} \quad \overline{u}_s = \frac{1}{n_s} \int f_s \overline{\mathrm{v}} d^3v \tag{2.28}$$

Since collisions change just the velocity of the interacting particles, and not their spatial location, the density should not be affected by collisions.

$$\frac{\partial n_s}{\partial t}|_{coll} = 0 \Rightarrow \Sigma_b \int C_{ab}(f_a) d^3v = 0. \tag{2.29}$$

For $X = m_s\overline{\mathrm{v}}$ (momentum conservation),

$$\begin{aligned}
&\frac{\partial}{\partial t}\int m_s\overline{\mathrm{v}}f_s d^3v + \overline{\nabla}\cdot\Big(\int m_s\overline{\mathrm{v}}f_s\overline{\mathrm{v}}d^3v\Big)\\
=&\frac{z_s e}{m_s}\int(\overline{E}+\overline{\mathrm{v}}\times\overline{B})\cdot\overline{\nabla}_v(Xn_s\overline{\mathrm{v}})f_s d^3v + \Sigma_{s'}\int m_s\overline{\mathrm{v}}C_{ss'}[f_s,f_{s'}]d^3v,\\
&\frac{\partial}{\partial t}(m_s n_s\overline{u}_s) + \overline{\nabla}\cdot\Big(\int m_s f_s\overline{\mathrm{v}}\otimes\overline{\mathrm{v}}d^3v\Big)\\
=&z_s e n_s(\overline{E}+\overline{u}_s)\times\overline{B} + \Sigma_{s'}\int m\overline{v}C_{ss'}[f_s,f_{s'}]d^3\\
&\text{with}\quad F_{ss'} = \int m_s\overline{\mathrm{v}}C_{ss'}[f_s,f_{s'}]d^3v,
\end{aligned}$$

analysing the next term:

$$\begin{aligned}
\int f_s m_s\overline{\mathrm{v}}\overline{\mathrm{v}}d^3v &= n_s m_s\overline{u}_s\overline{u}_s + \int f_s m_s\overline{\mathrm{w}}\overline{\mathrm{w}}d^3w\\
&= n_s m_s\overline{u}_s\overline{u}_s + \int f_s m_s\frac{\omega^2}{3}\overline{I}d^3\omega + \int f_s m_s(\overline{\mathrm{w}}\overline{\mathrm{w}} - \frac{\omega^3}{3}\overline{I})d^3\omega\\
&= n_s m_s\overline{u}_s\overline{u}_s + (T_s n_s)\overline{I} + \int f_s m_s(\overline{\mathrm{w}}\overline{\mathrm{w}} - \frac{\omega^3}{3}\overline{I})d^3\omega\\
&= n_s m_s\overline{u}_s\overline{u}_s + p_s\overline{I} + \Pi_s
\end{aligned}$$

$$\begin{aligned}
&\frac{\partial}{\partial t}(n_s m_s u_s) + \overline{\nabla}\cdot(n_s m_s\overline{u}_s\overline{u}_s) + \overline{\nabla}p_s\overline{\nabla}\cdot\Pi_s\\
&\qquad = z_e e n_s(\overline{E}+\overline{u}_s\times\overline{B}) + \Sigma_{s'\neq s}F_{ss'},
\end{aligned}\tag{2.30}$$

reducing the terms:

$$\begin{aligned}
\frac{\partial}{\partial t}(n_s m_s\overline{u}_s) + \overline{\nabla}\cdot(n_s m_s\overline{u}_s\overline{u}_s) &= m_s\frac{\partial n_s}{\partial t}\overline{u}_s + + m_s n_s\frac{\partial\overline{u}_s}{\partial t} + m_s\nabla(n_s u_s)u_s + m_s n_s\overline{u}_s\overline{\nabla}\overline{u}_s\\
&= m_s n_s\frac{\partial\overline{u}_s}{\partial t} + m_s n_s\overline{u}_s\overline{\nabla}\overline{u}_s = m_s n s\big(\frac{\partial\overline{u}_s}{\partial t} + \overline{u}_s\overline{\nabla}\overline{u}_s\big)
\end{aligned}$$

Therefore the final form of the momentum dynamic equation is:

$$n_s m_s\big(\frac{\partial\overline{u}_s}{\partial t} + \overline{u}_s\cdot\overline{\nabla}\overline{u}_s\big) + \overline{\nabla}p_s + \overline{\nabla}\cdot\Pi_s = z_e e n_s(\overline{E}+\overline{u}_s\times\overline{B}) + \Sigma_{s\neq s'}F_{ss'} \quad\text{where}\quad (\nabla\cdot\Pi)_j = \partial\Pi_{jk}/\partial x_k \tag{2.31}$$

For $X = m_s v^2/2$ (energy conservation),

$$\frac{\partial}{\partial t}\Big(\int\frac{1}{2}m_s v^2 f_s d^3v\Big) + \nabla\cdot\Big(\int\frac{1}{2}m_s v^2 f_s\overline{v}d^3v\Big) = z_s e n_s\overline{E}\cdot\overline{u}_s + \Sigma_{s'\neq s}W_{ss'}, \tag{2.32}$$

where $W_{ss'} = \int (1/2) m_s v^2 C_{ss'}[f_s, f_{s'}] d^3v$ is the energy gained by species 's' due to collisions with species 's".

Reducing terms:

$$\int \frac{1}{2} m_s v^2 f_s d^3v = \frac{3}{2} n_s T_s + \frac{1}{2} n_s m_s u_s^2, \tag{2.33}$$

$$\begin{aligned}
\int \frac{1}{2} m_s v^2 f_s \overline{\mathrm{v}} d^3v &= \int \frac{1}{2} m_s (\omega^2 + u_s^2 + 2\overline{w} \cdot \overline{u}_s) f_s (\overline{w} + \overline{u}_s) d^3v \\
&= \int \frac{1}{2} m_s \omega^2 f_s (\overline{w} + \overline{u}_s) d^3v + \int \frac{1}{2} m_s u_s^2 f_s (\overline{w} + \overline{u}_s) d^3v + \int m_s \overline{w u}_s f_s \overline{w} d^3v \\
&+ \int m_s \overline{w u}_s f_s \overline{u}_s d^3v \\
&= \int \frac{1}{2} m_s \omega^2 f_s (\overline{w} + \overline{u}_s) d^3v + \int \frac{1}{2} m_s u_s^2 f_s (\overline{w} + \overline{u}_s) d^3v + \int m_s \overline{w u}_s f_s \overline{w} d^3v \\
&+ \int m_s \overline{w u}_s \overline{\overline{I}} f_s \overline{u}_s d^3v \\
&= \int \frac{1}{2} m_s \omega^2 f_s (\overline{w} + \overline{u}_s) d^3v + \int \frac{1}{2} m_s u_s^2 f_s (\overline{w} + \overline{u}_s) d^3v + \int m_s \overline{w u}_s f_s \overline{w} d^3v \\
&+ u_s^2 \int m_s \overline{w} \overline{\overline{I}} f_s d^3v \\
&= \int \frac{1}{2} m_s \omega^2 f_s \overline{w} d^3v + \int \frac{1}{2} m_s \omega^2 f_s \overline{u}_s d^3v + \frac{1}{2} m_s u_s^2 n_s \overline{u}_s \\
&+ \int m_s \overline{w u}_s f_s \overline{w} d^3v \\
&= \overline{q}_s + \frac{3}{2} n_s T_s \overline{u}_s + \frac{1}{2} m_s n_s u_s^2 \overline{u}_s + \big(\int m_s \overline{w} \cdot \overline{w} f_s d^3v \big) \overline{u}_s \\
&= \overline{q}_s + \frac{3}{2} n_s T_s \overline{u}_s + \frac{1}{2} m_s n_s u_s^2 \overline{u}_s \\
&+ \Big(\big(\int m_s \overline{w w} f_s d^3v \big) \overline{u}_s - \big(\int m_s \frac{\omega^3}{3} f_s d^3v \big) \overline{u}_s \Big) + \int m_s \frac{\omega^2}{3} f_s d^3v \cdot \overline{u}_s
\end{aligned}$$

$$\int \frac{1}{2} m_s v^2 f_s \overline{\mathrm{v}} d^3v = \overline{q}_s + \frac{3}{2} n_s T_s \overline{u}_s + \frac{1}{2} m_s n_s u_s^2 \overline{u}_s + \Pi_s \cdot \overline{u}_s + n_s T_s \overline{u}_s. \tag{2.34}$$

Replacing equations 2.33 and 2.34 in equation 2.32:

$$\frac{\partial}{\partial t} \big(\frac{3}{2} n_s T_s + \frac{1}{2} n_s m_s u_s^2 \big) + \overline{\nabla} \cdot \big[\overline{q}_s + \big(\frac{5}{2} n_s T_s + \frac{1}{2} n_s m_s u_s^2 \big) \overline{u}_s + \Pi_s \cdot \overline{u}_s \big] = z_s e n_s \overline{E} \cdot \overline{u}_s + \Sigma_{s' \neq s} W_{ss'}$$

$$n_s \big(\frac{\partial}{\partial t} + \overline{u}_s \cdot \overline{\nabla} \big) \big(\frac{3}{2} T_s + \frac{1}{2} m_s u_s^2 \big) + \nabla \cdot (q_s + n_s T_s \overline{u}_s + \Pi_s \overline{u}_s) = z_s e n_s \overline{E} \cdot \overline{u}_s + \Sigma_{s' \neq s} W_{ss'} \tag{2.35}$$

Substracting equation 2.31 to 2.35 [6]:

$$\frac{3}{2}n_s\big(\frac{\partial}{\partial t}T_s + \overline{u}_s \cdot \nabla T_s\big) + \Pi_s : \overline{\nabla}\overline{u}_s + \overline{\nabla} \cdot \overline{q}_s + n_s T_s \overline{\nabla} \cdot \overline{u}_s = \Sigma_{s' \neq s}\overline{W}_{ss'}$$
$$\text{with} \quad \overline{W}_{ss'} = W_{ss'} - F_{ss'}\overline{u}_s = \int \frac{1}{2} m\omega^2 C_{ss'}[f_s, f_{s'}]d^3\omega \tag{2.36}$$

2.2 From Braginskii equations to the two-point model

The two point model gives a simple description of the steady-state SOL, through a zero dimensional approach. It correlates plasma and temperature of plasma between two points: one positioned at the solid target or the sheath edge, and the other far upstream, e.g., at the outer midplane in the case of a tokamak. The main variables used in the model are the plasma density and temperature both at the upstream position (n_u, T_u) and at the target (n_t, T_t), as well as the heat flux $q_{||}$. The last quantity is the power density that flows in the SOL along the direction parallel to the magnetic field. This power flux is supposed to be conserved through the length of the scrape-of layer.

The model consists of three equations, that consequently allows to evaluate three of the parameter of the problem listed before, knowing the remaining two variables. For example it is possible to calculate the plasma density and temperature at the target, as well the temperature upstream, starting from the parallel heat flux and density upstream. This last two quantities depend respectively on the heating power and the particle source (e.g. gas puffing) that are both set parameters in a tokamak (direct two point model). In a similar fashion one can obtain the parallel heat flux and the target parameters using the density and temperature at the upstream position (inverse two point model). The first equation is given below (Eq. 2.37) which describes the energy sink action provided by the Debye sheath. It is also referred as Bohm boundary condition for the heat flux.

$$q_{se} = q^i_{se} + q^e_{se} = \gamma k T_e \Gamma_{se} \tag{2.37}$$

The derivation of the other two equations is presented in the following subsections.

2.2.1 Conservative form of the momentum equation

Let us begin writing the steady state Navier-Stokes equation of momentum conservation for a plasma specie s, provided with a charge q_s, which is inserted in a magnetic field B and electric field E:

$$\nabla \cdot \Pi_s = n_s q_s \big(\vec{E} + \vec{v}_s \times \vec{B}\big) + \vec{S} \tag{2.38}$$

Where Π_s is the total pressure tensor; S is the source of momentum. For each species the total pressure tensor is defined as:

$$\Pi_s = p_s I + n_s m_s \vec{v}_s \otimes \vec{v}_s + \pi_s \tag{2.39}$$

Where p_s is the isotropic pressure; π_s the stress tensor. The term with the tensor product between the velocity of the specie s and itself, is the one that takes into account the dynamic share of the pressure. Another assumption of the two point model is that in the SOL there is neither source of momentum (other than the Coulomb and Lorentz forces) nor momentum sink (only the sheath acts as momentum well). Therefore we can neglect both the term S_s and the stress tensor pi_s. Projecting the equation in the direction parallel to the magnetic field, we find:

$$\frac{d\big(p_s + n_s m_s v_{s||}^2\big)}{dx} = n_s q_s E_{||} \tag{2.40}$$

Where x is the spatial dimension along the field direction. For an hydrogenic plasma, this equation would assume the following expressions for ions and electrons:

$$\frac{d\big(p_i + n_i m_i v_{i||}^2\big)}{dx} = n_i e E_{||} \tag{2.41}$$

$$\frac{d\big(p_e + n_e m_e v_{e||}^2\big)}{dx} = n_e e E_{||} \tag{2.42}$$

By summing together the last two relations, we get:

$$\frac{p_i + p_e + n_i m_i v_{i||}^2 + n_e m_e v_{e||}^2}{dx} = n_i e E_{||} - n_e e E_{||} \tag{2.43}$$

We can now make two simple assumptions. The first consists in evaluating the inertia of the electrons to be negligible if compared to the one of the ions ($mi >> me$; $mi/me = 1836$, for hydrogen), while the other states the quasi-neutrality of plasma ($n_i = n_e = n$). However we need to add another hypothesis, the ambipolarity of the flow ($v_{i||} = v_{e||}$). While the first two propositions seem quite reasonable (since the dimension of the system is much larger than the Debye length), the last one is less intuitive. To understand why it is plausible to assert such statement, we write the parallel-to-B current density in the SOL:

$$J_{||} = e\big(n_i v_{i||} - n_e v_{e||}\big) \tag{2.44}$$

This parameter is usually very small in the plasma edge (instead of inside the core), since both species are drawn to the target plates regardless of the charge. There is no preferable direction for ions or electrons in the SOL; the pressure gradient affects the two species equally. Thus, if we consider $J_{||} \sim 0$ and the quasi-neutrality, we derive the ambipolarity condition.

After the considered assumptions, the equation 2.43 becomes:

$$\frac{d\big(p_i + p_e + n m_i v_{i||}^2\big)}{dx} = 0 \tag{2.45}$$

or

$$p_i + p_e + n m_i v_{i||}^2 = const. \tag{2.46}$$

Such law is referred as the conservative form of the momentum equation. The last step would be to remember the definitions of pressure for a Maxwellian specie, and of the Mach number:

$$\begin{aligned} p_i + p_e + n m_i v_{i||}^2 &= n\big(kT_i + kT_e\big) + n m_i M^2 c_s^2 \\ &= n\big(kT_i + kT_e\big)\big(1 + M^2\big) \\ &= const. \end{aligned} \tag{2.47}$$

Where the sound speed $c_s = \sqrt{\frac{kT_i + kTe}{m_i}}$. Finally we can write this conservation law for the

upstream position ($M \sim 0$) and the target ($M = 1$, Bohm criterion), deriving the second equation of the two point model:

$$\boxed{n_u k T_u = 2 n_t k T_t} \tag{2.48}$$

2.2.2 Heat transfer inside the SOL

In the assumptions of the two point model, the power flowing from the core P_{SOL} enters the SOL in a localized fashion at the upstream position. However it can be demonstrated that the temperature gradient is not heavily influenced from the distribution of the heat source in the edge plasma [1]. The power is exhausted at the target through the Debye sheath. No other energy sinks or sources exist in the edge plasma (no radiation losses, no heating). For this reason the sheath condition, described in equation 2.37, allows us, once integrated on the surface perpendicular to the magnetic field, to determine the power that flows in each section of the SOL. However we still need to characterize how the heat is transferred along the SOL, which will provide an evaluation of the temperature gradient along the edge. The main heat propagation mechanisms are conduction and convection. The latter is dominant over the previous one when the outflow of particle inside the SOL is more or less uniform along its length. This is the case when the main source of plasma particle (from the ionization of neutrals) is located inside the core plasma. This leads to significant plasma flow along all the length of the SOL, which results in a convective heat flow. In this condition, a negligible drop of temperature exists between the upstream and target positions. In fact, the presence of a relevant temperature difference is intrinsically correlated with conduction, since this heat transfer mechanism depends directly on the temperature gradient. When ionization mean free paths are short in respect to the plasma dimension, ionization occurs mainly in the SOL, and it will also generally occur mainly close to the source of the recycling neutrals: the targets. The flow of plasma in the SOL is significantly decreased, in respect of the case where convection is relevant. The power source is located at the top end, but all the particle source is in front of the solid wall, resulting in the heat being mainly conducted out

of the plasma. Strong temperature drops are desirable along the SOL, since they allow to maintain high temperatures in the plasma core, while having a cold particle flux at the wall. Low temperatures at the target position result in decreased erosion of the solid boundary and therefore an increased lifetime of the plasma vessel. The presence of a temperature difference between the upstream and target positions is essential to operate a plasma device in an high performance regime, without compromising the plasma facing components.

The convective plasma flow can be evaluated from a drifting Maxwellian. We can write the parallel convective heat flux for electrons $q^e_{||,conv}$ and ions $q^i_{||,conv}$:

$$q^e_{||,conv} = \frac{5}{2} k T_e n_e v_{e||} \tag{2.49}$$

$$q^i_{||,conv} = \Big(\frac{5}{2} k T_i + \frac{1}{2} m_i v^2_{i||}\Big) n_i v_{i||} \tag{2.50}$$

Defining the total convective heat flux $q_{||,conv}$ as the sum of the contributes of both species, we derive:

$$\begin{aligned} q_{||,conv} &= q^i_{||,conv} + q^e_{||,conv} \\ q_{||,conv} &= \Big(5kT + \frac{1}{2} m_i v^2_{i||}\Big) n v_{i||} \end{aligned} \tag{2.51}$$

To obtain this relation we add to the same assumptions introduced for the derivation of the momentum conservation equation (ambipolarity, negligible inertia of electrons, quasi-neutrality), the hypothesis of equipartition between plasma species ($T_e = T_i = T$). For describing conduction, the classical Spitzer relation can be used for both ions and electrons:

$$q^e_{||,cond} = -\kappa_{0e} T_e^{5/2} \frac{dT_e}{dx} \tag{2.52}$$

$$q^i_{||,cond} = -\kappa_{0i} T_i^{5/2} \frac{dT_i}{dx} \tag{2.53}$$

Where the thermal conductivity is $K_{||} = \kappa_0 T^{5/2}$. For a pure hydrogenic plasma, the coefficients κ_0 for electrons and ions are $\kappa_{0e} \sim 2000$ and $\kappa_{0i} \sim 60$, for the heat flux expressed in $[Wm^{-2}]$, temperature in $[eV]$ and the temperature gradient in $[eVm^{-1}]$.

If electrons and ions are thermally well coupled we have that $q^e_{||,cond} \gg q^i_{||,cond}$, since the con-

ductivity of electrons is of two order of magnitude greater. Therefore, electron conduction is generally used to approximate the transport of the total conducted power.

$$\begin{aligned} q_{||,cond} &= q^e_{||,cond} + q^i_{||,cond} \\ &\sim q^e_{||,cond} \end{aligned} \tag{2.54}$$

The final assumption of the two point model consists in considering the convection in the SOL negligible in respect to the conduction.

$$\begin{aligned} q_{||} &= q_{||,cond} + q_{||,conv} \\ &\sim q^e_{||,cond} \\ &= -\kappa_{0e} T_e^{5/2} \frac{dT_e}{dx} \end{aligned} \tag{2.55}$$

As explained before, this hypothesis gives us information also about the distribution of the particle source in the SOL. If the main heat transfer occurs through conduction, the plasma flow is almost zero over the entire length of the layer, with the exception of the region near the target where recycling takes place. Essentially, the plasma is accelerated mainly in the region in front of the wall of depth comparable with the ionization mean free path of neutrals. We can now integrate equation 2.55 between the upstream and target positions:

$$\begin{aligned} \int_u^t q_{||} dx &= -\int_u^t \kappa_{0e} T^{5/2} dT \\ q_{||} L_{||} &= \frac{2}{7} \kappa_{0e} \Big(T_u^{7/2} - T_t^{7/2} \Big) \end{aligned} \tag{2.56}$$

We finally derive the last equation of the two point model, that gives us information on the temperature gradient in the SOL:

$$\boxed{T_u^{7/2} = T_t^{7/2} + \frac{7}{2} \frac{q_{||} T_{||}}{\kappa_{0e}}} \tag{2.57}$$

In these relations the quantity $L_{||}$ is called connection length. For the plasma edge, this parameter can be interpreted as the extension of the SOL between the upstream position and the target.

2.2.3 Density regimes

We finally completed the description of the two point model. The equations of conservation of momentum, power balance and continuity have led us to write the following relations:

$$\boxed{\begin{cases} q_{||} = \gamma k T_t n_t c_{s,t} \\ n_u k T_u = 2 n_t k T_t \\ T_u^{7/2} = T_t^{7/2} + \dfrac{7}{2} \dfrac{q_{||} L_{||}}{\kappa_{0e}} \end{cases}} \tag{2.58}$$

In order to simplify the analysis, from now on the temperature will be expressed in $[eV]$ rather than in $[K]$, omitting the Boltzmann constant k. The equivalence formula between the two form is the following:

$$T[eV] = \frac{k}{e} T[K] \tag{2.59}$$

What can we deduce from this simple description of the SOL? Let us begin by analyzing how the several parameters of interest treated in the model ($q_{||}, T_u, n_u, T_t, n_t$) are correlated one to another. To simplify the study we suppose one of the five free parameters to be fixed: the parallel heat flux. In fusion plasmas this quantity is directly correlated with both the dimension of the machine and the heating power, which is mainly provided by the nuclear reactions and by the auxiliary heating system (e.g. ECRH, ICRH, NBI). It is clear that this is a parameter that should be maximized as much as possible. In fact an higher achievable energy flux would result in smaller investment cost, since a smaller machine can be used for a given fusion power, or analogously in better performance; with fixed dimension of the device it is possible to increase the power produced. However an upper limit of the parallel heat flux is ultimately given by the thermo-mechanical resistance of the materials. Considering this quantity as fixed is therefore not a strong approximation of the real case. The current technological threshold for a tungsten target, like the one used for the International Thermonuclear Experimental Reactor (ITER), is in the order of magnitude of $10 MW m^{-2}$. If an expansion of the magnetic flux between the upstream and the target positions of ~ 5 is taken into account, as well as an inclination of the solid target in respect

to the field lines of 3°, our technological limit at the wall translates into a maximum parallel heat flux in the upstream position as:

$$10MWm^{-2}\frac{5}{sin(3^\circ)} \sim 1GWm^{-2}$$

This is the fixed value that will be considered in the present analysis.

We can now proceed expressing three of the remaining parameters as a function of the fourth, which is taken as an independent variable. A proper choice for this latter quantity is the plasma density at the upstream position, indicated with n_u, since it is correlated with the source of particle that can be practically increased through gas puffing or pellet injecting inside the machine. Under this light n_u can be seen as an engineering parameter, which can be set a priori. Starting from the relation of the two point model 2.58, we can then deduce the following equations for T_t, n_t and T_u:

$$T_t^{7/2} - \Big(\frac{2q_{||}}{\gamma n_u e}\sqrt{\frac{m_i}{2e}}\Big)^{7/2} T_t^{-7/4} + \frac{7}{2}\frac{q_{||}L_{||}}{\kappa_{0e}} = 0 \tag{2.60}$$

$$\Big(\frac{q_{||}}{\gamma e}\sqrt{\frac{m_i}{2e}}\Big)^{7/3} n_t^{-7/3} - \Big(\frac{2}{n_u}\Big)^{7/2}\Big(\frac{q_{||}}{\gamma e}\sqrt{\frac{m_i}{2e}}\Big)^{7/3} n_t^{7/6} + \frac{7}{2}\frac{q_{||}L_{||}}{\kappa_{0e}} = 0 \tag{2.61}$$

$$- T_u^{7/2} + \Big(\frac{q_{||}}{\gamma n_u e}\sqrt{\frac{m_i}{2e}}\Big)^{7} T_u^{-7} + \frac{7}{2}\frac{q_{||}L_{||}}{\kappa_{0e}} = 0 \tag{2.62}$$

The sound speed is evaluated in the case of isothermal plasma, which can be written as the following:

$$\begin{aligned} c_{s,t} &= \sqrt{\frac{eT_{i,t} + eT_{e,t}}{m_i}} \\ &= \sqrt{\frac{2eT_t}{m_i}} \end{aligned} \tag{2.63}$$

We see in the result a distinct change of trend when the density far from the wall reaches a certain value. The plasma density at the target increases monotonically with the upstream density, and in both regimes the double logarithm plot can be linearized. A similar evaluation can be made for the temperature drop in the SOL. Now we see a strictly

decreasing trend of temperature with n_u, which does not go against the physical intuition. A more dense plasma, at equal heat flux, would result in a lower temperature (energy dilution). In the regime of low upstream density, we observe that the temperature in the SOL stays in first approximation constant, since T_u and T_t are almost equal. As we pass the density threshold, the temperature upstream tends asymptotically to a constant value, whereas the temperature at the target decreases more rapidly than in the previous regime. As in the case of the target density, the temperature trend can be linearized in a logarithm plot in both density domains. These conclusions suggest us to better analyze this different regimes, and hopefully reach a simpler formulation of the two point model which would allow us to obtain a close form derivation of our parameters rather than solving numerically the equations (2.60, 2.61, 2.62).

2.2.4 The sheath-limited regime

At low plasma density in the upstream region, we observe that the temperature along the SOL field line is almost constant. We can therefore assume $T_u \sim= T_t$ and see how the equations (2.58) of the two point model change under this assumption:

$$\begin{cases} T_t = \left(\frac{2}{\gamma e}\sqrt{\frac{m_i}{2e}}^{2/3} \frac{q_{||}^{2/3}}{n_u^{2/3}}\right) \\ n_t = \frac{n_u}{2} \\ T_u = T_t \end{cases} \tag{2.64}$$

Since no temperature gradient exists, the third equation that describes the conducted power along the SOL looses sense. In fact, in this case the heat is transferred through convection. The momentum conservation equation gives us a linear proportionality between the densities at the ends of the SOL ($n_t \propto n_u$). One can thus understand why this regime is also called linear. For the temperatures, we observe instead a dependence from n_u that goes with the power of $-\frac{2}{3}$, i.e. $T_t \propto n_u^{-2/3}$).

In the approximation made, the SOL does not change the plasma temperature, because

convection is dominating the heat transfer. What governs the heat flow is only the Debye sheath, hence the name sheath-limited regime for this domain of operation. Sheath limited regime occurs when the source of particle is mainly located outside the SOL, in the core. For this condition the flow of particles in the plasma edge is not negligible, and it does not allow for a temperature gradient to build up.

2.2.5 The high-recycling regime

The second regime can be described by a different, but specular, condition on the temperature. The approximation made in this domain is that the plasma temperature at the target is negligible in respect to upstream ($T_u \gg T_t$). Of course the eventuality of having a hotter plasma at the wall would go against the second law of thermodynamics, since no source of energy is present in the SOL. The equations 2.58 will become:

$$\begin{cases} T_t = \left(\frac{2q_{||}}{\gamma n_u e T_u}\sqrt{\frac{m_i}{2e}}\right)^2 = \left(\frac{m_i}{2e}\right)\left(\frac{2}{\gamma e}\right)^2\left(\frac{2}{7}\frac{\kappa_{0e}}{L_{||}}\right)^{4/7}\frac{q_{||}^{10/7}}{n_u^2} \\ n_t = \frac{n_u T_u}{2T_t} = \left(\frac{e}{m_i}\right)\left(\frac{\gamma e}{2}\right)^2\left(\frac{7}{2}\frac{L_{||}}{\kappa_{0e}}\right)^{6/7}\frac{n_u^3}{q_{||}^{8/7}} \\ T_u = \left(\frac{7}{2}\frac{q_{||}L_{||}}{\kappa_{0e}}\right)^{2/7} \end{cases} \tag{2.65}$$

As anticipated, the upstream temperature does not depend on the upstream density. In this regime T_u is a function of only the geometry of the machine and the power that flows from the core into the SOL. For the target parameters, the overall monotony is maintained. However, in this case we observe more strong trends. The density at the target increases more than linearly with n_u ($n_t \propto n_u^3$), whereas the temperature is inversely proportional with the upstream density squared ($T_t \propto n_u^{-2}$). This operative condition is particularly interesting from a practical point of view. In fact, while in the first regime high plasma temperature far from the sheath resulted in very hot plasma at the wall, in this domain we can preserve high performances in the core while decreasing the thermal energy of the particles at the solid boundary. The temperature drop allows to operate the machine with

only cold plasma interacting with the plasma facing materials. Such advantage means less erosion of the equipment and therefore an increased lifetime of the components. However, we must keep in mind that the heat flux is invariant between the two regimes. The decrease of temperature at the target position is the consequence of the dilution of heat inside the plasma due to the increased density. The overall flow of energy has not changed.

Now, considering an experimental situation where the heat flux decreases at the solid plate, we have to include in the model some kind of energy sink inside the SOL (e.g. radiation losses). From the existing drop of temperature we deduce that the heat is mainly conducted along the field lines, reason why this regime is also called conduction-limited. This condition can occur only if most of the ionization of neutrals takes place near the target. The particle flow would therefore be relevant only in a distance range of one ionization mean free path from the solid wall. The steady state operation would be reached when the plasma out flow from the SOL will be equal to the flux of neutrals coming from the target. The plasma would sustain itself through recycling, so far as particles are concerned. Thus this low T_t regime will also be an high recycling regime. The high rate of recycling is in itself of no obvious advantage, but that is the main agent that allows the build up of the temperature drop inside SOL.

2.2.6 The transition between the sheath-limited and the high-recycling regime

The different assumptions that define each of the two introduced regimes are based on the comparison between the temperatures T_u and T_t. However from the plotted solution of two point model we observe that the transition is not at all gradual. There is a threshold value which needs still to be quantified. Therefore this paragraph will focus on evaluating the limit after which we can consider the target temperature to be negligible in respect to the upstream one. As specified in [21] the physical phenomenon that determines the transition between regimes is the collisionality of plasma inside the SOL. In particular [10] defines a threshold value for the SOL collisionality parameters based on upstream plasma values.

This quantity is defined as:

$$\nu^*_{SOL} = \frac{L_{||}}{\lambda_{ee}} \sim 10^{-6} \frac{n_u L_{||}}{T_u^2} \tag{2.66}$$

Where $n[m^{-3}]$, $T[eV]$, $\lambda_{ee}[m] \sim 10^6 \frac{T^2}{n}$ is the mean free path between electron-electron Coulomb collisions (same as the one for ion-ion interaction $\lambda_{ee} \sim \lambda_{ii}$). Using the two point model we can derive a relation between the quantity $\frac{n_u L_{||}}{T_u^2}$ and the rate between upstream and target temperature $f_T = \frac{T_u}{T_t}$. The conduction equation and the sheath condition can be written as:

$$\begin{aligned} q_{||} &= \frac{2}{7} \kappa_{0e} \frac{T_t^{7/2} \Big(f_T^{2/7} - 1 \Big)}{L_{||}} \\ q_{||} &= \gamma n_t e T_t \sqrt{\frac{2eT_t}{m_i}} \\ &= \gamma n_t e \sqrt{\frac{2e}{m_i}} T_t^{3/2} \end{aligned} \tag{2.67}$$

Which, eliminating $q_{||}$, becomes:

$$\frac{n_t L_{||}}{T_t^2} = \frac{2}{7} \sqrt{\frac{m_i}{2e}} \frac{\kappa_{0e}}{\gamma e} \Big(f_T^{7/2} - 1 \Big) \tag{2.68}$$

The momentum conservation equation, similarly can assume the following form:

$$\begin{aligned} 2 n_t T_t &= n_u T_u \\ \frac{n_t}{T_t^2} &= \frac{1}{2} \frac{n_u}{T_u^2} f_T^3 \end{aligned} \tag{2.69}$$

Which combined with the previous relation gives:

$$\frac{n_u L_{||}}{T_u^2} = \frac{4}{7} \sqrt{\frac{m_i}{2e}} \frac{\kappa_{0e}}{\gamma e} f_T^{-3} \Big(f_T^{7/2} - 1 \Big) \tag{2.70}$$

Remembering equation (1.61) we finally reach an expression that correlates the SOL collisionality with the temperature rate, which is also plotted in figure (1.8):

$$\nu^*_{SOL} \sim 10^{-6} \frac{4}{7} \sqrt{\frac{m_i}{2e}} \frac{\kappa_{0e}}{\gamma e} f_T^{-3} \Big(f_T^{7/2} - 1 \Big) \tag{2.71}$$

From [1] we see that the threshold value for the SOL collisionality is around 10. We

can derive through equation 2.71 the rate of temperature after which we have the transition between regimes: $f_T \sim 1.52$ at $\nu^*_{SOL} = 10$. We conclude that we can consider the target temperature to be negligible in respect to the upstream one when the latter is $\sim 50\%$ higher. One could have thought that from the high-recycling regime assumption the temperature rate should have been substantially higher than one ($T_u \gg T_t$; $f_T = \frac{T_u}{T_t} \gg 1$). However this is not the case because of the high non linearity in one of the equation of the two point model ($q_{||} \propto T^{7/2}$). Therefore even for small temperature drop, the heat flux transferred through conduction can be relevant:

$$q_{||} \propto T_u^{7/2}\Big(1 - \frac{1}{f_T^{7/2}}\Big) \tag{2.72}$$

A simpler (but non-physical) definition of the temperature rate during transition could have been made through a condition on the temperature upstream. If we define the reference temperature T_q as:

$$T_q = \Big(\frac{7}{2}\frac{q_{||}L_{||}}{\kappa_{0e}}\Big) \tag{2.73}$$

The heat conduction equation could be written as:

$$\begin{aligned} T_u^{7/2} - T_t^{7/2} &= \frac{7}{2}\frac{q_{||}L_{||}}{\kappa_{0e}} \\ \Big(\frac{T_u}{T_q}\Big)^{7/2} - \Big(\frac{T_t}{T_q}\Big)^{7/2} &= 1 \end{aligned} \tag{2.74}$$

The density regimes will be than defined form different, but analogous, conditions:

$$\begin{cases} T_u \gg T_q & \text{in the sheath-limtied regime} \\ T_u \sim T_q & \text{in the high-recycling regime} \end{cases} \tag{2.75}$$

This formulation tells us that the transition can be identified also by how the upstream temperature is distance from the reference temperature. From last equation it is possible to express the rate T_u/T_q as a function of f_T :

$$\frac{T_u}{T_q} = \frac{1}{\Big(1 - \frac{1}{f_T^{7/2}}\Big)^{2/7}} \tag{2.76}$$

We can also express, using equations 2.65 the transition between the regimes as a function of the control parameter, upstream density and heat flux. Assuming a threshold temperature rate of ~ 1.5, we get:

$$\begin{aligned} T_t &\ll T_u \\ 1.5T_t &\leq T_u \\ \frac{3m_i q_{||}^{10/8}}{\gamma^2 e^2 n_u^2}\Big(\frac{2}{7}\frac{\kappa_{0e}}{L_{||}}\Big)^{4/7} &\leq \Big(\frac{7}{2}\frac{q_{||}L_{||}}{\kappa_{0e}}\Big)^{2/7} \end{aligned} \tag{2.77}$$

Which can be translated in a condition on the upstream density:

$$n_u \geq \frac{\sqrt{3m_i}}{\gamma e^{3/2}}\Big(\frac{2}{7}\frac{2\kappa_{0e}}{7L_{||}}\Big)^{3/7} q_{||}^{4/7} = n_u^* \tag{2.78}$$

2.3 The modified Two Point Model

The strict assumptions of the two point model may be alleviated by introducing corrections into the model. In the simplest case, they have the form of three correction factors: f_{mom}, which allows for pressure imbalance by introducing momentum losses, f_{cond}, which allows for transport to be larger than conduction would carry, hence introducing convective transport, and f_{pow}, which allows for power losses between upstream and downstream.

The definition of f_{mom} is straightforward. For the pressure downstream being lower than upstream due to momentum losses, we define f_{mom} as

$$f_{mom} = \frac{p_t}{p_u} \tag{2.79}$$

Thus defined f_{mom} ranges from 0 (all pressure is lost) to 1 (all pressure is preserved).

The power loss factor f_{pow} is defined in a similar way, through the dissipation of heat flux along the flux tube. Its original definition by Stangeby [10], $q_{lost} = f_{pow} q_{||u}$, leads to a slightly counter-intuitive form

$$1 - f_{pow} = \frac{q_{||t}}{q_{||u}}. \tag{2.80}$$

(In the case of the heating power being distributed uniformly along the separatrix, $q_{||u}$ is replaced by $q_{||X-point}$). Thus defined $1 - f_{pow}$ gains values from 0 (all power lost before reaching target) to 1 (all power preserved).

Finally, the conduction factor f_{cond} represents the fraction of the total parallel heat flux which is conducted,

$$f_{cond} = \frac{q_{||cond,u}}{q_{||u}} \tag{2.81}$$

Upstream values of heat flux are used because the transport character is assumed to change from mostly conductive to fully convective adjacent to the sheath entrance, and thus the target values cannot be used directly. The conduction factor allows for non-zero plasma velocity in the majority of the flux tube, as part of the upstream heat flux is carried in the convective form.

Introducing the loss factors into the equations of the two point model is straightforward in the case of momentum losses and power losses, since they are defined directly as the inequality of the two sides of equations 2.48 and first- 2.58 . While equation 2.57 does represent the assumption that heat flux is driven solely by the gradient in temperatures between upstream and downstream, it was derived by integrating equation 2.55 while assuming that $q_{||cond}$ is constant along the entire flux tube. This may no longer be true since power losses along the entire flux tube are allowed. We solve this conundrum by assuming, in accordance with [10], that power losses occur close to the target (below X-point) 1. In this case, $q_{||} = q_{||u}$ in the majority of the flux tube. This is the heat flux appearing in equation 2.57, and thus $1 - f_{pow}$ does not appear in the corrected equation.

Assuming power entering uniformly through the separatrix, the equations of the two-point model can be expressed as follows:

$$\begin{cases} n_u T_u = 2 n_t T_t f_{mom} \\ T_u^{7/2} = T_t^{7/2} + \dfrac{7}{4} \dfrac{q_{||u} L_{||}}{\kappa_{0e}} f_{cond} \\ q_{||u} = \gamma n_t k_B T_t c_{s,t} (1 - f_{pow}) \end{cases} \tag{2.82}$$

2.3.1 Separatrix temperature determination using the Two Point Model

For TPM:

$$\begin{cases} T_u^{7/2} & = T_t^{7/2} + \frac{7}{2}\frac{q_{||}L_{||}}{\kappa_{0e}}, \\ 2n_tT_t & = n_uT_u, \\ q_{||} & = q_t = \gamma n_t k T_t c_{s,t} \end{cases} \tag{2.83}$$

$$\begin{cases} T_u^{7/2} = T_t^{7/2} + \frac{7}{2}\frac{q_{||}L_{||}}{\kappa_{0e}}, \\ T_t = \left(\frac{2q_{||}}{\gamma e n_u T_u}\sqrt{\frac{m_i}{2e}}\right)^2 \end{cases} \tag{2.84}$$

$$T_u^{7/2} = \left(\frac{q_{||}}{n_u e}\sqrt{\frac{m_i}{2e}}\right)\frac{1}{T_u^7} + \frac{7}{2}\frac{q_{||}L_{||}}{\kappa_{0e}} \tag{2.85}$$

$$\frac{2}{\gamma e}\sqrt{\frac{m_i}{2e}}\left(\frac{q_{||,SEP}}{n_{e,SEP}}\right)^7 + \left(\frac{7L_{||}}{2\kappa_{0e}}\right)q_{||,SEP}\eta^2 - \eta^3 = 0 \tag{2.86}$$

where $\eta = T_{e,SEP}^{7/2}$, $q_{||,SEP} = \frac{1/4P_{SOL}}{A} = \frac{1/4P_{SOL}}{2\pi R\lambda_q}\frac{|B|}{B_P}$ For modified-TPM:

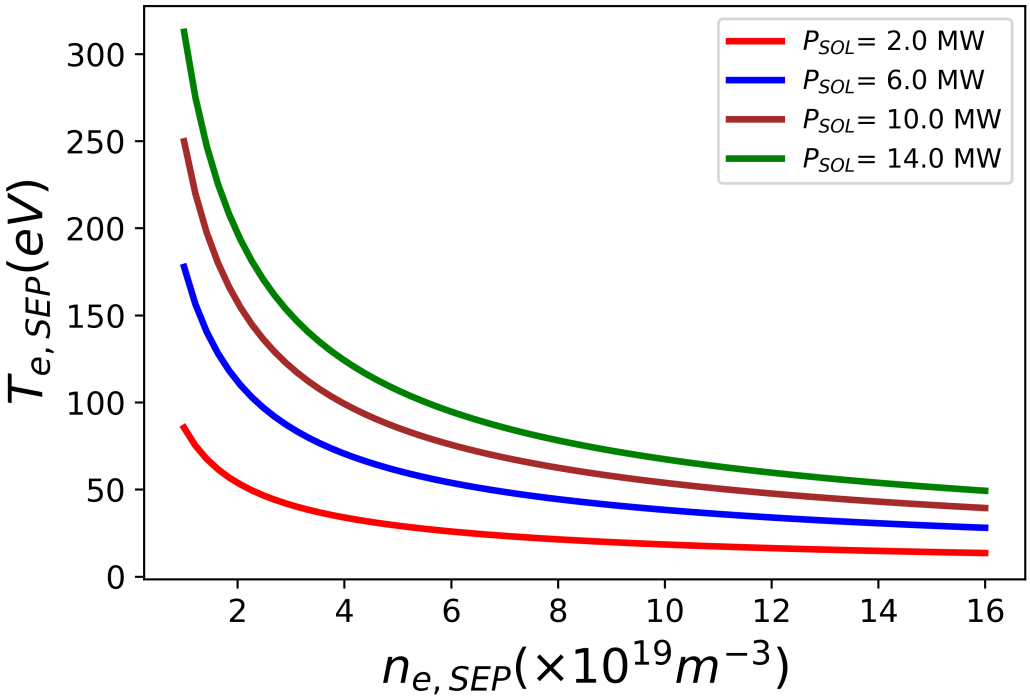

Figure 2.1: Two-point model illustration.

B_T	I_P	q_{95}	λ_q
$3.0T$	$3.0MA$	3.5	$2.5mm$

Table 2.1: Values set for two-pint model illustration.

$$\begin{cases} T_u^{7/2} & = T_t^{7/2} + \frac{7}{2}\frac{f_{cond} q_{||} L_{||}}{\kappa_{0e}}, \\ 2 n_t T_t & = f_{mom} n_u T_u, \\ (1 - f_{pow}) q_{||} & = q_t = \gamma n_t k T_t c_{s,t} \end{cases} \tag{2.87}$$

$$\begin{cases} T_u^{7/2} & = T_t^{7/2} + \frac{7}{2}\frac{f_{cond} q_{||} L_{||}}{\kappa_{0e}}, \\ T_t & = \big(\frac{2(1-f_{pow}) q_{||}}{\gamma e f_{mom} n_u T_u}\sqrt{\frac{m_i}{2e}}\big)^2 \end{cases} \tag{2.88}$$

$$\big(\frac{2}{\gamma e}\sqrt{\frac{m_i}{2e}}\big)^7 \big(\frac{1 - f_{pow}}{f_{mom}}\big)^7 \big(\frac{q_{||,SEP}}{n_{e,SEP}}\big)^7 + \big(\frac{7 L_{||}}{2\kappa_{0e}}\big) f_{cond} q_{||,SEP} \eta^2 - \eta^3 = 0 \tag{2.89}$$

where $\eta = T_{e,SEP}^{7/2}$.

Asymptotic cases for temperature-density relation

For asymptotic analysis of the electron separatrix temperature evolution inside the two-point model framework the equation 2.86 is used as follow:

$$\frac{2}{\gamma e}\sqrt{\frac{m_i}{2e}}\big(\frac{q_{||,SEP}}{n_{e,SEP}}\big)^7 + \big(\frac{7 L_{||}}{2\kappa_{0e}}\big) q_{||,SEP} \eta^2 - \eta^3 = 0$$

whith $q_{||,SEP} = \frac{1/4 P_{SOL}}{A} \approx \hat{f} P_{SOL}$, $\hat{f} = 1/(4A)$. The equation 2.86 is transformed to:

$$\eta^3 - C^{(2)} P_{SOL} \eta^2 - C^{(0)} \big(\frac{P_{SOL}}{n_{e,SEP}}\big)^7 = 0$$

$$\text{where } C^{(0)} = \hat{f}^7 (2/\gamma e)\sqrt{m_i/2e} \quad \text{and} \quad C^{(2)} = \hat{f}(7 L_{||}/2\kappa_{0e}).$$

Assuming a small increment in P_{SOL} an increment in η is envisaged then this hypothetical case is summarized as if $P_{SOL} \Rightarrow P_{SOL} + \Delta P_{SOL}$ then $\eta \Rightarrow \eta + \Delta\eta$, it let us form the next

equation system:

$$\eta^3 - C^{(2)} P_{SOL} \eta^2 - C^{(0)} \big(\frac{P_{SOL}}{n_{e,SEP}}\big)^7 = 0$$
$$(\eta + \Delta\eta)^3 - C^{(2)}(P_{SOL} + \Delta P_{SOL})(\eta + \Delta\eta)^2 - \frac{C^{(0)}}{n_{e,SEP}^7}\big(P_{SOL} + \Delta P_{SOL}\big)^7 = 0 \qquad (2.90)$$
$$\text{with conditions of 'small' for:} \quad \frac{|\Delta P_{SOL}|}{P_{SOL}}, \frac{|\Delta\eta|}{\eta} \ll 1.$$

Applying the approximation for small variations on P_{SOL} and η expressions we have:

$$\big(1 + \frac{P_{SOL}}{\Delta P_{SOL}}\big)^7 \approx 1 + 7\frac{P_{SOL}}{\Delta P_{SOL}}$$
$$\big(1 + \frac{\eta}{\Delta\eta}\big)^3 \approx 1 + 3\frac{\eta}{\Delta\eta}$$

Then using equations 2.90 the variation of η can be expressed as a implicit equation containing terms of P_{SOL}, ΔP_{SOL} and $n_{e,SEP}$, the expression is:

$$\Delta\eta = \frac{\Delta P_{SOL}\big(C^2\eta^2 + 7\frac{C^{(0)}P_{SOL}^6}{n_{e,SEP}^7}\big)}{\eta(3\eta - 2C^{(2)}(P_{SOL} - \Delta P_{SOL}))} \qquad (2.91)$$

like $\eta = T_{e,SEP}^{7/2}$ then:

$$\Delta T_{e,SEP} = \frac{2}{7}\frac{\Delta P_{SOL}}{T_{e,SEP}^6}\frac{\big(C^2 T_{e,SEP}^7 + 7\frac{C^{(0)}P_{SOL}^6}{n_{e,SEP}^7}\big)}{(3T_{e,SEP}^{7/2} - 2C^{(2)}(P_{SOL} - \Delta P_{SOL}))}. \qquad (2.92)$$

The final expression might be split in two terms:

$$\Delta T_{e,SEP} = \frac{2C^{(0)}\Delta P_{SOL} P_{SOL}}{(3T_{e,SEP}^{7/2} - 2C^{(2)}(P_{SOL} - \Delta P_{SOL}))}\Big(\frac{1}{n_{e,SEP}^7}\Big) + \Big[\frac{2C^{(2)}}{7}\Delta P_{SOL}\Big]\frac{T_{e,SEP}^{7/2}}{(3T_{e,SEP}^{7/2} - 2C^{(2)}(P_{SOL} - \Delta P_{SOL}))} \qquad (2.93)$$

Primarily the inverse dependence between $T_{e,SEP}$ and $n_{e,SEP}$ is clear unber the two-point model framework. Assuming the asymptotic cases for $n_{e,SEP}$:

. $n_{e,SEP}^7 \to 0 \Rightarrow 1/n_{e,SEP}^7 \to \infty$ then

$$\Delta T_{e,SEP}^{n_{e,SEP}|min} \approx \frac{2C^{(0)}\Delta P_{SOL} P_{SOL}}{(3T_{e,SEP}^{7/2} - 2C^{(2)}(P_{SOL} - \Delta P_{SOL}))}\Big(\frac{1}{n_{e,SEP}^7}\Big) \qquad (2.94)$$

. $n_{e,SEP}^7 \to \infty \Rightarrow 1/n_{e,SEP}^7 \to 0$ then

$$\Delta T_{e,SEP}^{n_{e,SEP}|_{max}} \approx \Big[\frac{2C^{(2)}}{7}\Delta P_{SOL}\Big]\frac{T_{e,SEP}^{7/2}}{(3T_{e,SEP}^{7/2} - 2C^{(2)}(P_{SOL} - \Delta P_{SOL}))} \tag{2.95}$$

Despite $T_{e,SEP}$ is different for $n_{e,SEP}|_{min}$ and $n_{e,SEP}|_{max}$, their variation is not in the range of $n_{e,SEP}^7$ then

$$\frac{\Delta T_{e,SEP}^{n_{e,SEP}|_{min}}}{\Delta T_{e,SEP}^{n_{e,SEP}|_{max}}} \approx \frac{P_{SOL}}{T_{e,SEP}^{7/2}}\Big(\frac{1}{n_{e,SEP}^7}\Big)$$
$$\text{with} \quad \frac{1}{n_{e,SEP}^7} \gg 1,$$

neglecting the effect of P_{SOL} and $T_{e,SEP}^{7/2}$:

$$\Delta T_{e,SEP}^{n_{e,SEP}|_{min}} \gg \Delta T_{e,SEP}^{n_{e,SEP}|_{max}} \tag{2.96}$$

nevertheless when P_{SOL} is small the term $T_{e,SEP}^{7/2}$ dropping down faster and the ratio $P_{SOL}/T_{e,SEP}^{7/2}$ increase leading the difference between $\Delta T_{e,SEP}^{n_{e,SEP}|_{min}}$ and $\Delta T_{e,SEP}^{n_{e,SEP}|_{max}}$ to :

$$\Delta T_{e,SEP}^{n_{e,SEP}|_{min}} > \Delta T_{e,SEP}^{n_{e,SEP}|_{max}} \tag{2.97}$$

2.4 Pedestal region and edge barrier in H-mode

In 1982, during high beta in Neutral-Beam-Heated divertor discharges the H-mode was observed in ASDEX [22]. During the ASDEX experiment [22] the confinement regime showed a link with auxiliary heating by means a power threshold, P_{th}, since, e.g., for input power larger than P_{th} the confinement time, t_{conf}, increases by a factor of 2 to 3 [23] and other features are revealed.

Taking P_{th} as a reference the confinement regime might be split in two modes, the first one is low-confinement mode, L-mode, for input power lower than P_{th} and the another one is high-confinement mode, H-mode, for input power larger than P_{th}.

For L-mode confinement regime some auxiliary heated tokamak experiments bring evidence

of linear increasing behavior with plasma current and a degradation of confinement regime with increasing of power [22] and it is indicated in JET and JFT-2M limiter H-modes, nevertheless no power dependence is found in ASDEX and DIII-D [24].

$$\text{L-mode:} \quad \tau_{conf} \propto \frac{I_P}{\sqrt{P_{input}}}.[25] \tag{2.98}$$

During the H-mode confinement regime the confinement time increases by a factor of 2 to 3 respect to L-mode, the plasma edge fluctuations decrease considerably, and there is a formation of a transport barrier at the plasma edge [23] leading to pedestals in the density and temperature profiles [24] on decreasing of plasma edge fluctuations. Also the decreasing of plasma of plasma edge fluctuations is important for the power balance separatrix determination since the error of power balance is in the same order than fluctuations.

The L-mode transition is almost instantaneous [23], less than 2 ms [24], the power threshold scales with toroidal magnetic field and density:

$$P_{Th} \propto B_T n \quad [26,\ 27] \tag{2.99}$$

The transition seems to be independent of heating method and magnetic field geometry [28, 23]. A cause for the formation of the edge transport barrier can be the formation of an edge $E_r^{'}$ layer with $E_r^{'}$ as a radial electric field shear [23]. There is a well correlation between the region of strong shear with steep density gradient region and the fluctuation supression [29, 23]. The $E_r^{'}$ layer formation leads an onset of a poloidal flow in the edge layer, correlating H-mode operation with parallel transport.

Many theoretical frameworks for the L to H transition are based on enhanced eddy correlation induced by the shear electric field with the consequent turbulence suppression [30, 23]. The most described casual mechanism for the L to H transition by effect of radial electric field, first described in [31, 32, 33], is:

- At a certain level of power injection in a tokamak, the edge particle losses or poloidal asymmetry create or modify the radial electric field.

- This electric field is then responsible for the reduction of the fluctuation level and transport.

Also it is shown that turbulence can modify the profile of average flows through Reynolds stress [34, 35], then for numerical goals the electric field profile and turbulence shall be calculated self-consistently.

2.4.1 High confinement regime and ELMs

Summarizing, the H-mode is a bifurcated plasma state and an important feature of H-mode, as is shown in figure 2.2, is a repetitive expulsion of particles and energy like bursts from the plasma periphery leaded by some kind of MHD instability at the plasma edge and have therefore been called ELMs (Edge-localized modes).
ELMs periodically deprecate the particle and energy confinement in the outer parts of the plasma thereby limiting the rise in plasma density and energy and reducing the accumulation of impurities in the plasma interior.
Among the H-mode discharges so far observed on different tokamaks and under various experimental conditions one can distinguish H-modes with and without ELMs. As pointed out before, H-discharges with ELMs - which are the usual case, for example, on ASDEX [36] facilitate reaching quasi-stationary conditions and long H-mode periods but at the expense of somewhat degraded H-mode confinement. H-modes without ELMs, on the other hand, - typical for example, of JET and DIII-D [37, 38] which have better confinement, are characterized by a continuous rise in plasma density and a concomitant increase in bulk plasma radiation which finally terminates the H-mode when the radiation losses exceed some fraction of the input power.

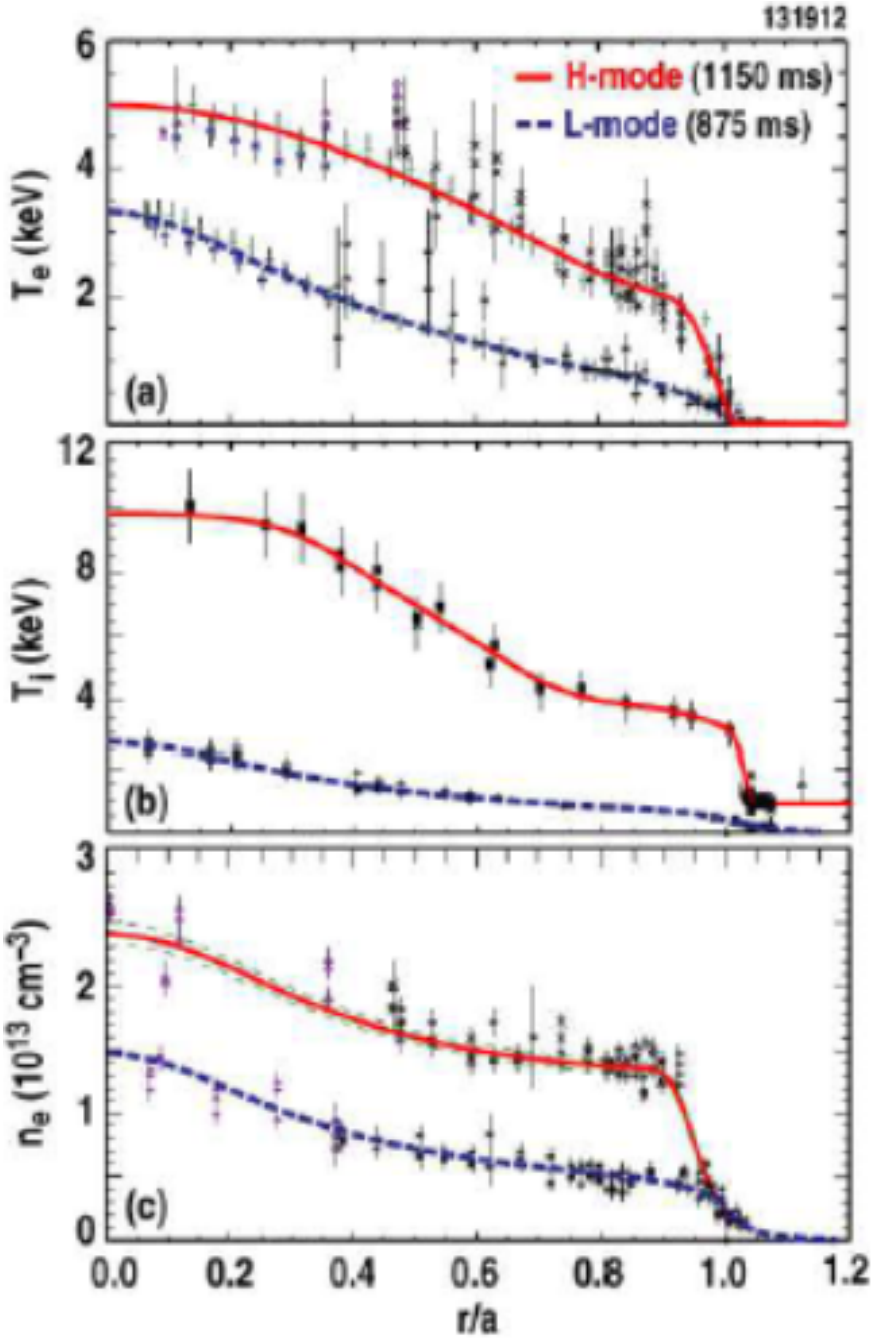

Figure 2.2: Radial profiles of (a) electron temperature from core plasma Thomson scattering data (triangles and x-symbols), and electron cyclotron emission (ECE, horizontal bars), (b) ion temperature from CHERS, and (c) electron density from core plasma Thomson scattering in L-mode (875 ms, dashed line) and H-mode (1150 ms, solid line). Figure from [L. Schmitz et al. Nucl. Fusion, 52, 2012.]. This two regimes might be interpreted like two bifurcated states of plasma depending of the operation conditions

2.4.2 Quality of confinement and H98 factor

The energy confinement time of a tokamak is a central quantity of plasma execution. Generally it is looked in terms of the "H_{98}-factor": the ratio between the measured confinement time and that expected from the $IPB_{98}(y,2)$ scaling [39]. The quality of confinement, expressed by the H-factor $H_{98} = \tau_E/\tau_{IPB_{98}(y,2)}$, i.e. the value of τ_E compared to the scaling law prediction [40]. The scaling law prediction by $IPB_{98}(y,2)$ is given by

$$\begin{aligned}\tau_{IPB_{98}(y,2)} =& 0.0562 \times I^{0.93} B^{0.15} n^{0.41} P^{-0.69} \\ & \times R^{1.97} \kappa^{0.78} \epsilon^{0.58} M^{0.19}\end{aligned} \tag{2.100}$$

where I is plasma current (in MA), R is major radius (in m), inverse aspect ratio $\epsilon = a/R$, Elongation (κ), B is toroidal magnetic field (in T), n is electron density (in $10^{19}\mathrm{m}^{-3}$), P is heating power or loss power (in MW) and M is ion mass number [41].

ITER was designed using $H_{98} = 1.0$ [42] but ITER has significant flexibility that means advanced plasma scenarios with plasma performance of $H_{98} \sim 1.57$ are now predicted in reversed shear operation [43]. $H_{98} \sim 1.8$ has also been suggested in the context of an "advanced tokamak" [44] justified by the large H_{98}-factors achieved in DIII-D [45].

Chapter 3

Experimental setup: the JET and TCV tokamaks

In this chapter, we present two different machines, JET and TCV, different in several aspects. This will allow us in the second part of the manuscript to analyze data from both of them and considering also a general scaling law which encompasses the conditions of both tokamaks. The JET tokamak is the largest single project within the EUROFUSION programme and It was coordinated by Euratom (the European Atomic Energy Community). Operations began in 1983 being the pioneer fusion facility in the world to achieve a milestone of production of controlled fusion power, almost 2 MW, with a D-T experiment in 1991. Later 1991, JET was upgraded by the installation of a divertor to operate higher levels of exhaust power. Experiments with Deuterium in the ITER geometry have made crucial contributions to the ITER divertor design and supplied critical data of heating, confinement and fueling. This has contributed substantially to the set of the size, heating requirements and operating conditions of ITER [46, 47].

Pending 1997 the JET operations involved a successful campaign with experiments using a range of D-T fuel mixtures. During this campaign it was achieved three new 'world record':

- 22 MJ of fusion energy in one pulse.
- 16 MW of peak fusion power.
- a 65% ratio of fusion power produced to total input power, $Q \approx 0.65$,.

The JET tokamak operates in a pulse mode, and pulses can be reproduced at maximum rate of about one every twenty minutes and each one can last for up to 60 seconds in duration, however the energy confinement time is about 1-2s. It is officially defined as the ratio of the thermal energy contained in the plasma and the power losses. The importance of JET tokamak for the aim of this thesis lies in the extensive range existing for the engineering parameters since it allows to produce reliable empirical scalings using the available data.
On the side of TCV tokamak, it is a Swiss research fusion reactor of the Ecole Polytechnique Fédérale de Lausanne (EPFL). Its distinguishing attribute compared to other tokamaks is that its torus section is three times higher than wide. This lets study several shapes of plasmas, which is particularly relevant since the shape of the plasma has links to the performance of the reactor. This advantage has earned its choice as one of the three national machines in Europe involved in the design of the international reactor ITER [r3], as well as in the development of ITER's successor DEMO, a prototype of a commercial reactor. The TCV was set up in November 1992.

JET Tokamak	
Technical Data	
Major plasma radius	2.96 m
Minor radii	1.25/2.10 m
Magnetic field	3.4 T
Plasma current	5.0 MA
Plasma heating	50 MW
Plasma volume	$80m^3$
Plasma Mixture	Hydrogen, Deuterium, Tritium
Plasma temperature	$100 - 200 \times 10^6 C^o$

Table 3.1: Technical Values of JET tokamak

TCV Tokamak	
Technical Data	
Major plasma radius	0.89 m
Minor radii	0.25 m
Maximal on axis magnetic field	1.54 T
Maximal plasma current	1.2 MA
Plasma heating - Ohmic (OH)	Up to 1 MW
Plasma heating - Electron Cycl. (ECH)	Up to 4.5 MW
Aspect ratio	3.5
Main ion component	Hydrogen, Deuterium, Helium
Core electron temperature	$\leq 1keV$ (ohmic)
Core electron temperature	$\leq 15keV$ (ECH)

Table 3.2: Technical Values of TCV tokamak

3.1 Heating system and principles of Neutral Beam Injection

The neutral beam heating system is a heating plasma method, this system heats plasma inside fusion devices despite of the magnetic confinement field, it consists of high energy particles neutral beam. The neutral particles injected into the plasma are ionized by collision with the original plasma particles and they are also confined by the magnetic field then remaining in the plasma and might transfer their energy to the whole plasma by further collisions.

A complementary contribution of the neutral beam injection is the momentum provided to the plasma by tangential injection in the torus, current drive is also affected by momentum contribution and it is essential in special for long pulses of plasmas.

Neutral beam injection is an adaptable and trustable technique, whereby it has been used in many fusion devices as the main heating system. The regular mechanism for the neutral beam formation is shown in 3.1 and summarized here below in four steps scheme:

1. **Making a plasma**. This can be done by microwaving a low pressure gas.

2. **Electrostatic ion acceleration**. This is done dropping the positively charged ions towards negative plates. As the ions fall, the electric field does work on them, heating them to fusion temperatures.

3. **Reneutralizing**. The hot plasma by adding in the opposite charge. This gives the fast-moving beam with no charge.

4. **Injecting**. The fast moving hot neutral beam in the machine.

There is a critical importance to inject neutral particles into plasma since whether non-neutral material is injected then harmful plasma instabilities can start and some energetic particles can run-off plasma before they spread their energy in the whole plasma. Whereas

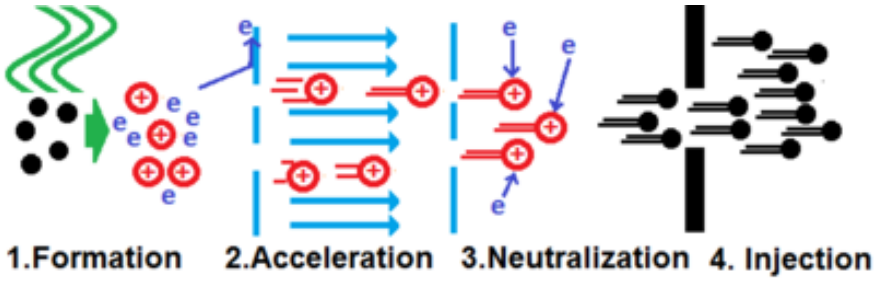

Figure 3.1: Neutral Beam Injection mechanism

circular shape of magnetic field, fast particles are confined in the background of plasma transfering their energy and increasing the overall plasma temperature.

3.1.1 Neutral Beam in JET

The Neutral Beam system is located in Octants 4 and 8 of the JET torus, with Octant 4 designated YC and Octant 8 designated AH.. Each octant contains a Neutral Injector Box (NIB) containing 8 Positive Ion Neutral Injectors (PINIs) in 2 stacks; the normal bank (tangent radius RT = 1.31m) and the tangential or "tan" bank (RT = 1.85m). On each octant the normal bank contains PINIs 3,4,5,6 and the tan bank contains PINIs 1,2,7,8. The system has a theoretical maximum of 32MW of beam power. Figure 1 shows a simple model of the NBI system geometry.

Each beam is formed in the PINI, a particle accelerator which uses several high voltage grids to accelerate positively charged particles. The end of the PINI is taken to be the final grid, grid 3. The beam then enters the neutraliser which converts part of the beam into neutral particles via charge exchange interactions. The beam then enters the NBI, where a bending magnet diverts the remaining charged part of the beam onto energy dumps. The NIB also contains the calorimeter, a movable ion dump where the power profile of the beam can be measured. The beam then passes through the rotary valve and duct and into the torus. Along the beamline there are several 'scrapers' which block certain outer parts of the beam so it fits through without excessively heat loading the surrounding components.

Each beam actually consists of two beams, as the grids are formed of two independent

half grids, and hence there are two independent horizontal alignments for each PINI. These two halves of the beam then converge within the torus.

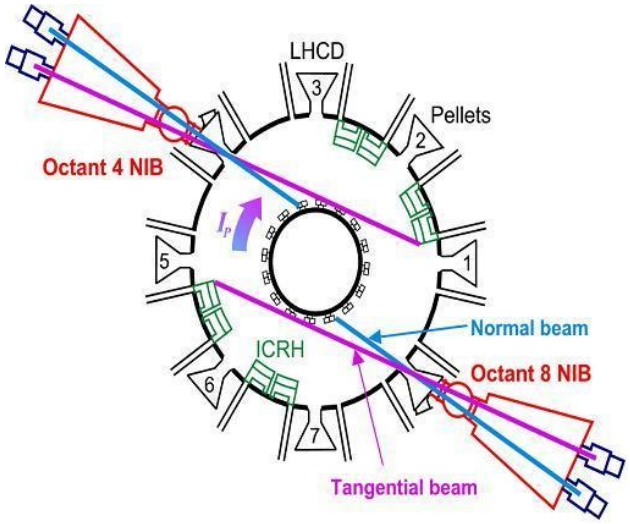

Figure 3.2: Neutral Beam scheme

3.1.2 Neutral Beam in TCV

The neutral beam injection system in TCV has two sources for plasma creation, one is generated by RF in Neutral Beam Heating (NBH) system and the another one is by ARC discharge in the Diagnostic Neutral Beam Injector (DNBI) system. The plasma in the source of NBI is formed from neutrals, electrons, fully ionised atoms (H^+ or D^+) and ionized molecules like D^{2+}, D^{3+}, D_2O^+, or H, etc. An extraction of ions are applied on the beam, and when the neutral beam has reached the whole confined plasma the fast neutral particles emit $H_\alpha(D_\alpha)$ lines. The scheme of the injection of the neutral beam system in plasma is shown in figure 3.3 and the characteristics of the NBI system is:

1. Max. NB power injected in TCV - 1.2 MW.

2. Nominal beam energy - 27.8 keV.

3. Max. NB pulse duration - 2 sec.

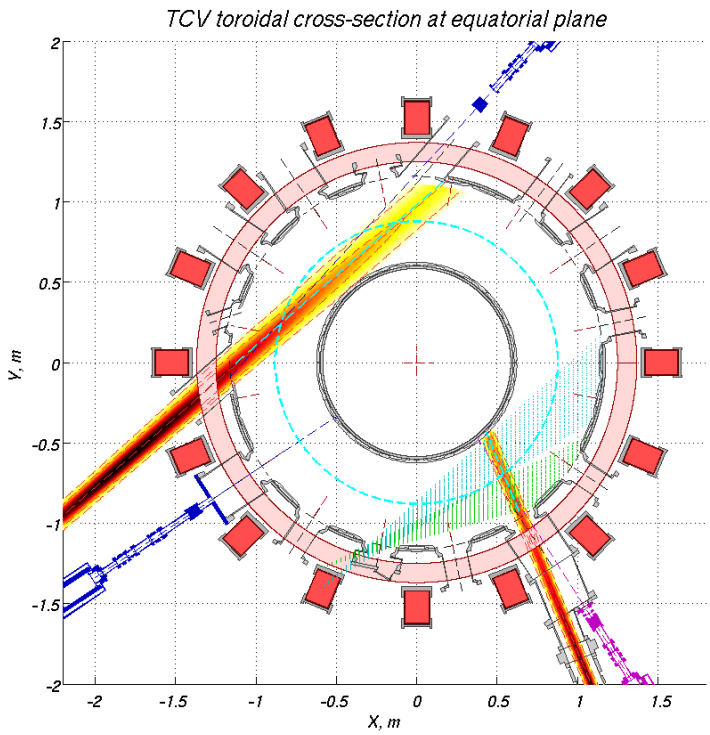

Figure 3.3: Neutral Beam scheme in TCV

4. Neutral power fraction at full 75%, half - 20%, third - 5%, low (1/(12...18) - ¡ 0.05% energies for 1.28 MW.

5. Power losses in beam duct - $8 - 15\%$ must be excluded from injector neutral power.

3.2 High-resolution Thomson scattering

3.2.1 Principles

Thomson scattering is an elastic scattering of electromagnetic radiation by a free charged particle [48]. Thomson scattering is a low-energy approximation of Compton scattering, where the kinetic energy of free-particle and photon energy is neglectable to mass energy of the particle, $h\nu << mc^2 \Rightarrow \nu << mc^2/h$ [49].

For low-energy limit, the electric field of the incident wave accelerates the charged particle, breeding it, to emit electromagnetic radiation with equivalent frequency as the incident wave, thereby the wave is scattered. Since motion of the particle is non-relativistic the ac-

celeration of the particle will be due to the electric field component of the incident wave. In a first approximation, the influence of the magnetic field can be neglected. The particle will move in the direction of the oscillating electric field, resulting in electromagnetic dipole radiation. The moving particle radiates most strongly in a direction perpendicular to its acceleration and that radiation will be polarized along the direction of its motion. In tokamaks, the electron temperature and density in plasma might be measure with high accuracy by detecting effects of Thomson scattering for high-intensity laser beam.

Thomson scattering diagnostic is a laser-aided diagnostic widely used in the field of high-temperature plasma diagnostic [50]. Perform well-localized measurements of the electron temperature and density in the plasma. Scattering of monochromatic electromagnetic radiation from hot-electrons in a plasma leads to a spectral broadening of the scattering spectrum due to the Doppler effect. Electron temperature is determined from a spectral width of the Thomson signal, electron density from scattered signal intensity [50].

The temporal evolution of the T_e and n_e spatial profiles is important for understanding the physics of plasma, so multiple lasers systems in which the time between pulses is less than the energy-confinement time become very attractive [51, 52].

Therefore many Thomson-scattering systems use Nd lasers that allow for high repetition rates ($\leq 10Hz$), with energies $\leq 1J/pulse$ and low divergence to minimize the beam waist into the plasma. A laser wavelength in the near infrared also yields a reliable signal-to-noise ratio because the background plasma light is lower than in the visible range of the wave length [53].

For the case of horizontal Thomson scattering the plasma axis moves through the laser beam as a consequence of time-dependent Shafranov-shift, but this problem is solved using an auxiliary vertical laser system for the acquisition of the signals [51].

As fusion plasma machines become larger and more expensive to operate, and as temporal evolution of the plasma becomes important to the understanding of the physics of processes such as L-H transitions, edge-localized modes (ELMs), beta limits, ans disruptions, mul-

tipulse laser systems offer an attractive alternative to single pulse systems, both from the standpoint of the cost of repeating many discharges and sutdying events where shot-to-shot reproductibility is challenging [54].

The use of a multiple system eliminates the need to know a priori when the time of interest will occur during a plasma discharge and also permits measurements to be made during several different experiments in one shot, thereby increasing the productivity of the entire experimental program [54].

3.2.2 HRTS at JET

The High Resolution Thomson Scattering (HRTS) diagnostic is a 90° Thomson scattering system that measures electron temperature (T_e) and density (n_e) in JET along a chord across the low-field side of the plasma in octant 5, close to the horizontal mid-plane. When mapped to the magnetic mid-plane, the HRTS data typically runs from $R_{mid} = 3.0$ to 3.9 m. Currently HRTS provides 63 spatial data points per profile, with a 20 Hz repetition rate for the duration of a JET pulse. The system has a spatial resolution of ~ 1.6 cm in the core region and ~ 1 cm in the pedestal region. Note that during vertical kicks, the n_e profile may fluctuate with time due to optics misalignment. A scheme of the HRTS in JET is figured in 3.4

HRTS stands for High Resolution Thomson Scattering. The HRTS system on JET measures the density and temperature of the electrons in the fusion plasma via Thomson scattered laser light.

The HRTS system on JET fires 20 light pulses per second into the JET plasma from a Q-switched Nd:YAG LASER, housed in the 'roof-lab' above the JET machine. The laser light has a wavelength of 1064 nm (infra-red) and each 20 ns long pulse has 3 Joules of energy, which equates to about 150 million Watts per pulse.

The laser light interacts with the electrons in a plasma via a process called Thomson scattering: the electrons oscillate in the light's electric field and emit a photon of the same

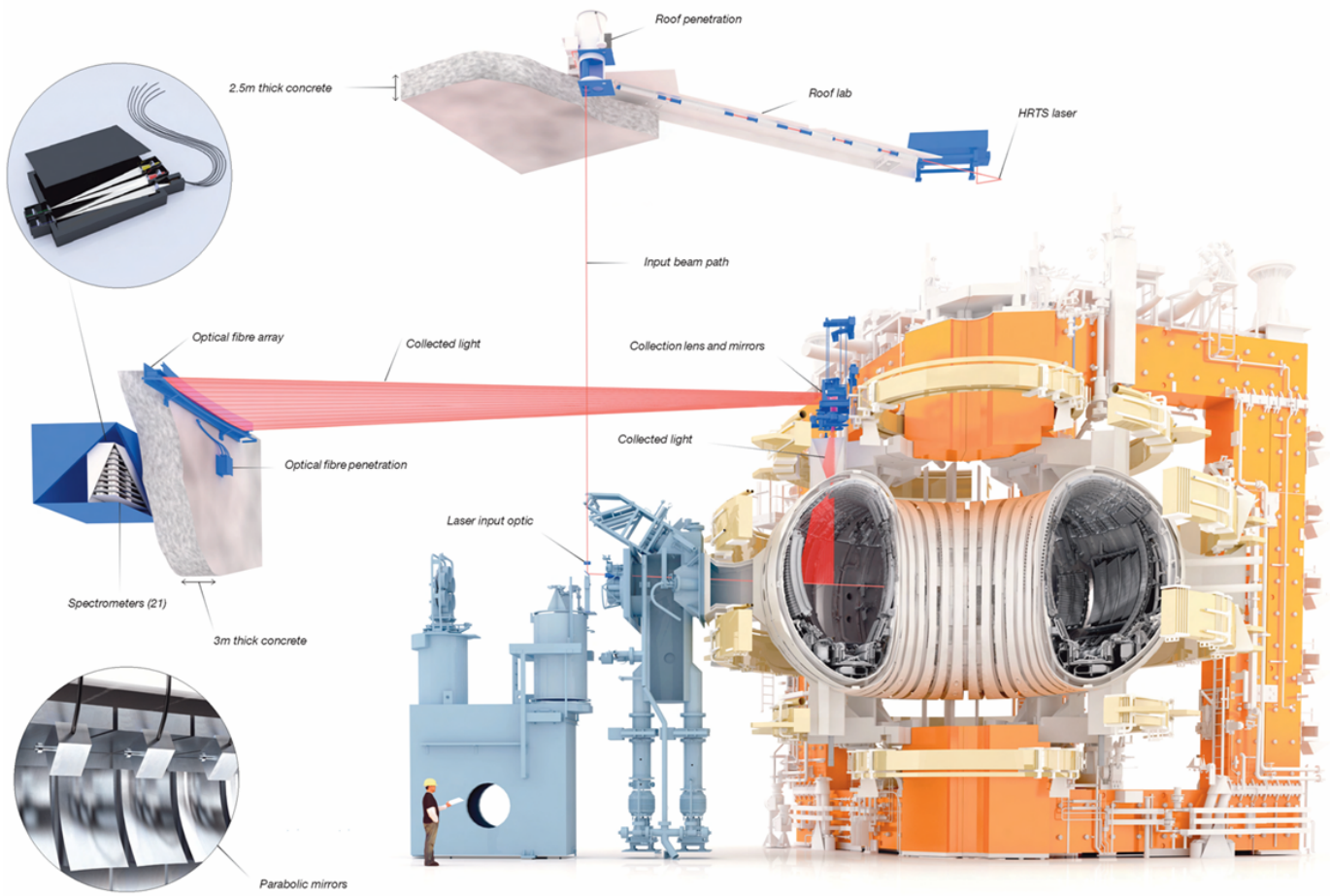

Figure 3.4: Neutral Beam scheme in JET

wavelength as the incident light. In a hot plasma, the thermal motion of the electrons broadens the laser spectrum via the Doppler effect.

The light scattered from each laser pulse is collected by a large lens at the top of the JET machine and is imaged with mirrors onto an array of > 120 optical fibres. Light in these fibres is sent to a bank of 21 polychromators, which use optical filters to 'chop' the received spectrum of light into four bands, or channels, each with it's own detector. The measured light gives information on:

1. Electron density; the total amount of scattered light is proportional to the number of electrons.

2. Electron temperature; the average speed (and hence temperature) of the electrons is

related to the width of the Thomson scattered spectra due to Doppler broadening of the laser line.

3. Spatial position; is given by the optical fibre position in the array. The spatial resolution of this system is $\sim$ 1 - 1.6 cm.

3.2.3 HRTS at TCV

The Thomson scattering system is the main diagnostic for the measurement of the spatial profiles of the electron temperature and density on TCV. The profiles are measured along a laser beam passing through plasma in vertical direction at R=0.9 m matching with mid radius of the TCV vessel. Wide-angle camera lenses, installed on 3 horizontal ports in sector 5, collect light produced by scattering. At present, there are 109 observation positions covering the region from Z=-69 cm to Z=+55 cm with a spatial integration length that depends on the channel location.

The scattered light is analyzed using filter polychromators conditioned with 4 or 5 spectral channels. The channels have been optimized to permit measurements of the electron temperature over a range from 6eV to 20keV. Not all polychromators allow to go down to 6eV.

The sampling rate of the measurements is determined by the repetition rate of the high-power Nd:YAG lasers, emiting at a wavelength of 1.06 microns.

There are 3 lasers combined in a cluster to build a beam which goes through the plasma. It appears as a single laser beam when viewed by the detection optics. Using a combination of 3 lasers offers the following options :

1. **Flexibility in timing**: Although each laser operates at a fixed repetition rate of 20Hz, individual triggering of the lasers at different delays permits to adapt the effective

sampling rates to the requirements of the measurements.

2. **Flexibility in effective pulse energy**: Measurements at low electron density require higher energies per laser pulse to conserve the signal-to-noise ratio. Concurrent triggering of 2 or 3 lasers can be used to amplify the effective laser pulse energy.

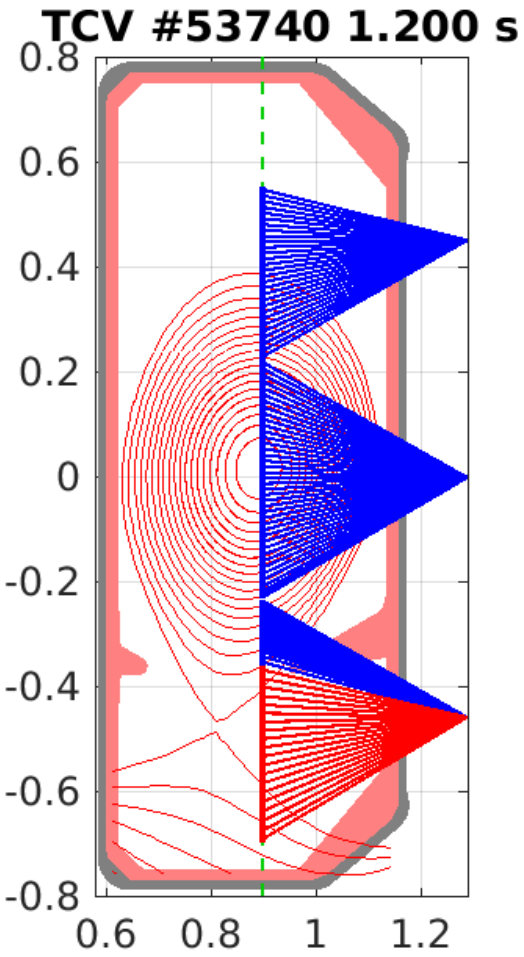

Figure 3.5: HRTS in TCV

For measurements of the electron density the system has to be absolutely gauged. Regular gauged are performed using Raman scattering from molecular nitrogen gas filled into the TCV vessel. Nevertheless, drifts in the relative alignment of the laser beams and the detection optics are going to affect the validity of the gauged. Therefore, the results from special

reference shots (standard shots, Yo-Yo shots) are used for verification.
In addition, a comparison of the line integrated density with the results from a multi-chord FIR interferometer is performed to derive a correction factor (FIR-THOM-RAT) and obtain consistency.

3.3 Gas puffing and divertor electric probes in JET

This section describes the JET torus layout, including the main wall structures, the gas injection modules (GIMs), and the key density measurements' locations (diagnostics). The wall materials are tungsten (W) and Beryllium (Be), corresponding to the divertor and main chamber wall, respectively.

The GIMs are the gas injection modules differentiated in spreading and intensity. The distribution of GIMs are,

- For the top gas puff (GIM7 or GIM8).
- For the divertor gas puff (GIM11).
- On the mid-plane GIMs (GIM3, GIM4, or GIM6).

The midplane GIMs are located very deep in the so-called A-port. As the gas is transported radially inward from the GIM, it keeps spreading poloidally and toroidally, filling the whole A-port essentially. A rather homogenous gas is found at the cross-section where the A-port is connected to the main chamber.

In steady-state JET H-mode plasmas, the divertor and main chamber wall's recycling fluxes behaves like particle sources, and limiters in the low field side have strong interactions with the plasma. They are essential during the confinement and generating recycling fluxes. The limiters are eight Wide Poloidal Limiters (WPLs), two ITER-Like-Antenna (ILA) limiters, and one Narrow Poloidal Limiter (NPL) having them different widths and different radial

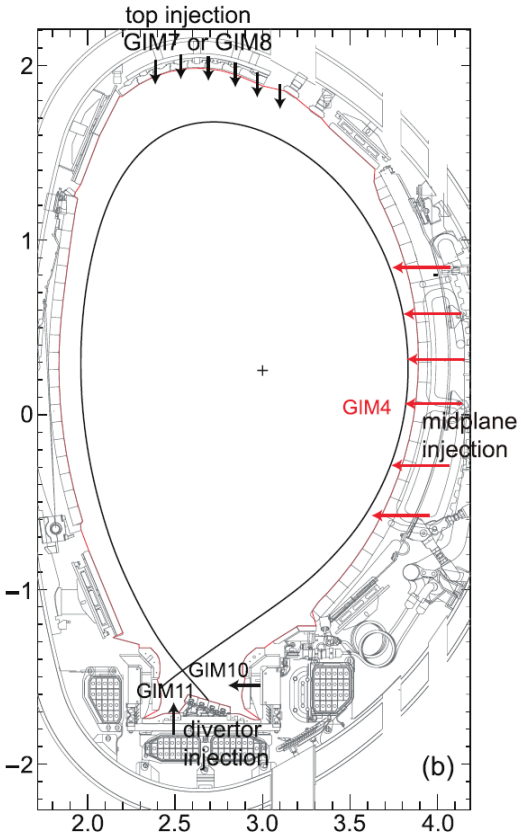

positions inducing toroidal inhomogeneities in the SOL. Divertor Langmuir probes (DLPs) provided target profiles of J_{sat}, n_e, and T_e measurements across divertor surfaces at 100 Hz, while J_{sat} was also available at 100 kHz. The Langmuir probes description is given in the following table and figures.

Table 3.3: Langmuir probes summary in JET

Probe	Tile	s(mm)	R(m)	Z(m)	A	B	C
1	1	270	2.391	-1.365	Dead	Working	Dead
2	1	303	2.410	-1.393	Working	Dead	Dead
3	1	362	2.415	-1.452	Dead	Dead	Dead
4	1	392	2.413	-1.482	Dead	Working	Dead
5	3	477	2.412	-1.561	Working	Working	Dead
6	3	496	2.417	-1.579	Working	Working	Working
7	3	518	2.423	-1.601	Working	Missing	Working
8	3	540	2.422	-1.623	Dead	Working	Missing
9	3	577	2.417	-1.660	Dead	Dead	Dead
10	4	813	2.412	-1.719	Dead	Dead	Dead
11	4	884	2.482	-1.707	Working	Working	Dead

12	5	1089	2.600	-1.605	Missing	Missing	Working
13	5	1116	2.626	-1.612	Working	Missing	Missing
14	5	1143	2.651	-1.621	Missing	Missing	Working
15	5	1165	2.672	-1.626	Working	Intermittent	Working
16	5	1182	2.689	-1.630	Working	Intermittent	Working
17	5	1202	2.706	-1.637	Working	Intermittent	Working
18	5	1215	2.719	-1.641	Dead	Dead	Working
19	5	1229	2.732	-1.644	Working	Intermittent	Working
20	5	1242	2.745	-1.648	Working	Working	Working
21	5	1264	2.765	-1.655	Intermittent	Dead	Dead
22	5	1278	2.778	-1.659	Dead	Working	Working
23	5	1291	2.791	-1.662	Dead	Working	Dead
24	5	1305	2.804	-1.666	Dead	Working	Working
25	6	1411	2.852	-1.708	Dead	Missing	Missing
26	6	1467	2.905	-1.721	Intermittent	Missing	Working
27	-	1510	2.980	-1.740	Missing	Missing	Missing
28	7	1684	2.889	-1.662	Working	Intermittent	Dead
29	7	1710	2.883	-1.637	Missing	Dead	Working
30	7	1724	2.879	-1.623	Working	Dead	Working
31	7	1742	2.878	-1.605	Working	Working	Dead
32	7	1783	2.885	-1.564	Dead	Working	Working
33	8	1878	2.884	-1.475	Dead	Working	Working
34	8	1813	2.884	-1.440	Working	Dead	Working
35	8	1953	2.895	-1.401	Working	Dead	Dead
36	8	1996	2.921	-1.367	Working	Dead	Dead

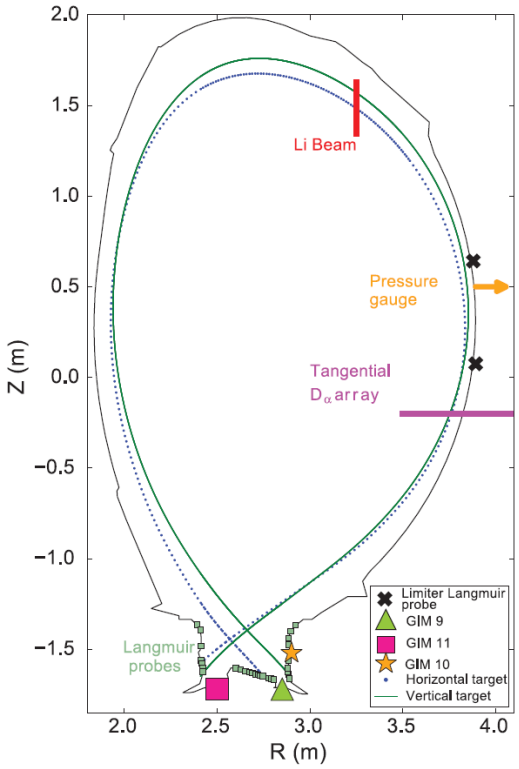
Li Beam
Pressure gauge
Tangential D_α array
Langmuir probes
Limiter Langmuir probe
GIM 9
GIM 11
GIM 10
Horizontal target
Vertical target
Z (m)
R (m)
2.0
1.5
1.0
0.5
0.0
−0.5
−1.0
−1.5
2.0
2.5
3.0
3.5
4.0

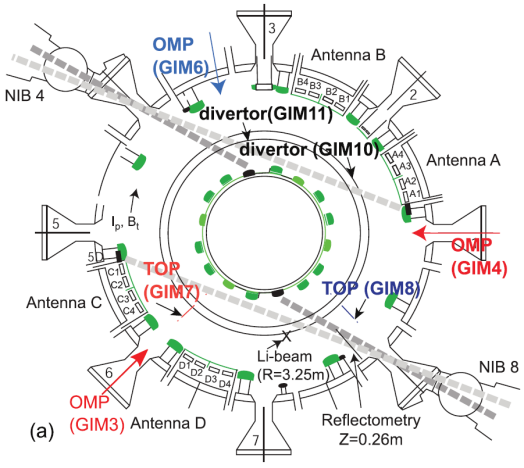
OMP (GIM6)
Antenna B
NIB 4
divertor(GIM11)
divertor (GIM10)
Antenna A
I_p, B_t
OMP (GIM4)
TOP (GIM7)
TOP (GIM8)
Antenna C
Li-beam (R=3.25m)
NIB 8
OMP (GIM3)
Antenna D
Reflectometry Z=0.26m
(a)
3
2
5
6
7

Chapter 4

Determination of the separatrix position

In this chapter, we show how to determine the separatrix position at outer mid-plane. This is important because in this region the density and temperature change rapidly due to the strong gradient of pedestal density-temperature presents in H-mode and consequently small changes in separatrix position imply strongs variations in plasma quantities.
The chapter is organized as follows: firstly we present the determination of separatrix positions based on power balance method [11, 13, 27, 55, 56]. As we will see this method relies on the expression of heat flux. Several expressions are presented and the estimation of the separatrix position obtained from the different expressions on a numerical simulation of a JET discharge using the SOLEDGE code is presented. From this analysis I made the choice for retaining the heat flux expression called kinetically corrected Spitzer [57, 13, 27, 56] one, which will be used as the standard one in chapter 5 for the determination of separatrix position in JET H-mode dataset.

4.1 Determination of the separatrix position at outer mid-plane using a power balance method

The power balance method provides an accurate separatrix position at the outer-midplane (OMP) for H-mode Thomson profiles [13, 15], n_e and T_e, because electron density profiles for the pedestal zone are stepper than in L-mode [58]. Then a slight shift of the separatrix

position regarding the pedestal amplitude upon the electron density profile is taken with more accuracy with power balance method than classical magnetic reconstruction method [12].

The hight-resolution Thomson scattering profiles at OMP are used calculating the electron parallel conducted heat flux profiles [13]. The parallel heat flux profile is integrated from wall up to the position where the computed power matches to the measured power input, $P_{SOL} = P_{Injected} - P_{rad,Bulk}$ [11, 13], where $P_{rad,Bulk}$ is calculated from an internal function of JET data acquisition system [59].

Harnessing the radial parallel conducted heat flux profile the power crossing the r-radial position is computed as follow [11]:

$$\begin{aligned} P|_{r\Rightarrow wall} &= \int_r^{wall} \frac{B_P}{B_T} q_{||}(r) r dr, \\ \text{with} \quad B_P &= \frac{\mu_0 I_P}{2\pi a \sqrt{(1+\kappa^2)/2}} \end{aligned} \tag{4.1}$$

with B_P and B_T as the poloidal and toroidal components of the magnetic field at OMP, the ratio B_P/B_T represents the angle of incidence of $q_{||}$ on the radial plane at OMP. Allowing for a cylindrical estimation of B_P, the expression for power crossing the r-radial position is updated to

$$P|_{r\Rightarrow wall} = \frac{\mu_0 I_P}{a B_{T,center} R_0 \sqrt{(1+\kappa^2)/2}} \int_r^{wall} r^2 q_{||}(r) dr, \tag{4.2}$$

with κ as elongation, a as minor radius, R_0 as major radius, and $B_{T,center}$ as toroidal magnetic field at the centre of plasma. When $P_{r\Rightarrow wall} = (1/4)P_{SOL} \Rightarrow r = r_{sep}$, the factor 1/4 [27, 13, 11] is consequence of uniformly entering of P_{SOL} from upstream to the targets represented by factor 1/2, and the split of heat flux over inboard and outboard targets represented by an extra factor 1/2.

4.1.1 Application to a JET discharge

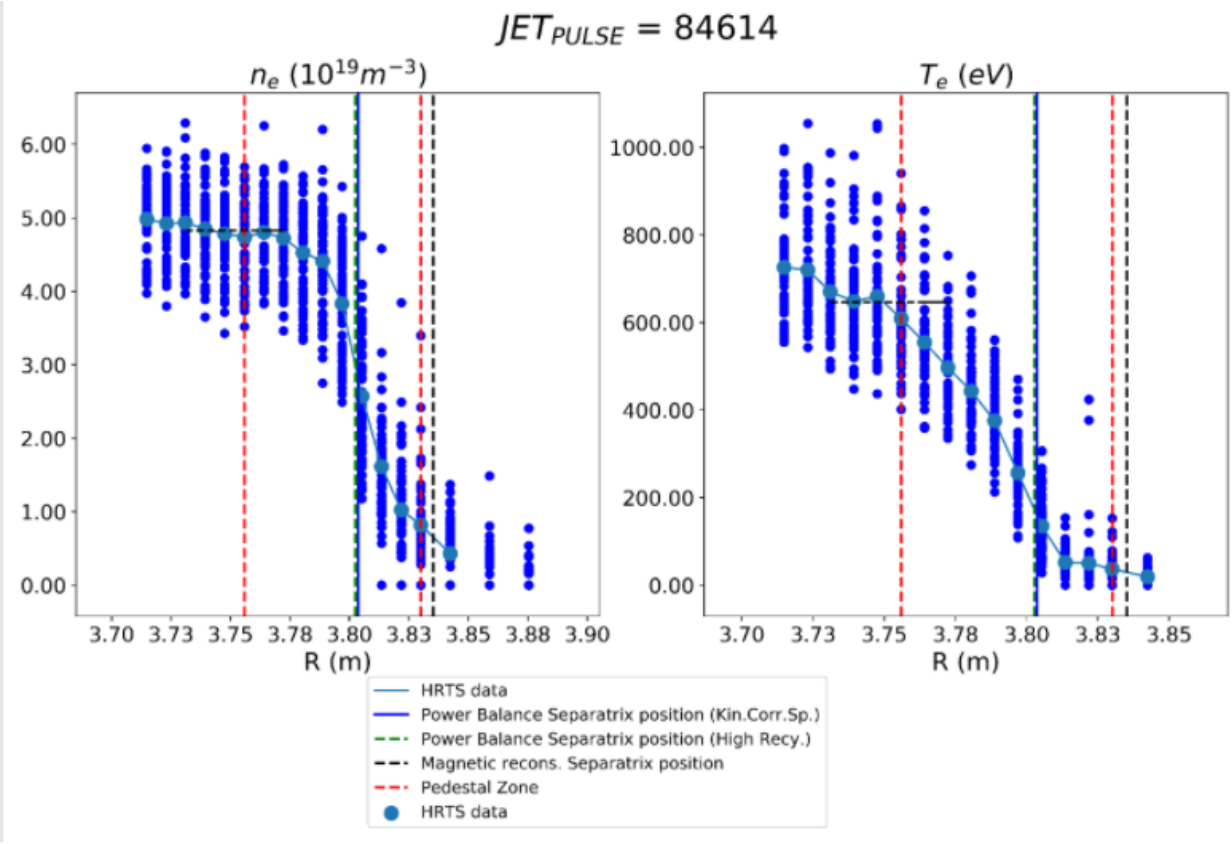

Figure 4.1: Electron temperature and density profiles for JET pulse number 89248.

The main analysis of this study is performed on electron outer mid-plane data collected by high-resolution Thomson scattering. The Thomson profiles are charted upon radial coordinate to use power balance in the separatrix determination. The electron profiles are shown in figure 4.1 for JET pulse number 89248, Thomson data has been represented as dark blue points, since power balance method in this study just use one profile the data is averaging regarding a time window normally between 2 and 4 s (40-90 Thomson profiles), this new profile is pictured with light blue points.

The steeped region on electron density profile provides us, by the gradient's analysis, the sector of radial axis where the separatrix is setted, thios region in figure 4.1 is enclosed by two dashed-red vertical lines.

The power balances method uses an expression for $q_{||}$ then separatrix position depends on

the $q_{||}$ expression. In [11] the expression chosen to $q_{||}$ is the kinetic-corrected Spitzer model, represented by blue vertical line, because it is the closest to magnetic reconstruction's separatrix used in SOLEDG2D modeling. Nevertheless the separatrix obtained using Spitzer-Harm expression to $q_{||}$, dashed-green vertical line in figure 4.1, does not have an excessive difference with the separatrix obtained by kinetic corrected Spitzer-Harm.

The kinetic-corrected Spitzer expression embody the completeness of heat flux since it gather the Spitzer conductivity, full-conducted representation of heat flux, with flux limited corrections. Also the magnitud of flux limit corrections depend of dataset's parameters.

4.1.2 Parallel heat flux expressions and verification on a SOLEDGE2D numerical simulation

A brief summary of parallel heat flux expressions is given:

- The Spitzer [60, 61, 62] model describes a high collisionality regime with a strong conduction behavior with the form $q_{||}^{Spitzer} = \kappa_{0e} T^{5/2} (dT/ds_{||})$ where κ_{0e} is the electron heat conduction coefficient. Considering $T_u \gg T_d$, high recycling condition, so $q_{||}^{Spitzer} \approx 2\kappa_{0e} T_e^{7/2}/7L_{||}$. In the dataset, $L_{||}$ is approximated like $L_{||} = \pi R q_{95}$.

$$q_{||}^{Spitzer} \approx 2\kappa_0 T_e^{7/2}/7L_{||}, \tag{4.3}$$

- On the sheath-limited [63, 64, 65] regime the difference between temperatures at upstream and downstream of the SOL is small. Due to the dependency $T_u = T_t \propto n_u^{-2/3}$, this regime is for low plasma density and considering Bohm boundary condition one obtains:

$$q_{||}^{sheath-limited} \approx \gamma (n_e/2) \sqrt{2eT_e/m_i} eT_e \tag{4.4}$$

- For flux-limited model [27, 10, 13, 57] an overestimation of electron heat fluxes in long mean-free regimes lead by the classical approximation for thermal conductivities, shown in laser-plasma experiments, is evident and in consequence a maximum allowable heat flux with the form, $q_{||}^{flux-limited} = \alpha v_{the} n_e e T_e$ are imposed, $v_{the} = \sqrt{eT_e/m_e}$, with $\alpha = 0.3$. Thus $q_{||}^{flux-limited}$ has a value lower than the thermal energy flux that is representative of long mean-free path regimes.

$$q_{||}^{flux-limited} \approx \alpha_e n_e \sqrt{eT_e/m_e} eT_e \tag{4.5}$$

- Finally the kinetically-corrected Spitzer [27, 10, 13, 57, 56] model condensed all the collisionality regimes in one expression, $q_{||}^{kin-corr-Spitzer} = q_{||}^{Spitzer} q_{||}^{flux-limited}/(q_{||}^{Spitzer} + q_{||}^{flux-limited})$.

We consider now two-SOLEDGE2D simulated pulses for two different input power referenced in the table 4.1. We will apply the power balance balance for determination of the separatrix positions using the four expressions presented above. The two simulation are in pure deuterium without drifts.The simulation indicated with $P_{INJECTED} = 8.4\,\mathrm{MW}$ refers to JPN 94210 where the particle flux from core is $1.5 \times 10^{21}\, m^{-2}s^{-1}$, gas puffing is $4.4 \times 10^{21} + 11.3 \times 10^{21}\,\mathrm{atoms}.s^{-1}$. We use autofit procedure to obtained mid-plane profile electron density and temperature equal to experimental ones. The original experimental data with $P_{INJECTED} = 8.4\,\mathrm{MW}$, particle flux from core $= 1.5 \times 10^{21} m^{-2}s^{-1}$, gas puffing $= 4.4 \times 10^{21} + 11.3 \times 10^{21}\,\mathrm{atoms}.s^{-1}$. We have applied the power balance method for

PULSE	**Pin**	**Tsep**	**Tsep(S2D)**	**nsep**	**nsep(S2D)**
94210-1040	8.4 MW	78 eV	92 eV	$1.24 \times 10^{19} m^{-3}$	$1.33 \times 10^{19} m^{-3}$
94210-1060	4 MW	61 eV	63 eV	$1.18 \times 10^{19} m^{-3}$	$1.19 \times 10^{19} m^{-3}$

Table 4.1: Comparison between the electron temperature and density at the separatrix position estimated with the power balance method using the kinetically-corrected heat flux expression and the separatrix position given by soledge meshgrid, indicated with (S2D).

determining the radial position of the separatrix at the outer mid-plane considering four different expressions for heat flux. The results are presented in figures 4.4 and 4.5.

As we can see in figures 4.4 and 4.5, the separatrix position brought by the Kinetic-corrected model is the closest one to the separatrix position fixed in the mesh grid for SOLEDGE2D simulation. For this reason, in the next chapter, the determination of the separatrix position at outer mid-plane in JET H-mode data is under the use of the Kinetic-corrected model for the heat flux.

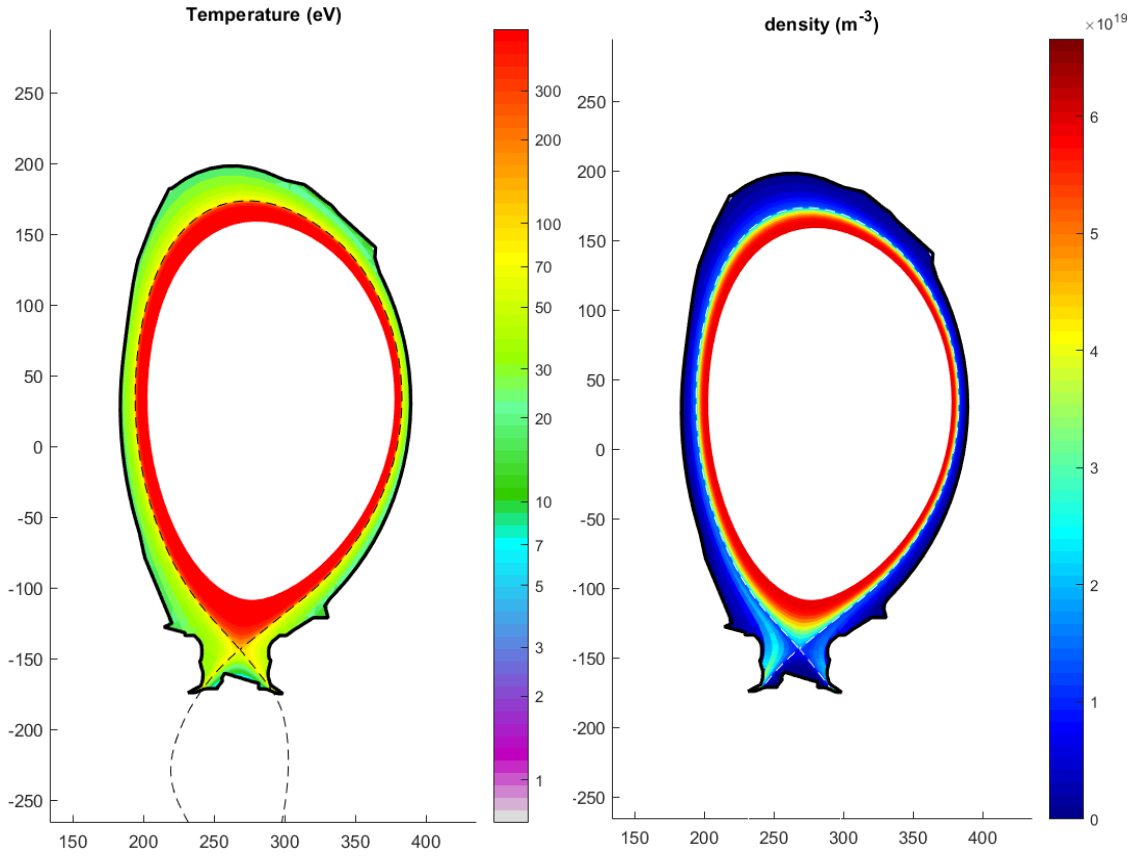

Figure 4.2: Electron temperature (left panel) and density (right panel) poloidal profiles computed with SOLEDGE2D simulations for JPN94210-1040. The separatrix is indicated with dotted black curve

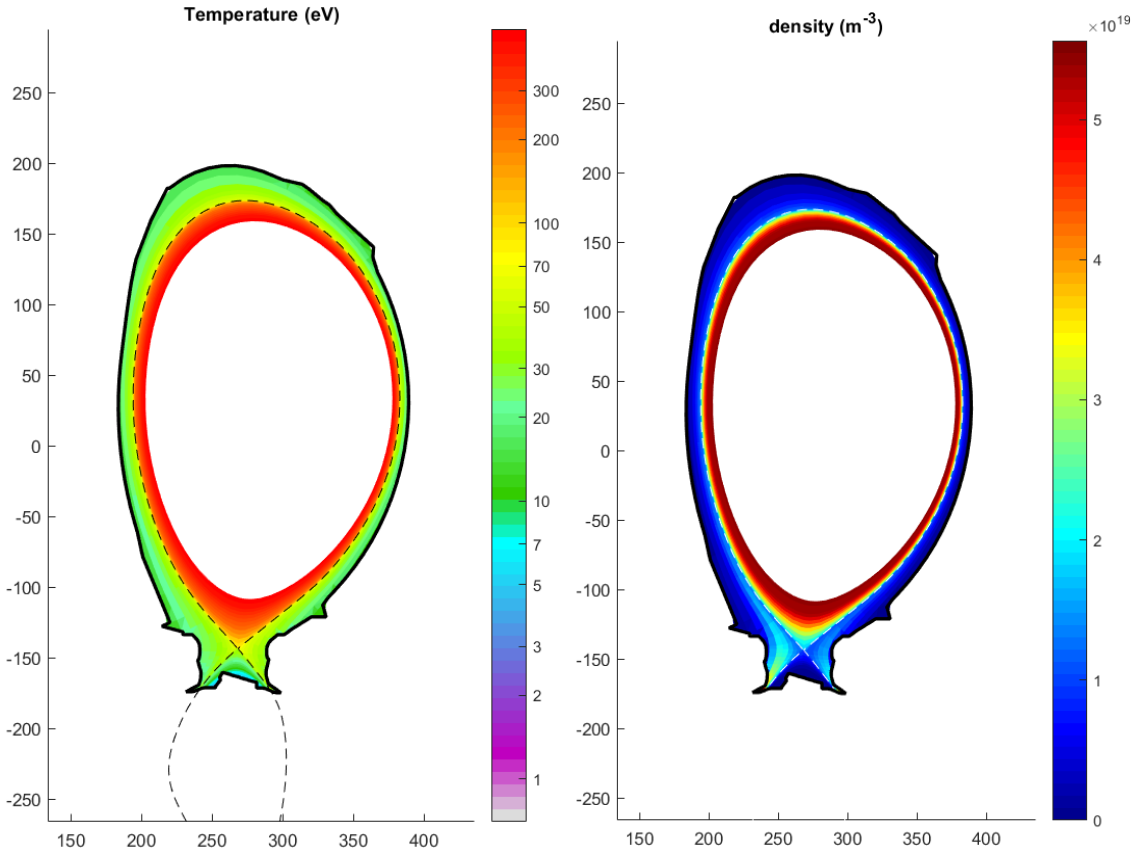

Figure 4.3: Electron temperature (left panel) and density (right panel) poloidal profiles computed with SOLEDGE2D simulations for JPN94210-1060. The separatrix is indicated with dotted black curve

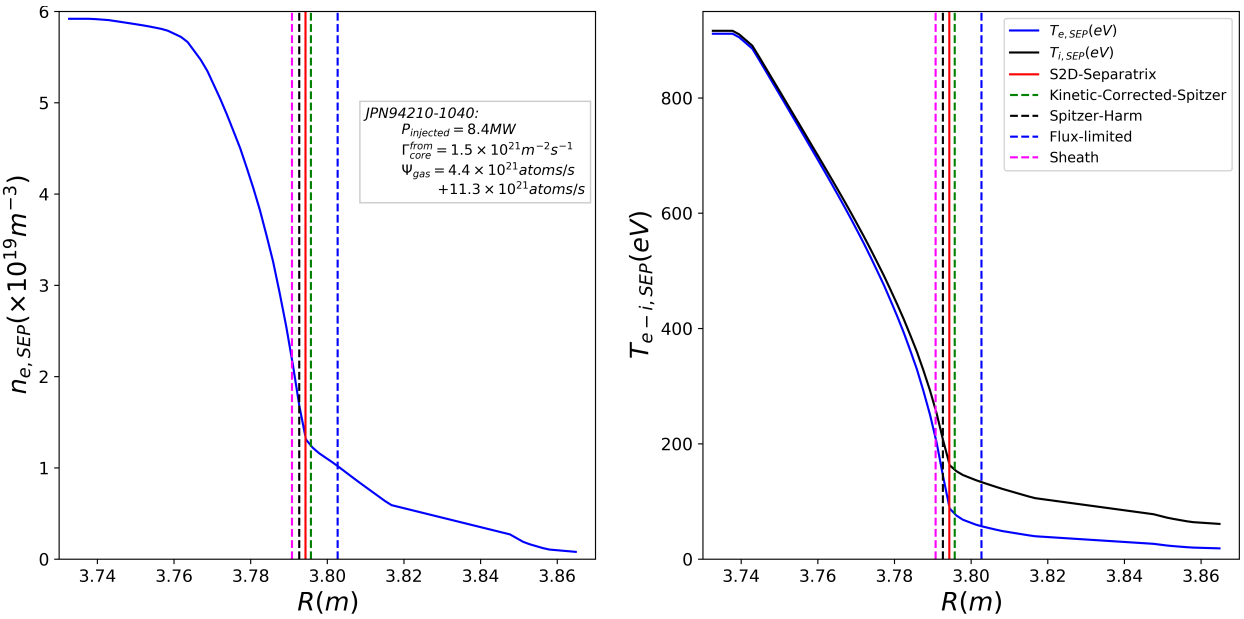

Figure 4.4: Separatrix positions given by the different heat flux models on electron temperature and density profile for JET pulse number 94210 with conditions of modeling 1040.

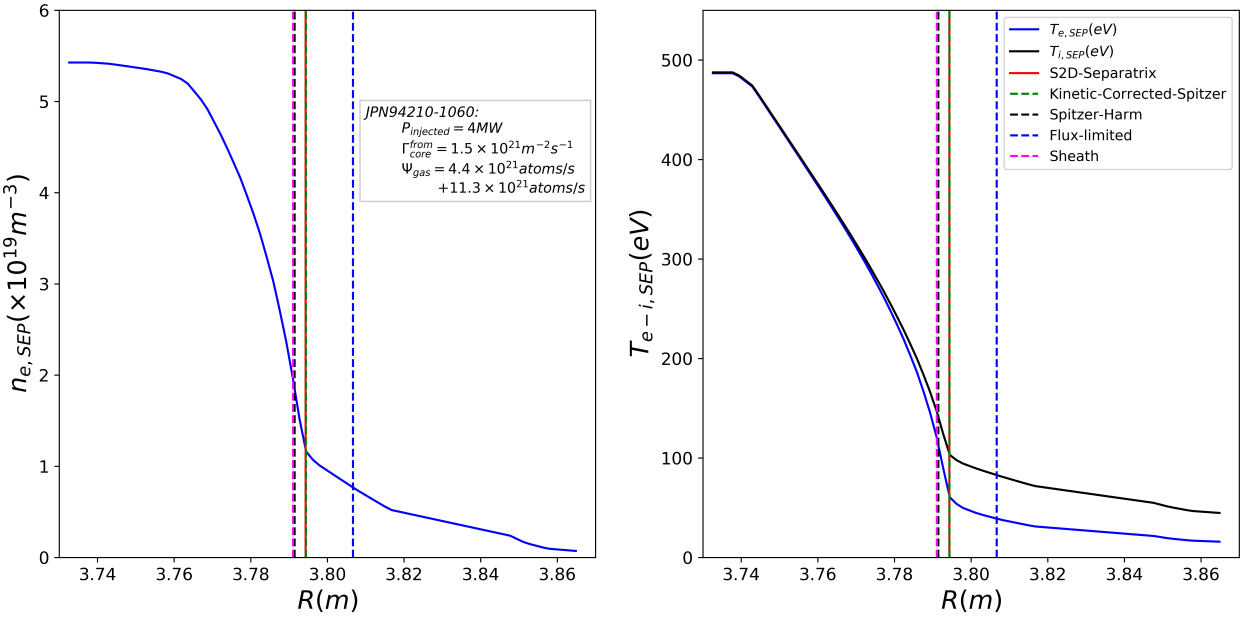

Figure 4.5: Separatrix positions given by the different heat flux models on electron temperature and density profile for JET pulse number 94210 with conditions of modeling 1060.

Chapter 5

Investigation of the dependency of midplane separatrix density in H-mode as a function of engineering parameters for JET tokamak

A viable magnetic fusion reactor has to combine very high plasma density and temperature in the core region, in order to maximize fusion reactions, with plasma conditions in the divertor region compatible with long life expectancy of plasma-facing components, i.e. plasma heat flux under 10 MW/m^2 in steady-state conditions and very low plasma temperatures. This chapter investigates JET H-mode discharges looking for optimized scenario combining the density at the top pedestal location $n_{e,PED}$ and the density at the separatrix position $n_{e,SEP}$ in a ratio $n_{e,SEP}/n_{e,PED}$, and expressing this ratio as a function of engineering parameters. Indeed, on one side pedestal density is an important indicator of the quality of H-mode confinement, it sets boundary condition of the core plasma, and a high confinement regime is expected to be achieved with an optimal $n_{e,PED}$. On side of separatrix density it is a crucial factor for divertor regime and in particular for the onset of divertor detachment. The ratio $n_{e,SEP}/n_{e,PED}$ comprises both the core plasma conditions and the divertor physics. In this work we have analyzed ninety JET discharges in the H-mode regime to determine a tentative scaling law of the ratio $n_{e,SEP}/n_{e,PED}$ as a function of two engineering parameters, the plasma current I_P and the total injected power P_{TOTAL}.

In the following section, we present first the main parameters of the discharges we have considered for our analysis. Then we will focus on the determination of the scaling law.

5.1 JET dataset

The dataset of JET presented in this thesis was gathered from different campaigns and experiments, that were not tailored for the determination of the $n_{e,SEP}/n_{e,PED}$ relationship we are searching for. Even if we tried to cover the largest range of engineering parameters we could, analysing the dataset we have found preferred configurations used in JET discharges, inducing dependencies between a given number of such enginnering parameters. A first analysis of the enginnering parameters covered by the dataset is presented in fig. 5.1. On the left panel is presented the dataset in terms of the toroidal magnetic field B_t and the plasma current I_p values for the considered discharges. The datapoints shows that for a large part of the dataset a linear relationship between these two parameters holds, and for this reason in the scaling law we will present in the following only one of the two will be considered. Still in fig. 5.1, right panel, the dataset is reported in terms of total injected power P_{total} and plasma current I_p, showing that in this case one has a quite good scan over the discharges allowing to consider both parameters in the scaling law. As a first analysis of the dataset in terms of these two parameters, we show in figure 5.2 the behavior of the top pedestal density $n_{e,PED}$ in function of I_P (left panel) and in function of P_{TOTAL} (right panel). We obeserve on one side that the pedestal density can reach quite high values at the increase of I_P,as expected, and it will be interesting in the following look at the ratio between the separatrix and pedestal densities in these cases. On the other side, the increase of the total injected power corresponds with an increase of the pedestal density. These first results will help in the interpretation of the plasma behaviour we will present in the following, when we will analyse in particular the temperature and density at the outer midplane separatrix. We continue in the analysis of the dataset looking at the relationship between density at the outer midplane separatrix with top pedestal density.

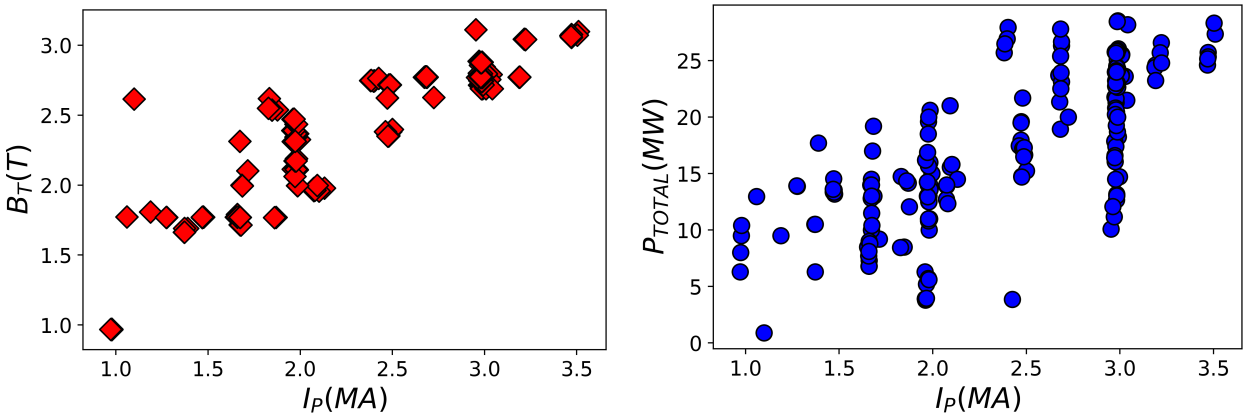

Figure 5.1: Left panel: dataset plotted in the $I_P\,(MA)$ - $B_T\,(T)$ plane. One can observe that in the largest part of the discharges the liner relationship between B_T and I_p, indicating an "operational preference" over the dataset. Right panel: dataset plotted in the $I_P\,(MA)$ - $P_{TOTAL}\,(MW)$ plane indicating that the plane is well covered with the and allowing for using these two enginnering parameters in the scaling law

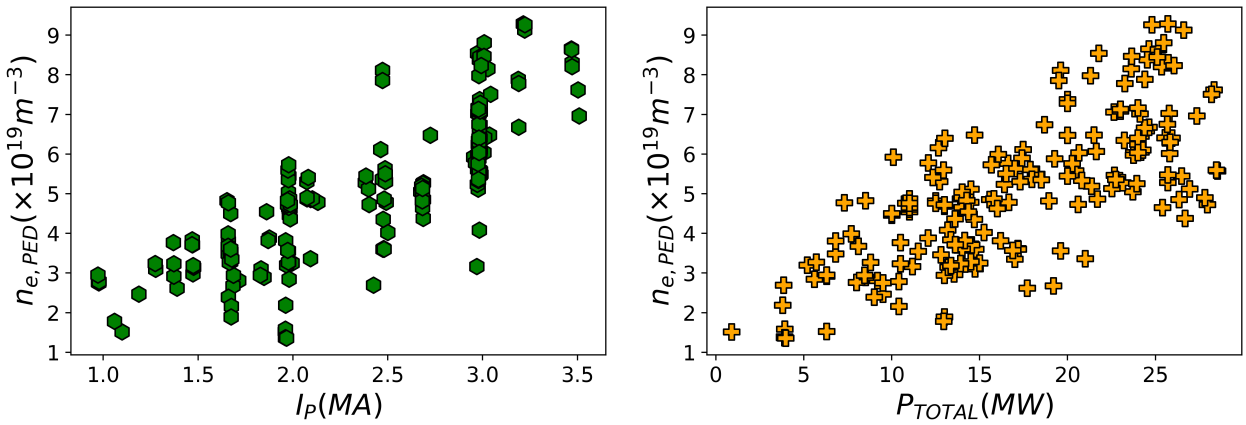

Figure 5.2: (Left panel: Plot of the dataset in terms of top pedestal density $n_{e,PED}$ as a function of I_P, displaying an impact of I_P on the quality of confinement. Right panel: Plot of the dataset in terms of $n_{e,PED}$ as a function of the total injected power P_{TOTAL}, showing an overall liner relationship between these two quantities

The total JET dataset in H-mode fairs a linear increasing of electron separatrix density as shown in figure 5.3 and a remarkable electron temperature around of $140eV$, averaged $T_{e,SEP}$, as shown in figure 5.4, those results are shown in contrast with pedestal density. The ratio of densities, $n_{e,SEP}/n_{e,PED}$ looks enclosed among two limits with a minimum of 30% and a maximum 80% as shown figure 5.3. Concerning the eletron temperature at the separatrix outer midplane, we observe similar behaviours when plotted as a function of

top pedestal or separatrix density. The data points are quite scattered around the average value of $140eV$, as shown in figure 5.5. The range of variation for $n_{e,SEP}$ is smaller than the range of $n_{e,PED}$ holding a scattering behavior of $T_{e,SEP}$ even for high values of $n_{e,SEP}$ in contrast to $n_{e,PED}$ for which the $T_{e,SEP}$ shows a less scattered behavior at the increase of $n_{e,PED}$ values, in particular for $n_{e,PED} \gtrsim 6.5 \times 10^{19}\mathrm{m}^{-3}$. The enclosure of separatrix

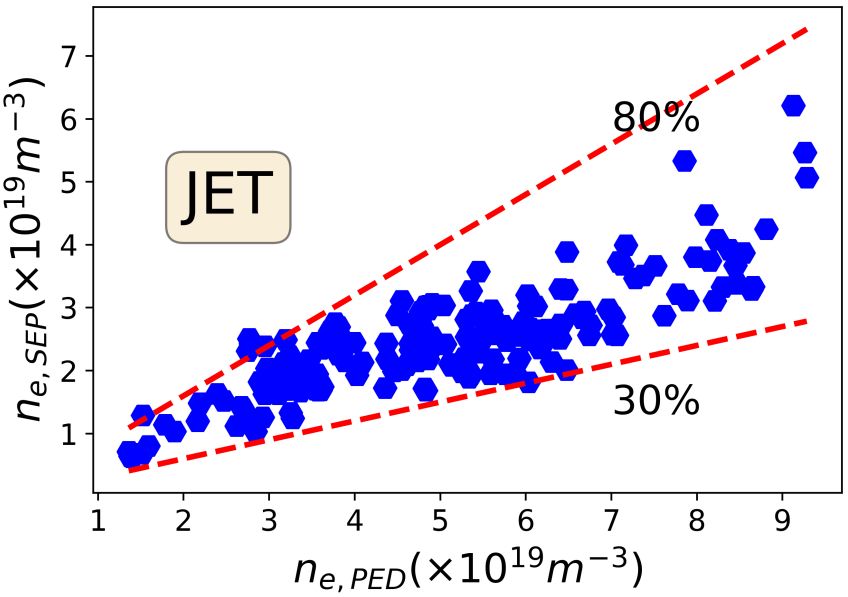

Figure 5.3: JET dataset under consideration plotted in terms of electron separatrix density as a function of pedestal density. The dataset is enclosed by two limits set like $30\% \leq n_{e,SEP} \leq 80\%$.

density dataset as shown in figure 5.3 supports the density limit concept, that restricts the operation of H-mode. A similar enclosing trend for pulses in H-mode was also published in [27] with limits for $n_{e,SEP}/n_{e,PED}$ given by $\leq 30\%$ and $\geq 60\%$, and coherent with the current results. The limits of $n_{e,SEP}/n_{e,PED}$ and the trend of datapulses for being close to lower or higher limits shown in figure 5.3 might be correlated to engineering parameters influence. Nevertheless that the values ranges of them are wide, allow the results like figure 5.3 consider all the possible influences that is caused by engineering parameters, from tiny to huge values. Being considered wide ranges of engineering parameters on this dataset, the results can be extrapolated to another tokamak datasets. Moreover, as already mentioned, these current

results might be sensitive to an artificial relation settled by operation requirements like evidenced in the left-figure 5.1. For this reason we used only one parameter between I_P and B_T, but this restriction is related just to the present dataset and could be removed in future and more complete dataset. On the side of electron separatrix temperature, $T_{e,SEP}$,

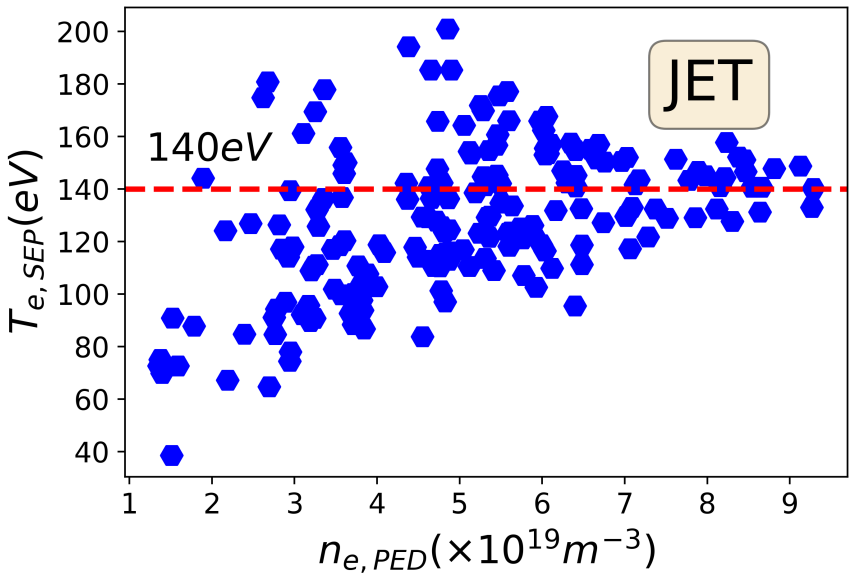

Figure 5.4: JET dataset under consideration plotted in terms of electron separatrix temperature as a function of pedestal density. In the figure is pointed out in red dashed line the averaged electron separatrix temperature, $140\,eV$

its behaviour as a function of electron separatrix and pedestal densities displays similar trends. The temperature, as shown in figure 5.4, looks like scattered, with high levels of it, for low values of $n_{e,PED}$ while that for higher values of $n_{e,PED}$ the scattering of $T_{e,SEP}$ decreases. The same is qualitatively observed plotting $T_{e,SEP}$ as a function of the outer midplane separatrix density $n_{e,SEP}$.

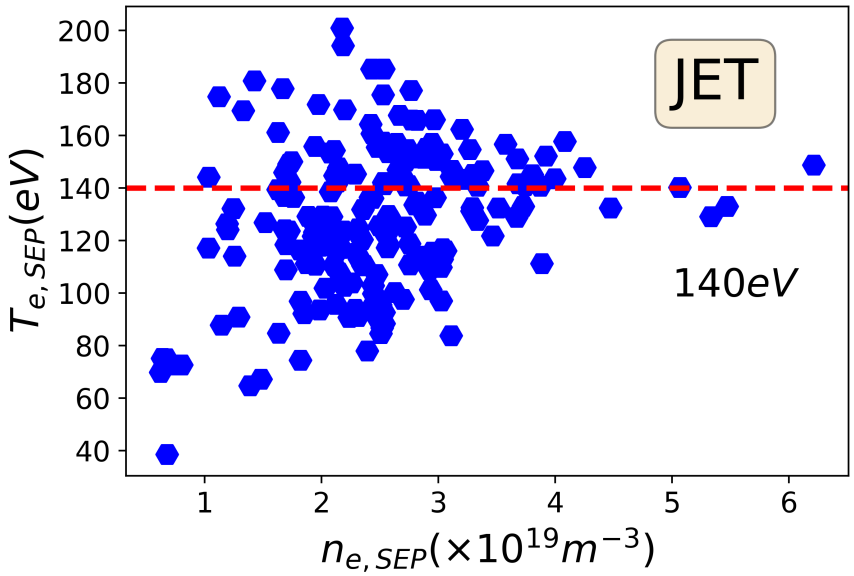

Figure 5.5: JET dataset under consideration plotted in terms of electron separatrix temperature as a function of separatrix density. The range of $T_{e,SEP}$ is reduced for $n_{e,SEP} \geq 3.0 \times 10^{19}\mathrm{m}^{-3}$.

5.2 Determination of a scaling law

After this first analysis I derive a scaling law of the dependence of the separatrix outer midplane density $n_{e,SEP}$ as a function of the top pedestal density $n_{e,PED}$, the total injected power P_{TOTAL} and the plasma current I_P.

$$n_{e,SEP} = C \times n_{e,PED} P_{TOT}^{0.06} I_P^{-0.58} \propto \frac{n_{e,PED}}{\sqrt{I_P}} \tag{5.1}$$

The current scaling law relates the densities of separatrix and pedestal at outer midplane with two engineering parameters bringing an inverse relation of $n_{e,SEP}/n_{e,PED}$ with I_P that was previously deduced using the experimental results represented in figures 5.1 and 5.2 then the scaling law saves coherence with the general trend of the dataset. On side of P_{TOTAL} the dependence is faint and direct, but in the next analysis show that even the faint dependence of P_{TOTAL} supports a notorious trend of increasing $n_{e,SEP}$ by consequence P_{TOTAL}.

The scaling law is presented in figure 5.26 where the values of the separatrix density determined from the scalin law for each discharge in the dataset are plotted against the experimental values obtained using the power balance method for the determination of the separatrix position. There are values for, $n_{e,SEP}(\text{DATA}) \geq 5 \times 10^{19}\text{m}^{-3}$, out of trend that can be affected to unconsidered parameters. In the following we will continue the analysis of the dataset in order to find such parameters.

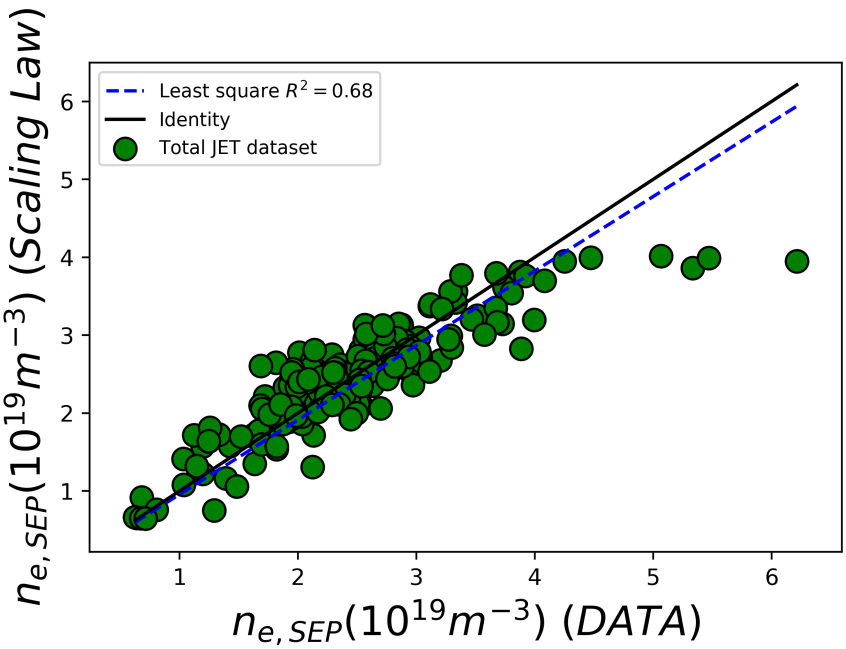

Figure 5.6: Comparison of experimental $n_{e,SEP}$ (determined using power balance method), and $n_{e,SEP}$ provided by the scaling law referenced in equation 5.1. There are values for, $n_{e,SEP}(\text{DATA}) \geq 5 \times 10^{19}\text{m}^{-3}$, out of trend that can be affected to unconsidered parameters.

5.2.1 Further investigation of dataset and dependencies from engineering and plasma parameters

The general dataset of JET H-mode discharges under consideration shows a linear relation between I_P and B_T, as shown in previous section, see figure 5.1. For studying the dependency between $n_{e,SEP}$ versus an engineering parameter like P_{SOL}, the others parameters should be fixed and to choose the reduced intervals for I_P and P_{SOL}. Then we identify two subsets where the variations of I_P and B_T are minimum as shown in figure 5.7. The range of values for I_P and B_T corresponding to subset 1 and subset 2, pointed out in figures 5.7, are exposed in table 5.1.

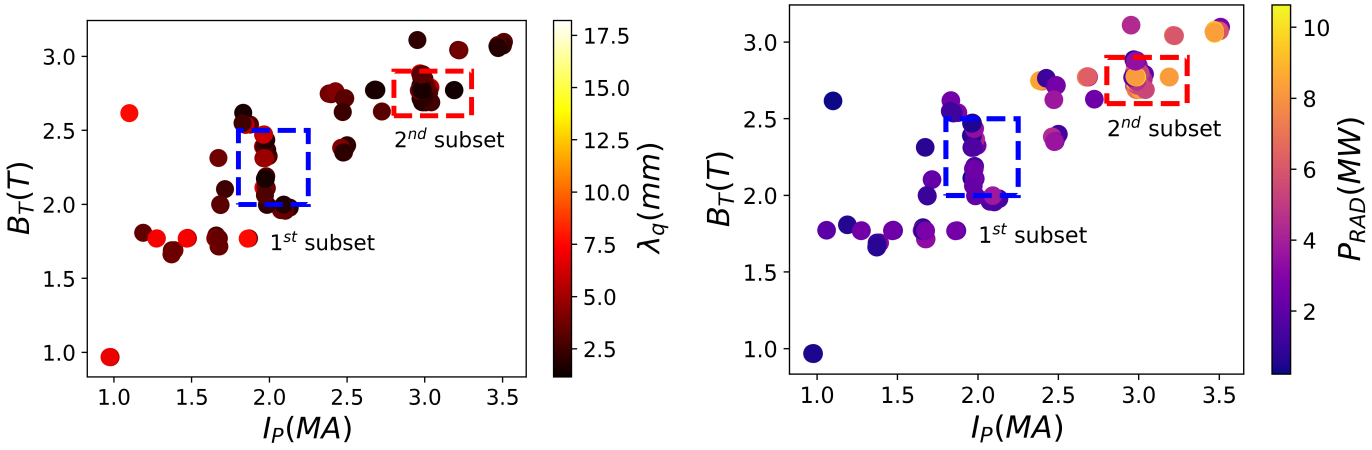

Figure 5.7: The framework of I_P versus B_T is used like background to colored the data as function of λ_q and P_{RAD}, thus homogeneous subsets can be identified like those pointed out as 1st subset and 2nd subset. These two subsets can be employed to observe the evolution of magnitud like $n_{e,SEP}$, e.g., as function of unconsidered parameter like P_{TOTAL}.

	I_P (MA)	B_T (T)	P_{RAD} (MW)	λ_q (mm)
1er subset	$(1.8, 2.25)$	$(2.0, 2.5)$	$(0.2, 4.6)$	$(1.5, 4.8)$
2nd subset	$(2.8, 3.3)$	$(2.6, 2.9)$	$(0.6, 10.6)$	$(1.2, 5.9)$

Table 5.1: Averaged values for the two-point model comparison in C-C configuration.

Besides the new intervals for subset 1 are plotted in figure 5.9 bearing out a bigger variation of B_T compared to I_P, conceding us the opportunity to split the range of B_T in two new

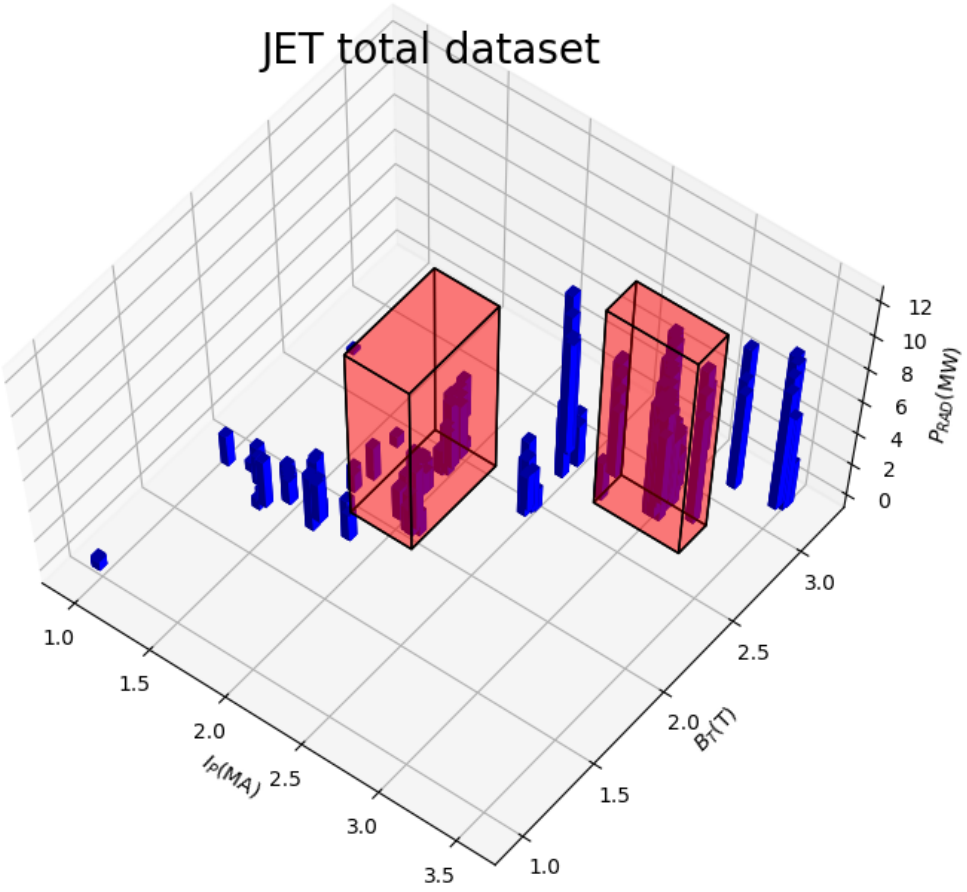

Figure 5.8: The framework of I_P versus B_T with a 3D perspective.

sets where the data are more condensed, remaining the variation for P_{SOL} as indicate the colored of figure 5.9. The results for the subset 1 are illustrated in figures 5.10 and 5.10,

	I_P (MA)	B_T (T)	P_{RAD} (MW)
$I_B^{(1)}$	$(1.96, 1.98)$	$(2.06, 2.18)$	$(0.2, 3.2)$
$I_B^{(2)}$	$(1.95, 1.99)$	$(2.31, 2.47)$	$(0.3, 4.6)$

Table 5.2: Averaged values for the two-point model comparison in C-C configuration.

based on the reduced new intervals for I_P and B_T these pictures show the evolution of $n_{e,SEP}$ in function of P_{SOL}, upholding a $n_{e,SEP}$ increase with an increasing of P_{SOL}. Nevertheless, for the current general JET dataset the variations and trends of $T_{e,SEP}$ are meaningless for the moment because even when the colored, P_{SOL} label, point out a tentative increasing of $T_{e,SEP}$ while P_{SOL} increase, the data display a high scattering degree, allowing us to plan a

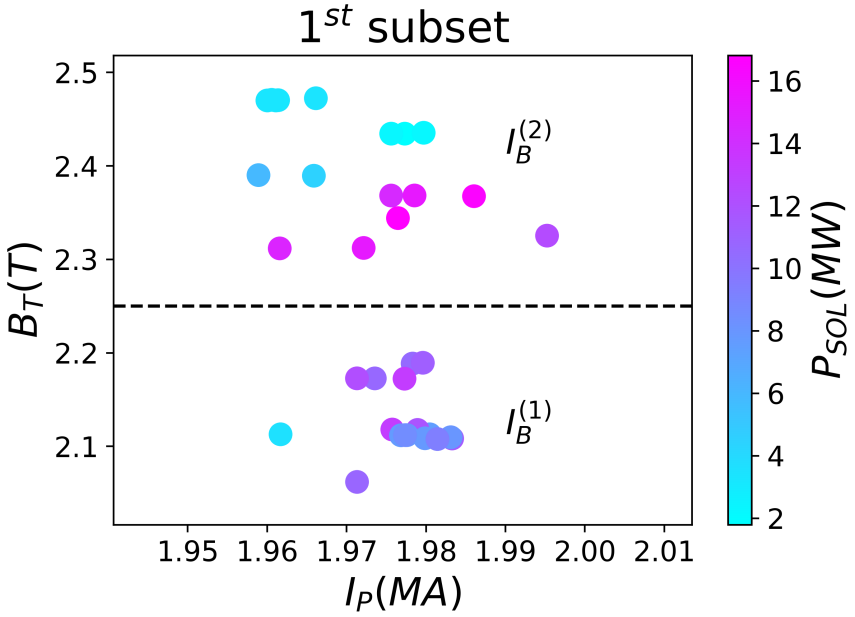

Figure 5.9: This is a representation of one subset $I_P - B_T$ with small variations for B_T and I_P. The coloring of P_{SOL} allows to split this subset in two new sets where the range of P_{SOL} is wide.

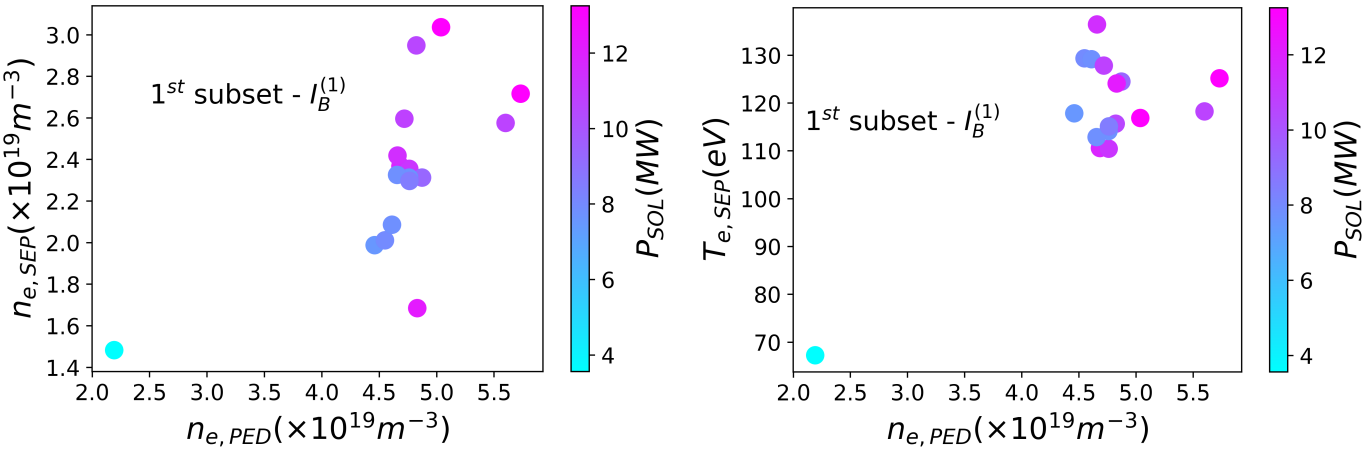

Figure 5.10: These two graphics show an increasing of $n_{e,SEP}$ while P_{SOL} increases and show small variations of $T_{e,SEP}$ respect to P_{SOL}.

hypothesis where the $T_{e,SEP}$ is assumed being sensible for another parameter or features of discharges that are explored in the next sections of this chapter.

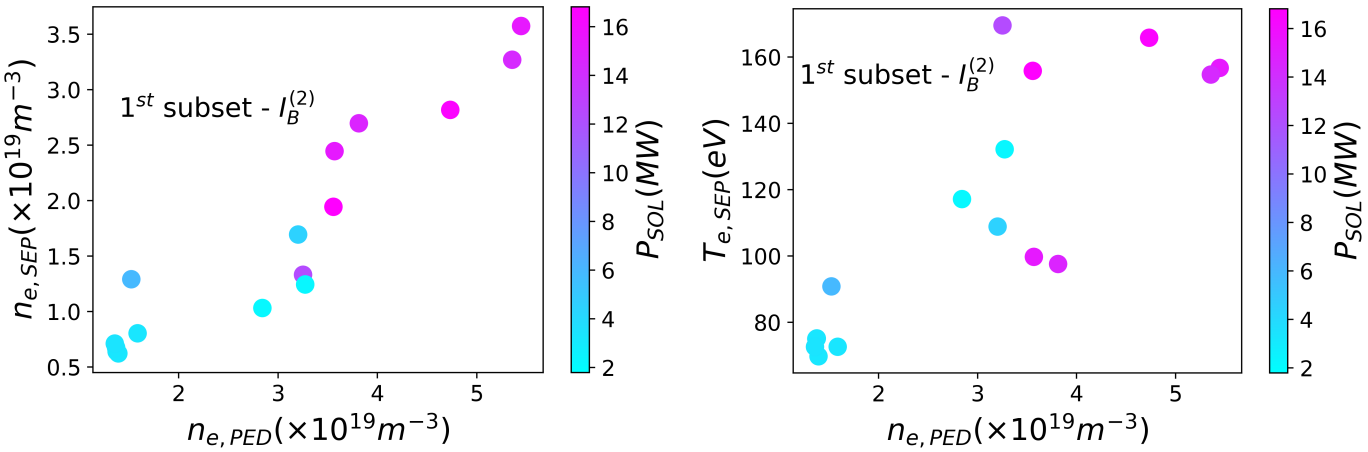

Figure 5.11: These two graphics evidence that $n_{e,SEP}$ and $T_{e,SEP}$ increase while P_{SOL} is incresing. There are $T_{e,SEP}$ values, $\geq 100\,eV$ and $\leq 140\,eV$, for which P_{SOL} takes low and high values.

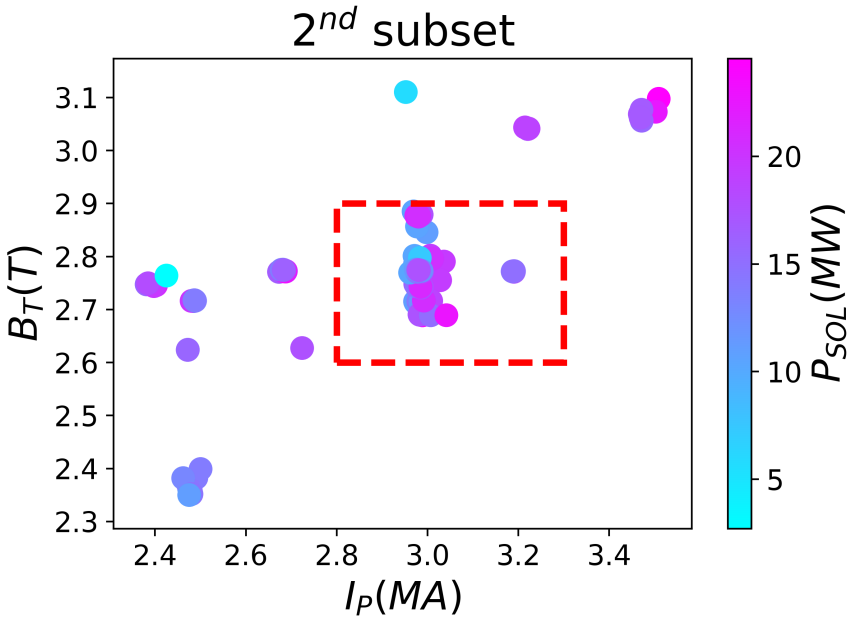

Figure 5.12: This is a representation of a subset where I_P and B_T have been reduced in their ranges keeping a wide range of P_{SOL}.

This second analysis is based for the second subset, referenced in 5.13, with the reduced intervals for B_T and I_P pointed out in table 5.2 where the range for P_{SOL} is broad as is shown in figure 5.12. This subset attests an increasing of $n_{e,SEP}$ while P_{SOL} increase. On the side of $T_{e,SEP}$, an increase of P_{SOL} correlates with an increasing of $T_{e,SEP}$, and for the interval of $n_{e,PED}$, $\left[5.5, 9.0\right](\times 10^{19} m^{-3})$, a slowly decreasing of temperature $T_{e,SEP}$ is pointed out while $n_{e,PED}$ increases.

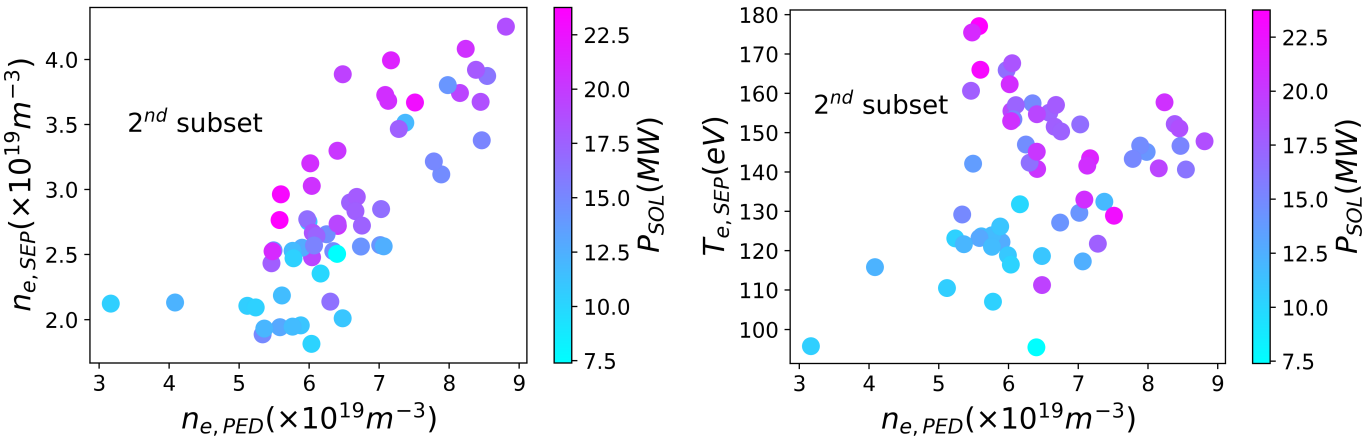

Figure 5.13: These two graphics show an increasing $n_{e,SEP}$ and $T_{e,SEP}$ while P_{SOL} has increased holding a wide range of P_{SOL}.

5.3 JET dataset analysis with respect to divertor magnetic configuration

The magnetic divertor configurations selected for this study are Corner-Corner, Vertical-Horizontal and Vertical-Vertical as shown in figure 5.14. There are 36 Langmuir-probes arrange on the divertor zone as shown in figure 5.14 collecting current-voltage raw data enabling us calculate electron divertor temperature and density. Likewise, there is a high-resolution Thomson scattering (HRTS) system collecting pre-processed data of electron temperature and density. Since HRTS system has a horizontal alignment the profiles of electron temperature and density are projected on radial profile, this diagnostic system is located closed to outer mid-plane position like is shown in figure 5.14. This location favors the resolution of magnitudes because of the properties of outer mid-plane respect the heat flux coming to core, this system has an horizontal orientation and it is upon the outer face of the tokamak.

The change among magnetic configurations has a geometrical impact on the divertor physics considering the striking points and width of SOL like two major factors. The change of SOL width has an impact on the intensity of heat flux and the wetted area on the target, while the position of the striking points determine the location of impurity sources and neutrals, with diverse impacts on operation of plasma. It is known that the quality of H-mode in experiment seems correlated to the divertor magnetic configuration. Many reasons could explain that, but instead of trying to have a detailed analysis of each single physical mechanism at play, we continue with our approach, adding a label referred to magnetic configuration for each H-mode discharge and analysing the trends with respect engineering parameters as already introduced in the chapter.

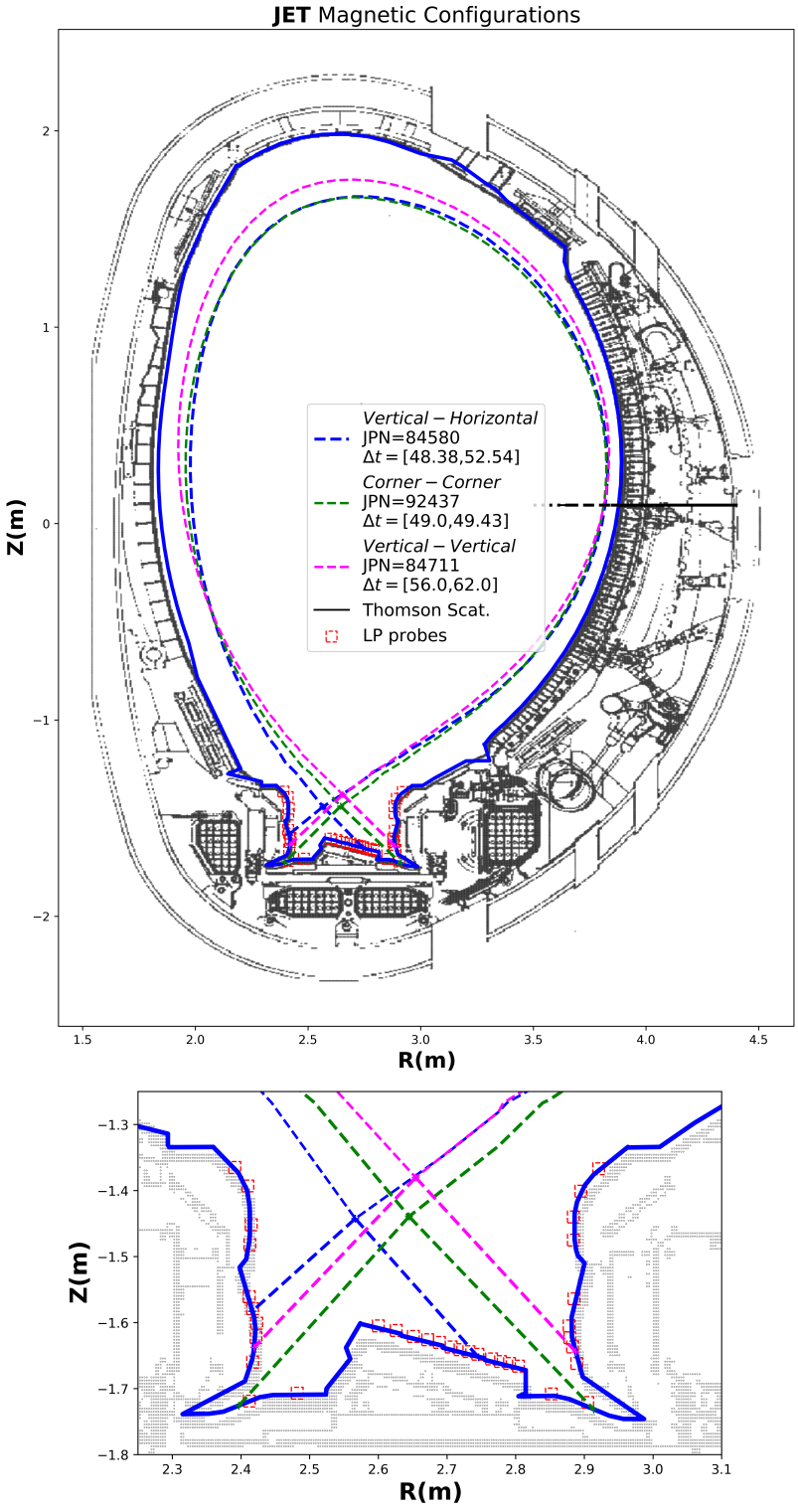

Figure 5.14: Poloidal section of JET. The Corner-corner (C-C), Vertical-Horizontal (VT-5) and vertical-vertical magnetic configurations are represented with green, blue and pink dashed lines respectively, referring to three particular discharges as mentioned in the inset of the figure. Horizontal black line crossing bidimensional wall profile (blue solid line) represents midplane Thomson scattering diagnostic; red squares in the divertor region represent Langmuir probes.

5.3.1 Analysis of plasma discharges in Corner-Corner divertor magnetic configuration

As we have already seen, the ensemble of H-mode JET discharges we consider exhibits general trends in function of engineering parameters. We now look at such trends with respect to discharges with the same divertor magnetic configuration. For Corner-Corner

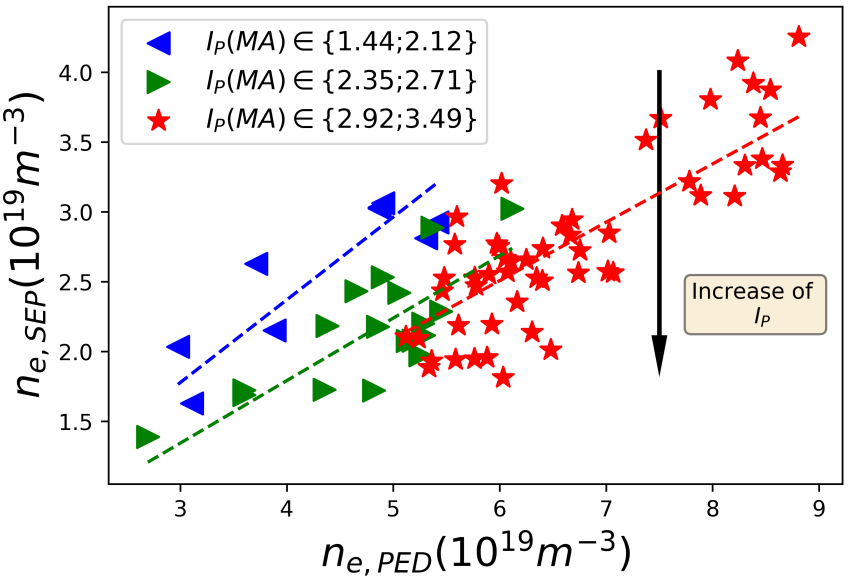

Figure 5.15: The $n_{e,SEP}$ as a function of $n_{e,PED}$ with classification with respect to three $I_P(MA)$ in Corner-Corner configuration.

sub-dataset a remarkable trend is the decreasing of $n_{e,SEP}$ while B_T and I_P increase as shown in figures 5.15 and 5.16. The dataset is quite large in this case. Then we look at the behaviour with respect to P_{SOL} (see figure 5.17). A clear increase of the ratio $n_{e,SEP}$ over $n_{e,PED}$ is observed corresponding to an increase of the injected power, or equivalently the power flowing into the SOL, P_{SOL}.

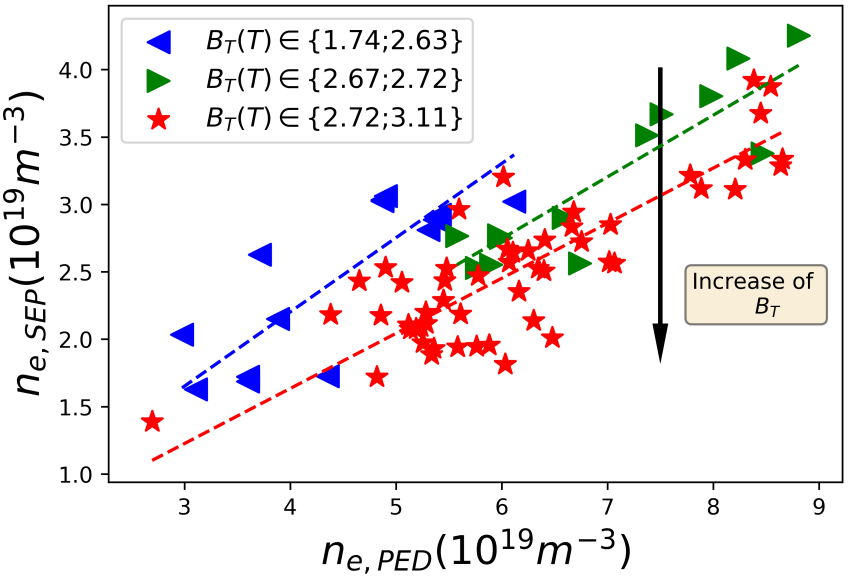

Figure 5.16: The $n_{e,SEP}$ as a function of $n_{e,PED}$ with classification for $B_T(T)$ in Corner-Corner configuration.

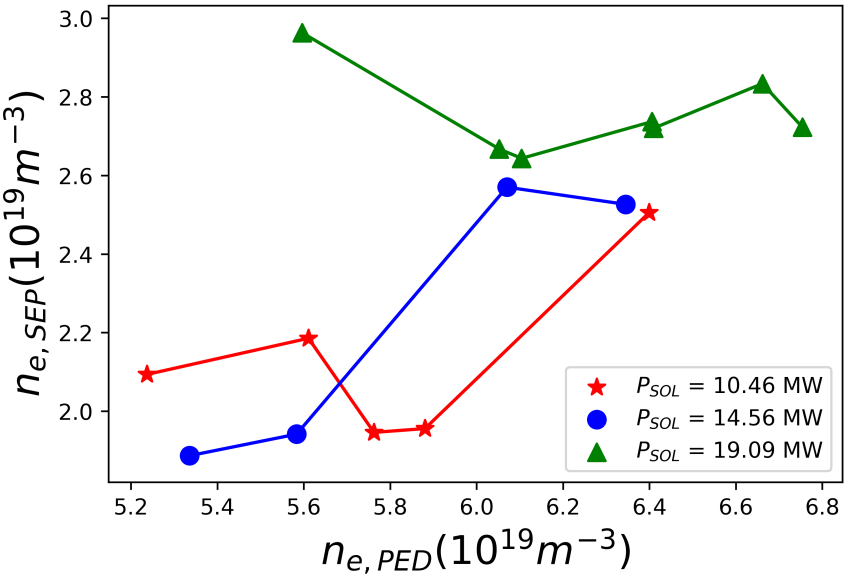

Figure 5.17: The $n_{e,SEP}$ as a function of $n_{e,PED}$ with classification for $P_{SOL}(MW)$ in Corner-Corner configuration.

5.3.2 Analysis of plasma discharges in Vertical-Horizontal divertor magnetic configuration

Concerning the Vertical-Horizontal divertor magnetic configuration sub-dataset, we observe an inverse relation between $n_{e,SEP}$ and the engineering parameters B_T and I_P, as shown in figure 5.18 and figure 5.19. Analysing the relation between $n_{e,SEP}$ and B_T in data shows

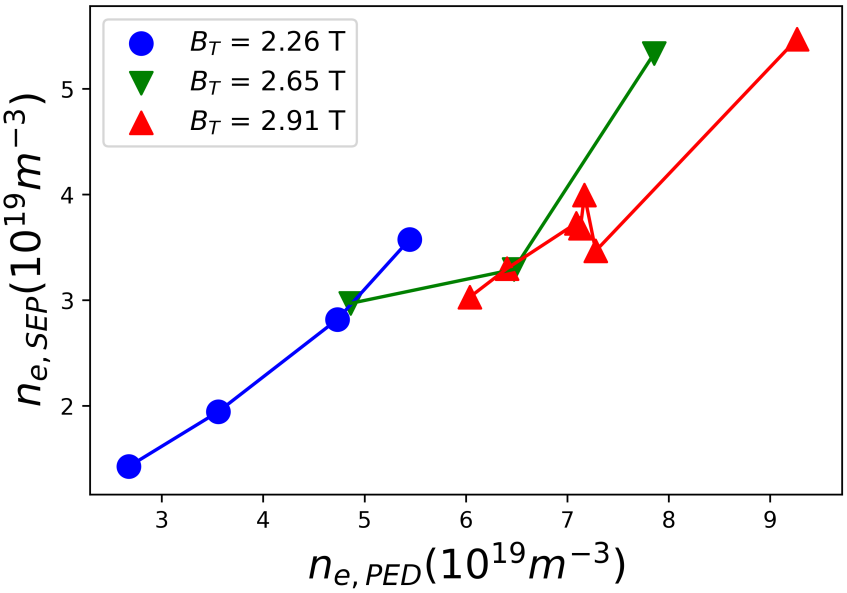

Figure 5.18: The $n_{e,SEP}$ as a function of $n_{e,PED}$ with classification for $B_T(T)$ in Vertical-Horizontal configuration.

a proportional increase of $n_{e,SEP}$ during a smooth increase of B_T, approximately a change $|\Delta B_T| \sim 0.3T$ casuses an increase of $|\Delta n_{e,SEP}| \sim 1.0 \times 10^{19} m^{-3}$ but the data is not abundant and these approximations might change for new experiments. For the case of I_P the inverse relation with $n_{e,SEP}$ is held and in figure 5.19 the variation of plasma current $|\Delta I_P| \sim 0.2MA$ indicates a change $|\Delta n_{e,SEP}| \sim 0.2 \times 10^{19} m^{-3}$, and for a change of $|\Delta I_P| \sim 0.4MA$ th change in $n_{e,SEP}$ is $|\Delta n_{e,SEP}| \sim 0.4 \times 10^{19} m^{-3}$. these analyses seem to confirm that the behavior of the ratio n_{SEP} over n_{PED} with respect to B_T and I_P variations are similar.

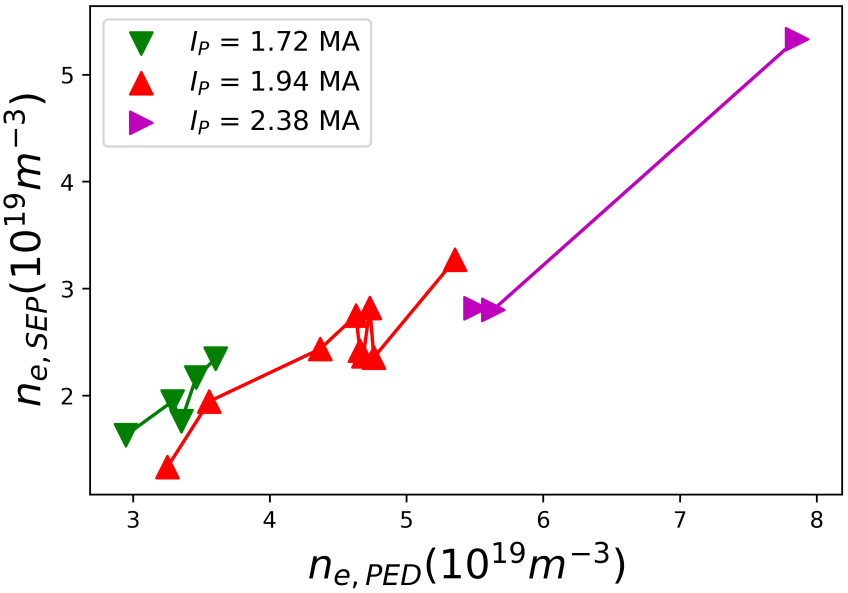

Figure 5.19: The $n_{e,SEP}$ as a function of $n_{e,PED}$ with classification for $I_P(MA)$ in Vertical-Horizontal configuration.

5.3.3 Separatrix density and temperature analysis in terms of divertor magnetic configurations

We consider now the ensemble of discharges plotting $n_{e,SEP}/n_{e,PED}$ for total JET dataset labelled with respect to the divertor magnetic configuration, as shown in 5.20. In figure 5.20,

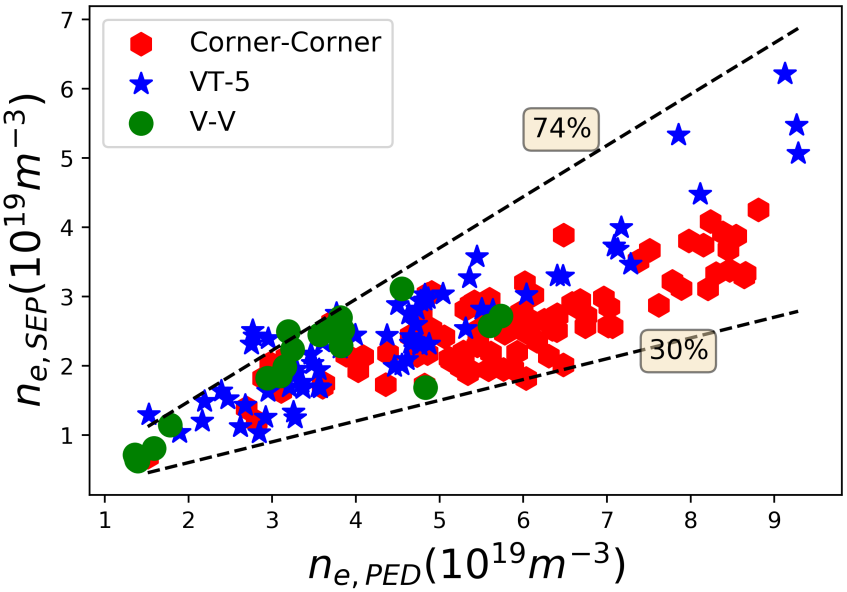

Figure 5.20: The $n_{e,SEP}$ as a function of $n_{e,PED}$ limited by $n_{e,SEP}/n_{e,SEP}|_{min}$ (upper dashed black line) and $n_{e,SEP}/n_{e,SEP}|_{max}$ (lower dashed black line).

the three different subsets show seemingly an increase of separatrix density while divertor magnetic configuration scans Corner-Corner, Vertical-Horizontal and Vertical-Vertical configurations respectively. Nevertheless the Corner-Corner, Vertical-Horizontal and Vertical-Vertical datasets show a scattering bearing particularly for low pedestal density. In consequence, the datasets overlap in some regions causing an argument's weakening upon the increasing of separatrix density while divertor magnetic configuration is changing. Before continuing this analysis in the following section, we present the behavior of the separatrix temperature as a function of top pedestal density n_{PED}, labelled in terms of divertor magnetic configuration (see figure 5.22).

The electron separatrix temperature for low pedestal density is perceptible to pedestal density changes, and increment of pedestal density causes an increment in collisional rates

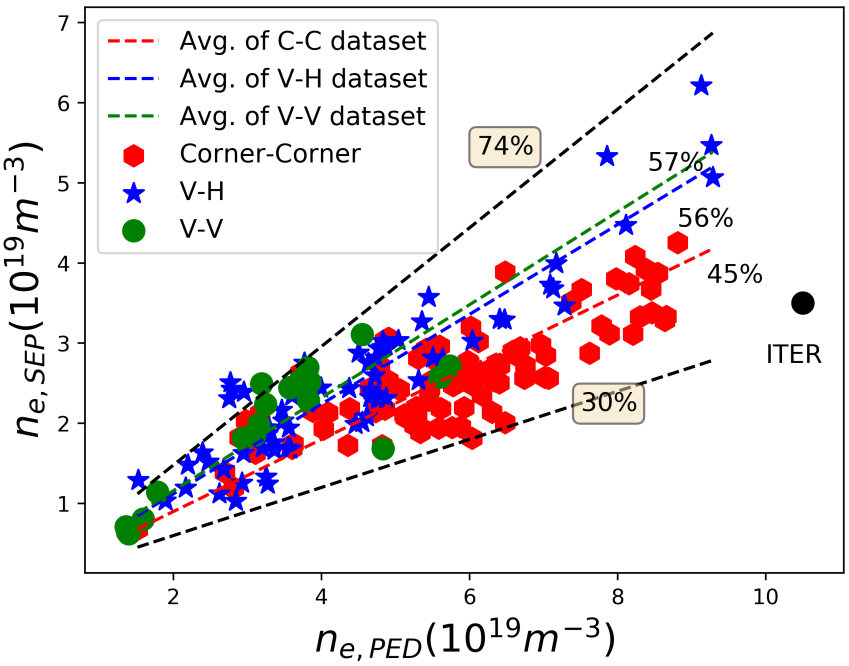

Figure 5.21: The $n_{e,SEP}$ as a function of $n_{e,PED}$ limited by $n_{e,SEP}/n_{e,SEP}|_{min}$ (upper dashed black line) and $n_{e,SEP}/n_{e,SEP}|_{max}$ (lower dashed black line). The internal dashed lines represent the average of each one of the sub-datasets correspondingly to Corner-Corner, Vertical-Horizontal and Vertical-Vertical configuration.

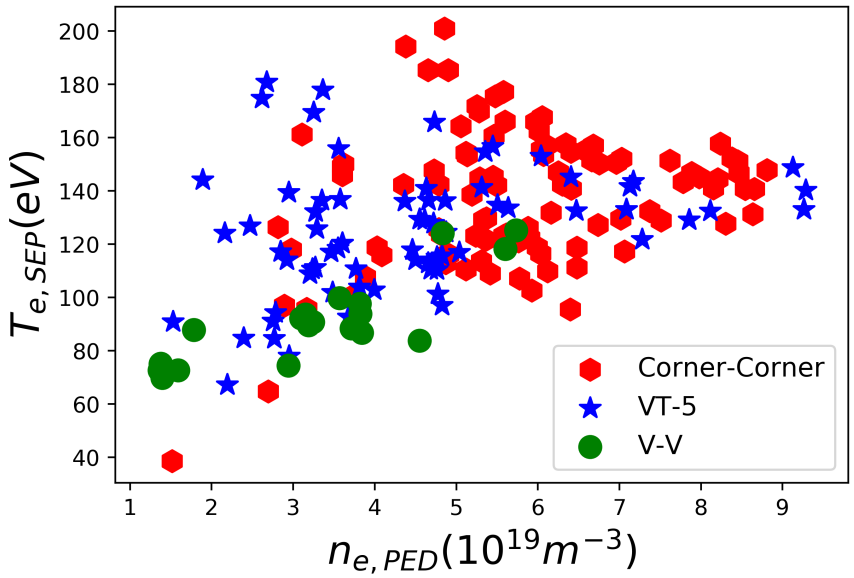

Figure 5.22: $T_{e,SEP}$ as a function of $n_{e,PED}$.

concluding with a lower electron separatrix temperature by consequence of radiation dissipated by collisions. Besides, for low pedestal density, an increase in heating power, mainly

neutral beam injection, boosts the kinetic energy of plasma breeding an increase of temperature as figure out in equation 2.94.

Instead, for a high pedestal density, an increase of this does not have a relevant impact on temperature since particles are whitin a 'crowded state' where collisions do not play an important role for change in temperature and an increase in heating power causes an increment of electron temperature by consequence of kinetic energy as figure out in equation 2.95. Then electron separatrix temperature is almost constant for high pedestal density, increasing humbly while heating power is increasing and for an increase of pedestal density the temperature decreases slowly as figure out the equation 2.93 and shown in figure 5.22.

5.4 JET dataset analysis under H_{98} parameter

In the previous section we have seen that the divertor magnetic configuration seems to have an impact on the ratio between n_{SEP} and n_{PED}. This could be reformulated in terms of quality of confinement because it is known that in JET operating in Corner Corner configuration, for example, corresponds with a better core confinement. We introduce the H_{98} parameter to quantify such quality of confinement and we present the analysis of the database with respect to this parameter. Figures 5.23, 5.24 and 5.25 clearly show that one should introduce the H_{98} parameter inro the scaling law, in particular to see if there is a better description for high n_{PED} values.

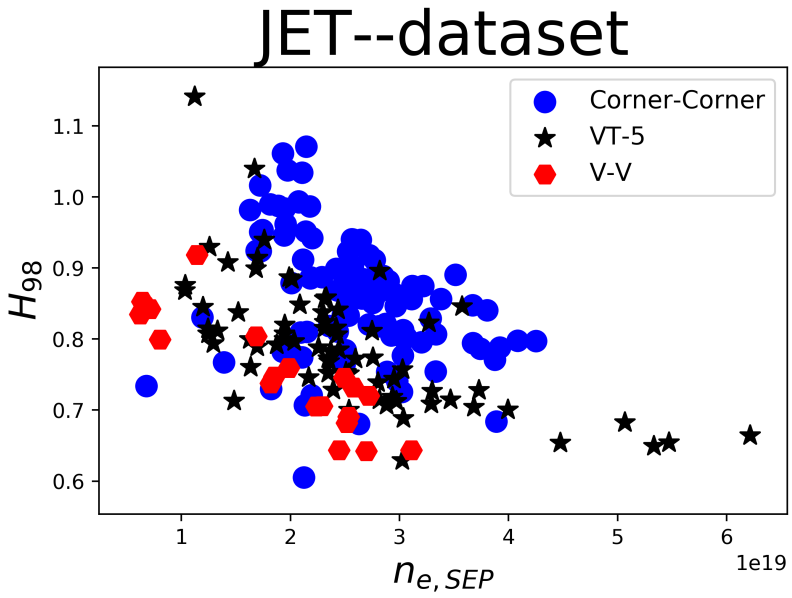

Figure 5.23: H_{98} as a function of $n_{e,SEP}$.

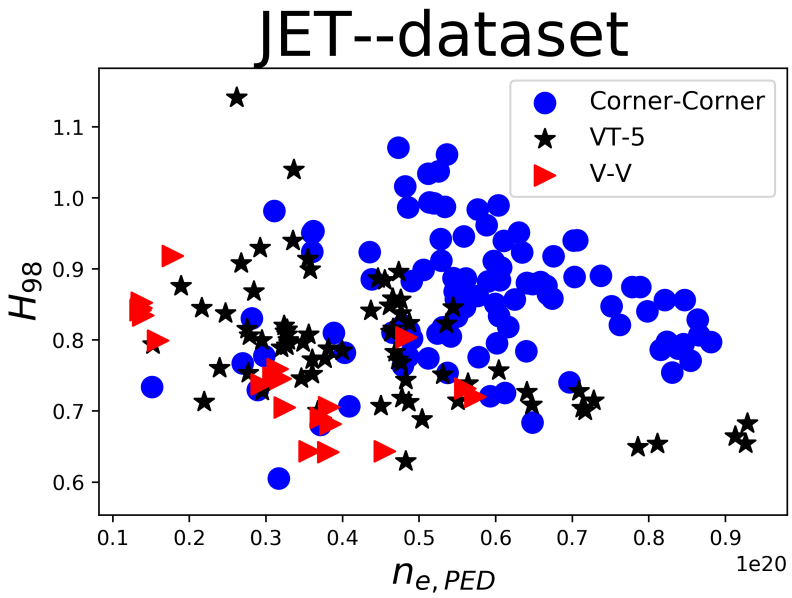

Figure 5.24: H_{98} as a function of $n_{e,PED}$.

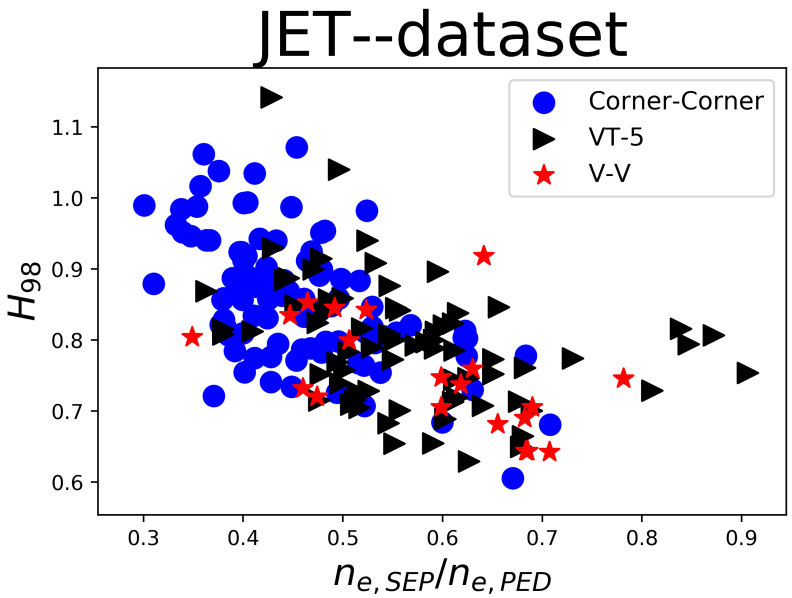

Figure 5.25: H_{98} as a function of $n_{e,SEP}/n_{e,PED}$.

5.5 Scaling law taking into account the H_{98} parameter

The engineering parameters I_P and H_{98} influence the quality of confinement with impact on the heat flux exhausting described on subsection 5.1 where I_P holds a direct relation direct relation with $n_{e,PED}$ exposed in figure 5.2. On side of $n_{e,SEP}$ due to the fusion is going on well then the heat flux coming from core towards SOL breeds an increment of $T_{e,SEP}$ with a consequently decrease of $n_{e,SEP}$ as is indicated in equation 5.1 and in figure 5.26.

This current subsection 5.5 uses results of H_{98} shown in figures 5.23, 5.24 and 5.25, and links quality of confinement directly to an scaling law referred in equation 5.1. The quality of confinement in the same way that I_P might increases $T_{e,SEP}$ causing a decrease of $n_{e,SEP}$ as shown figure 5.23 then showing that H_{98} should save an inverse relation with $n_{e,SEP}/n_{e,PED}$ as shown in figure 5.25.

The resultant scaling law shows, in equation 5.2, the impact of I_P and P_{TOT} to the quality of confinement and the heat flux coming towards SOL, allowing us to propose a tentative scenario where the performance of confinement during H-mode reachs an optimal state while the heat flux spreaded on target is reduced to possible minimum.

$$n_{e,SEP} \propto n_{e,PED}^{0.81} P_{TOT}^{0.21} I_P^{-0.43} H_{98}^{-1.14} \tag{5.2}$$

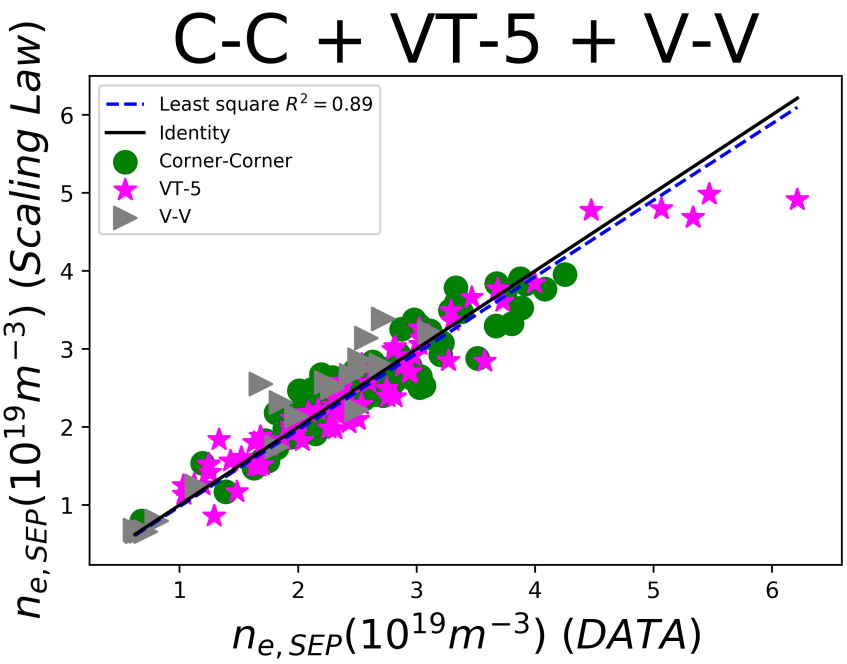

Figure 5.26: The experimental separatrix density versus the expectation from scaling law of equation 5.2. The dashed line represents 89% of exected value.

5.6 Two point model comparison

The two point model is an ideal image for the parallel transport region in a tokamak with a divertor configuration. The model just considers two geometrical points, the outer mid-plane and the target, to analyse the transport of the heat flux in these two points. The $T_{e,SEP}$ and $n_{e,SEP}$ are two of the most important magnitudes in the tokamak data, and using the two-point model equations represented in 2.58 and 2.82 a relation among $T_{e,SEP}$ and $n_{e,SEP}$ is represented in 2.86 and 2.89 for $T_{e,SEP}$ as a function of $n_{e,SEP}$.

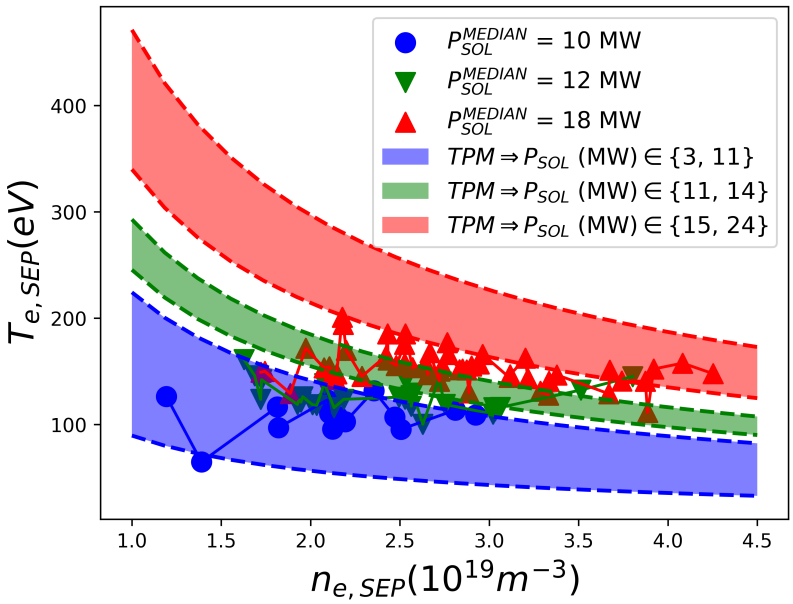

Figure 5.27: $T_{e,SEP}$ as a function of $n_{e,SEP}$ and the TPM comparison for C-C magnetic configuration.

P_{SOL}	B_T	I_P	q_{95}	λ_q
$3-11MW$	$2.61T$	$2.55MA$	3.17	$3.23mm$
$11-14MW$	$2.50T$	$2.60MA$	3.0	$2.71mm$
$15-24MW$	$2.76T$	$2.92MA$	2.97	$2.16mm$

Table 5.3: Averaged values for the two-point model comparison in C-C configuration.

$$\frac{2}{\gamma e}\sqrt{\frac{m_i}{2e}}\left(\frac{q_{||,SEP}}{n_{e,SEP}}\right)^7 + \left(\frac{7L_{||}}{2\kappa_{0e}}\right)q_{||,SEP}\eta^2 - \eta^3 = 0$$

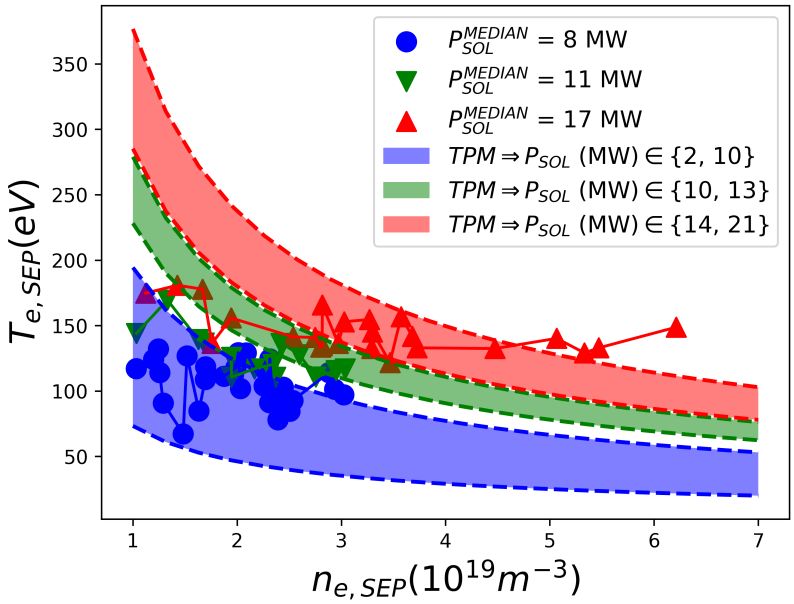

Figure 5.28: $T_{e,SEP}$ as a function of $n_{e,SEP}$ and the TPM comparison for VT-5 magnetic configuration.

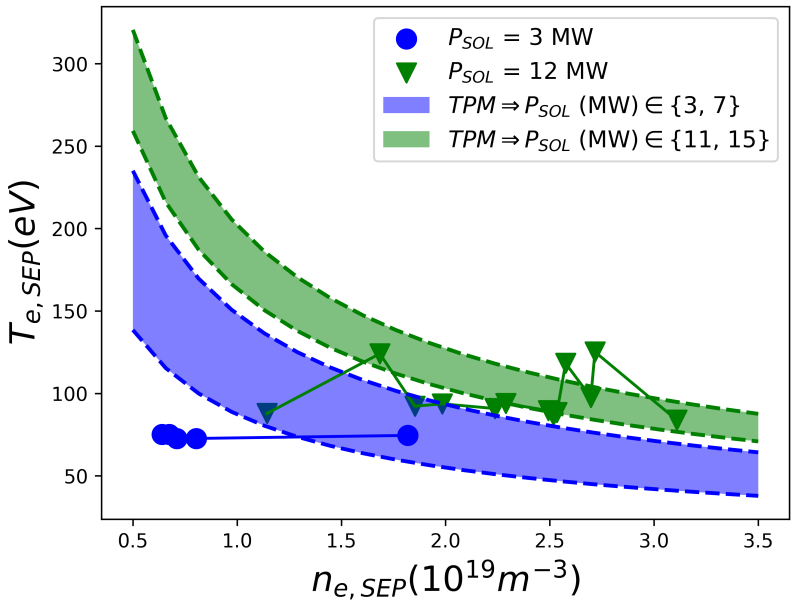

Figure 5.29: $T_{e,SEP}$ as a function of $n_{e,SEP}$ and the TPM comparison for V-V magnetic configuration.

where $\eta = T_{e,SEP}^{7/2}$, $q_{||,SEP} = \frac{1/4P_{SOL}}{A} = \frac{1/4P_{SOL}}{2\pi R\lambda_q}\frac{|B|}{B_P}$.

Harnessing equation 2.86 the curve $n_{e,SEP}$ vs $T_{e,SEP}$ is classified as a function of P_{SOL} while other parameter remains constant.

P_{SOL}	B_T	I_P	q_{95}	λ_q
$3-7MW$	$2.61T$	$2.55MA$	3.17	$3.23mm$
$11-15MW$	$2.50T$	$2.60MA$	3.0	$2.71mm$

Table 5.4: Averaged values for the two-point model comparison in V-V configuration.

The JET dataset is divided to magnetic configurations and each one of these subsets are labeled like P_{SOL} functions, the subdatasets are plotted upon the curve $n_{e,SEP}$ vs $T_{e,SEP}$ with the same P_{SOL} classification and they are illustrated in figures 5.13, 5.14 and 5.15. A trend for each one of curves in figures 5.15, 5.14 and 5.15 is the increasing of $T_{e,SEP}$ when P_{SOL} increases, for the theoretical representation an inverse dependency between $T_{e,SEP}$ and $n_{e,SEP}$ is evident and for high values of $n_{e,SEP}$ a slowly decreasing of $T_{e,SEP}$ is observed. For Corner-Corner magnetic configuration represented in figure 5.13 the dataset is located in zone of short-variations for $T_{e,SEP}$ but remaining the trend of slowly decreasing, the values for $n_{e,SEP}$ in this magnetic configuration are low, $n_{e,SEP} \in \{1.5, 4.5\}(\times 10^{19} m^{-3})$, and with high values of $n_{e,PED}$ represented in figure 5.17 the ratio of $n_{e,SEP}/n_{e,PED}$ is the lowest one between magnetic configurations and it means lower values of $n_{e,SEP}$ are out of the density limit represented in figure 5.9 since these hypothetical lower values would not can remain the confinement. For Vertical-Horizontal dataset the range for $n_{e,SEP}$ is longer, $n_{e,SEP} \in \{1.0, 7.0\}(\times 10^{19} m^{-3})$, and the increasing of P_{SOL} is still leading an increasing in $T_{e,SEP}$. The V-H data points match with the forecast of two-point model with close agreement.

Depending of the position and the intensity of the load on the target the counting of scattered particles coming into the core generates a radiation of the bulk, this condition support the reaching of low values for $n_{e,SEP}$. Nevertheless the P_{SOL} variation does not just affect to $n_{e,SEP}$ otherwise it will have direct effect on $n_{e,SEP}$ and $T_{e,SEP}$, e.g., an increment of P_{SOL} leads an increase of $T_{e,SEP}$ even when it causes a high $n_{e,SEP}$ and it probably happens because this increasing of P_{SOL} is affecting the $n_{e,SEP}$ and by effect of P_{SOL} increasing the $n_{e,PED}$ is decreasing and this decreasing is consequence of the overloading of pressure in the

pedestal zone, deprecating the quality of confinement during H-mode. A difference between dataset and two-point model forecast is focused in low- $n_{e,SEP}$ region, in this region the change in P_{SOL} might be affecting more the quality of the confinement decreasing H_{98} or decreasing $n_{e,PED}$ as is illustrated in figure 5.24, and the effect on $T_{e,SEP}$ is just the linear effect of increasing like is illustrated in figures 5.27, 5.28 and 5.29.

5.7 Investigation of density behavior in a series of SolEdge 2D transport code simulations

SOLEDGE2D is a 2D transport code that solves fluid equations (density, parallel velocity, ions and electrons temperatures) and toroidal axisymmetry is assumed being the domain reduced to a poloidal cross-section. The boundary conditions in SOLEDGE2D are imposed by using a penalization technique. This method allows the simulation domain to be extended from the plasma to the solid components where the equations are modified to recover the standard Bohm boundary conditions at the interface. In order to model the particle source that comes from the neutralization of plasma pairs onto the wall, SOLEDGE2D is coupled with the EIRENE code based on a Monte-Carlo method [3].

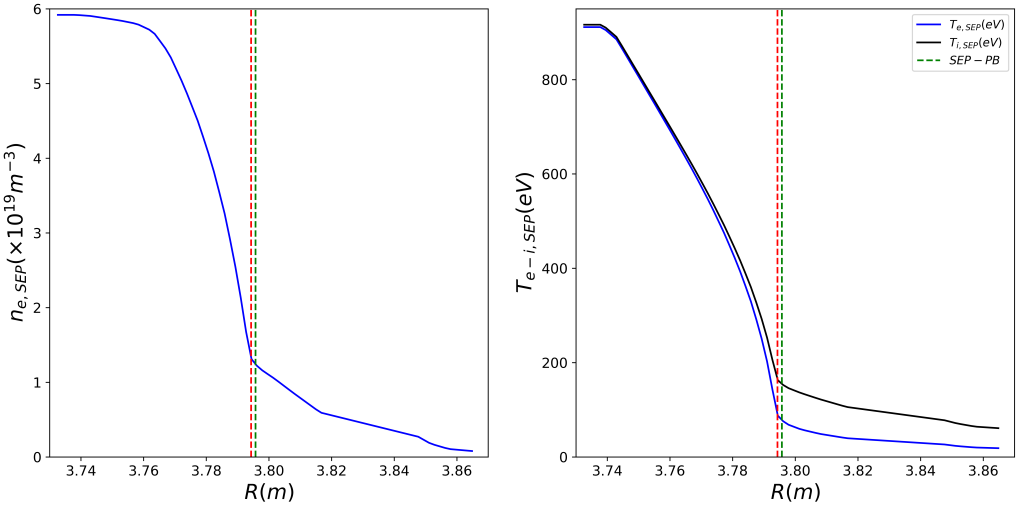

Figure 5.30: Separatrix positions given by power balance method for JPN94210-1040.

5.7.1 P_{SOl} scan on S2D

1. For the transition 94210-1040 $\Rightarrow$ 94210-1050, P_{SOL} changes from $8.4MW$ to $12MW$. This changes cause an increase of $35eV(19\%)$ on $T_{e,SEP}$ and a decrease of $0.06 \times 10^{19} m^{-3}(3\%)$ on $n_{e,SEP}$.

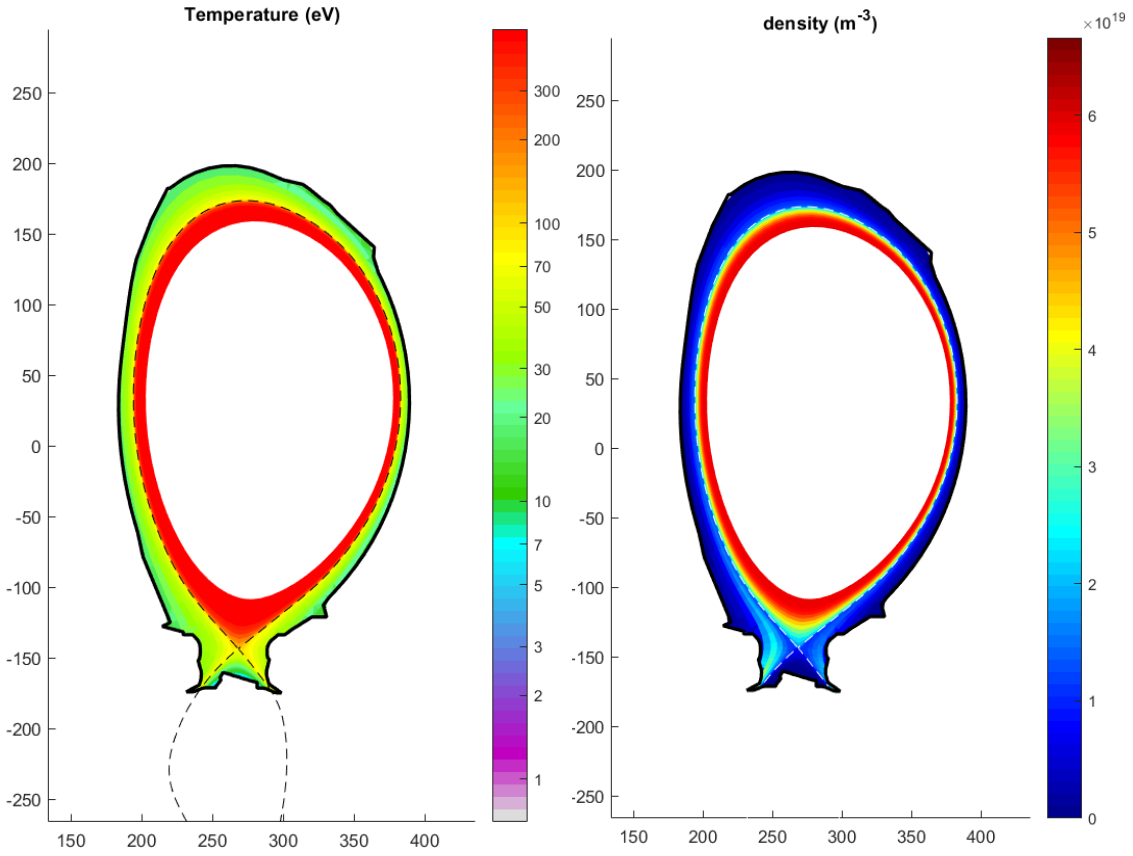

Figure 5.31: Electron temperature and density poloidal profiles for JPN94210-1040.

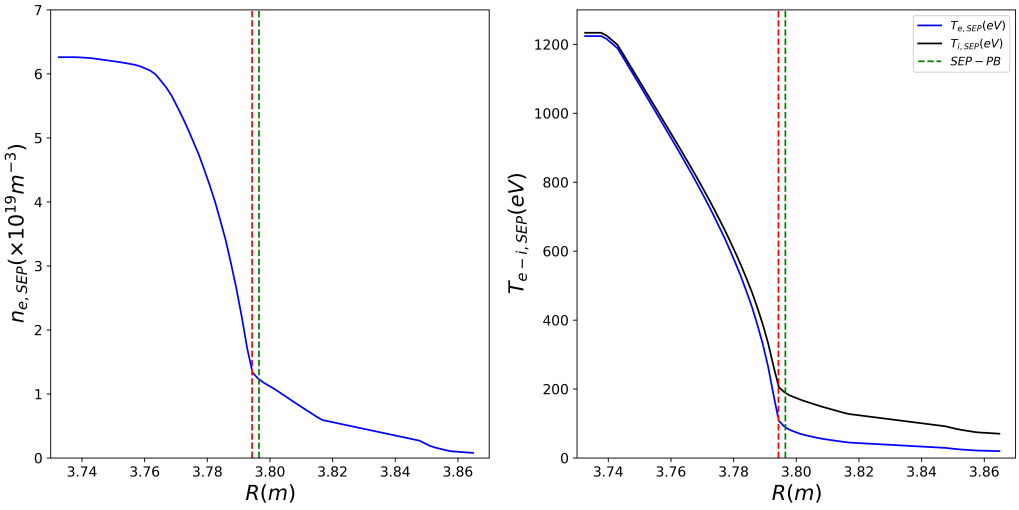

Figure 5.32: Separatrix positions given by power balance method for JPN94210-1050.

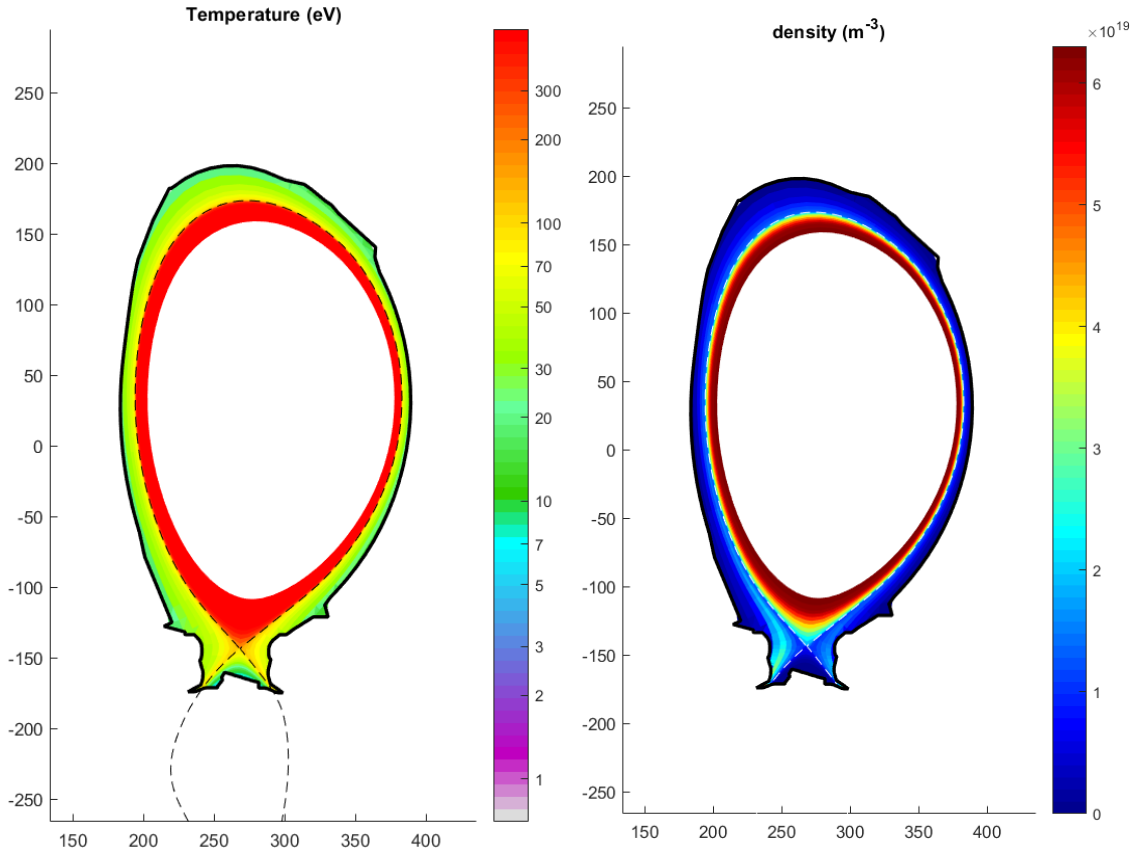

Figure 5.33: Electron temperature and density poloidal profiles for JPN94210-1050.

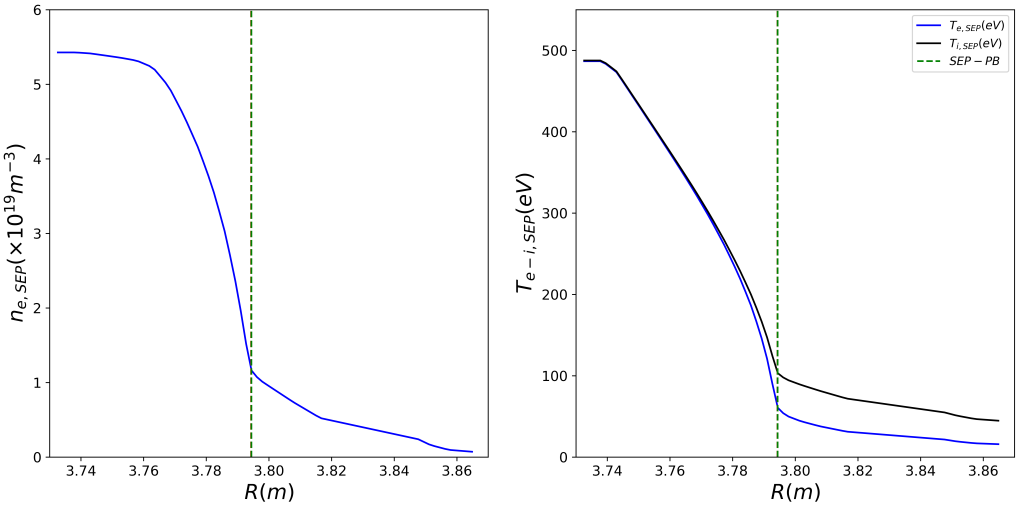

Figure 5.34: Separatrix positions given by power balance method for JPN94210-1060.

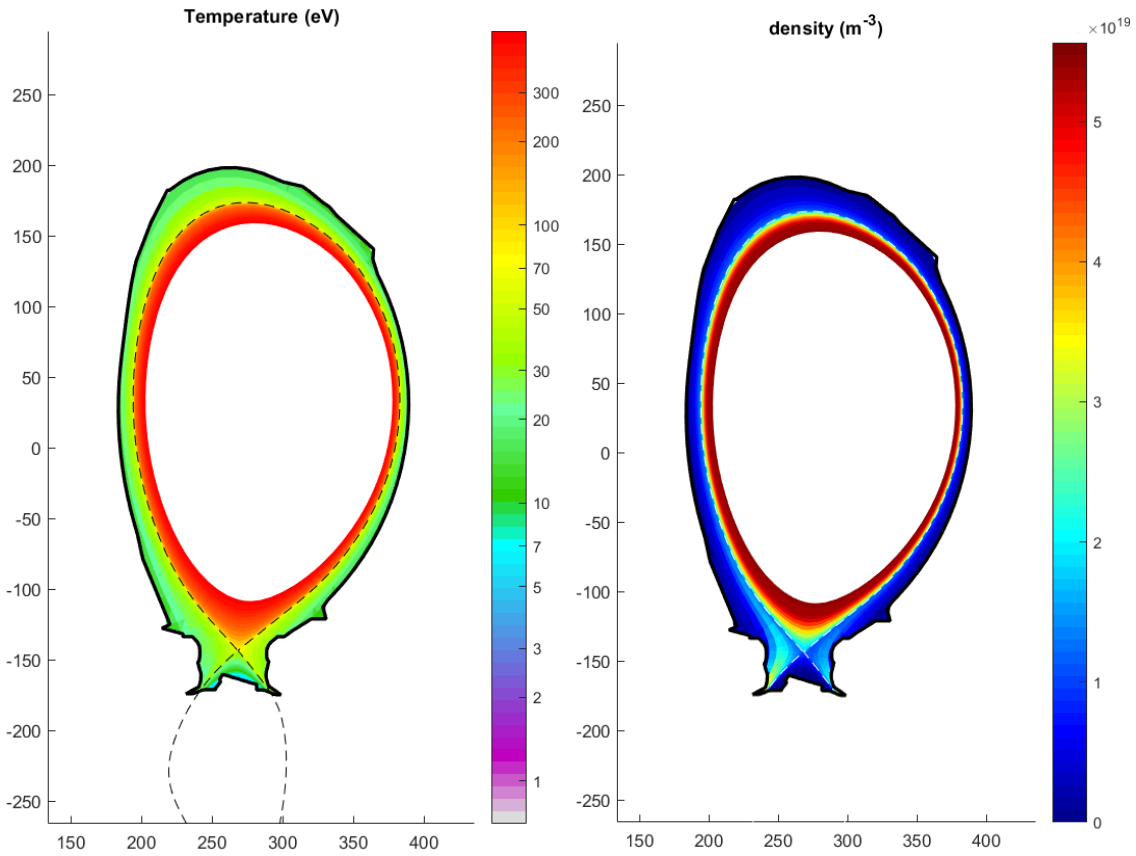

Figure 5.35: Electron temperature and density poloidal profiles for JPN94210-1060.

$B_T = 2.85T$, $I_P = 2.5MA$, $q_{95} = 3$			
PULSE	**Psol**	Γ_{CORE}^{from}	Ψ_{gas}
94210-1040	8.4 MW (**Ground**)	$1.5 \times 10^{21} m^{-2} s^{-1}$	$4.4 \times 10^{21} + 11.3 \times 10^{21} atoms.s^{-1}$
94210-1050	12 MW	$1.5 \times 10^{21} m^{-2} s^{-1}$	$4.4 \times 10^{21} + 11.3 \times 10^{21} atoms.s^{-1}$
94210-1060	4 MW	$1.5 \times 10^{21} m^{-2} s^{-1}$	$4.4 \times 10^{21} + 11.3 \times 10^{21} atoms.s^{-1}$
94210-1070	12 MW	decreasing Γ_{CORE}^{from}	same Ψ_{gas}
94210-1080	4 MW	increasing Γ_{CORE}^{from}	same Ψ_{gas}
94210-1090	12 MW	same Γ_{CORE}^{from}	decreasing Ψ_{gas}

Table 5.5: Summary of simulated pulses in SOLEDGE2D based on JPN 94210

PULSE	P_{SOL}	$T_{e,SEP}^{kin}$	$n_{e,SEP}^{kin}$	$T_{e,SEP}^{Sp}$	$n_{e,SEP}^{Sp}$
94210-1040	$8.4MW$	$78eV$	$1.24 \times 10^{19} m^{-3}$	$67eV$	$1.15 \times 10^{19} m^{-3}$
94210-1050	$12MW$	$89eV$	$1.23 \times 10^{19} m^{-3}$	$76eV$	$1.13 \times 10^{19} m^{-3}$

Table 5.6: Transition between JPN9420-1040 to JPN9420-1050.

2. For the transition 94210-1040 $\Rightarrow$ 94210-1060, P_{SOL} changes from $8.4MW$ to $4MW$. This changes cause a decrease of $56eV(30\%)$ on $T_{e,SEP}$ and an increase of $0.08 \times 10^{19}m^{-3}(4\%)$ on $n_{e,SEP}$. The inverse relation between $T_{e,SEP}$ and $n_{e,SEP}$ obtained in the results of S2D simulations are coherent with results of two-point model exhibit in figures 5.27,5.28 and 5.29.

PULSE	P_{SOL}	$T^{kin}_{e,SEP}$	$n^{kin}_{e,SEP}$	$T^{Sp}_{e,SEP}$	$n^{Sp}_{e,SEP}$
94210-1040	$8.4MW$	$78eV$	$1.24 \times 10^{19}m^{-3}$	$67eV$	$1.15 \times 10^{19}m^{-3}$
94210-1060	$4MW$	$61eV$	$1.18 \times 10^{19}m^{-3}$	$54eV$	$1.07 \times 10^{19}m^{-3}$

Table 5.7: Transition between JPN9420-1040 to JPN9420-1060.

5.7.2 Extra parameters variation on S2D

1. For the transition 94210-1050 $\Rightarrow$ 94210-1070, Γ^{from}_{CORE} suffers a **decreasing** to keep constant the density at the boundary. Results show a decrease on the electron separatrix density while temperature has no changes.

PULSE	P_{SOL}	$T^{kin}_{e,SEP}$	$n^{kin}_{e,SEP}$	$T^{Sp}_{e,SEP}$	$n^{Sp}_{e,SEP}$
94210-1050	$12MW$	$89eV$	$1.23 \times 10^{19}m^{-3}$	$76eV$	$1.13 \times 10^{19}m^{-3}$
94210-1070	$12MW$	$89eV$	$1.22 \times 10^{19}m^{-3}$	$76eV$	$1.13 \times 10^{19}m^{-3}$

Table 5.8: Transition between JPN9420-1050 to JPN9420-1070.

2. For the transition 94210-1060 $\Rightarrow$ 94210-1080, Γ^{from}_{CORE} suffers an **increasing** to keep constant the density at the boundary. Results shows an increment on $n_{e,SEP}$ while changes on $T_{e,SEP}$ are neglectible.

PULSE	P_{SOL}	$T^{kin}_{e,SEP}$	$n^{kin}_{e,SEP}$	$T^{Sp}_{e,SEP}$	$n^{Sp}_{e,SEP}$
94210-1060	$4MW$	$61eV$	$1.18 \times 10^{19}m^{-3}$	$54eV$	$1.07 \times 10^{19}m^{-3}$
94210-1080	$4MW$	$61eV$	$1.21 \times 10^{19}m^{-3}$	$53eV$	$1.10 \times 10^{19}m^{-3}$
94210-1100	$4MW$	$112eV$	$3.94 \times 10^{19}m^{-3}$	$108eV$	$3.88 \times 10^{19}m^{-3}$

Table 5.9: Transition between JPN9420-1060 to JPN9420-1080.

3. For the transition 94210-1050 $\Rightarrow$ 94210-1090, Ψ_{gas} is **decreased** to keep constant the density at the boundary. The decrease of Ψ_{gas} causes a decrease of $n_{e,SEP}$ and an increasing of $T_{e,SEP}$, these results are coherent with two-point model results shown in figures 5.27, 5.28 and 5.29.

PULSE	P_{SOL}	$T^{kin}_{e,SEP}$	$n^{kin}_{e,SEP}$	$T^{Sp}_{e,SEP}$	$n^{Sp}_{e,SEP}$
94210-1050	$12MW$	$89eV$	$1.23 \times 10^{19} m^{-3}$	$76eV$	$1.13 \times 10^{19} m^{-3}$
94210-1090	$12MW$	$97eV$	$0.52 \times 10^{19} m^{-3}$	$72eV$	$0.49 \times 10^{19} m^{-3}$

Table 5.10: Transition between JPN9420-1050 to JPN9420-1090.

From the simulation results reported in these tables, the code seems to reproduce the experimental behaviour which is observed with respect to the increase and decrease of the input power. Further studies and analysis will be performed to understand better if the radial transport coefficients have to be changed depending on the density regime under consideration and if it can be used for predicting the behaviour of future machines.

Chapter 6

Interpretation of H-mode dataset for TCV tokamak

This chapter studies a TCV dataset in H-mode looking for features comparables with results showed in chapter 5 on JET tokamak.

Then TCV dataset is assayed harnessing electron separatrix and pedestal density. The two magnitudes, $n_{e,SEP}$ and $n_{e,PED}$, are expressed as a function of engineering parameters. Previously the setting of a scaling law, the total dataset of electron separatrix density and temperature are referenced to pedestal density exhibiting similar trends to JET dataset, like the limits for the ratio of separatrix density over pedestal density. The limits obtained are coherent with results of JET and it reinforces the density limit concept for discharges in H-mode. Also the total TCV dataset is displayed as function of I_P, being this parameter whoes has the bigger range of values available for the dataset, besides in figure 6.5 $n_{e,SEP}$ shows a slight decreasing while I_P increases.

In this chapter, a total of sixty-four TCV discharges in H-mode regime were analyzed, proposing a scaling law of $n_{e,SEP}/n_{e,PED}$ as function of three engineering parameters, mainly P_{TOT} and I_P on small ranges of values.

6.1 TCV discharges

The total TCV dataset is setted in H-mode regime. Then the electron density profiles exhibit a pedestal shape as shown in figures 6.1 and 6.2. Also, in figures 6.1 and 6.2 the radial

separatrix position matchs in good agreement with the separatrix provided by magnetics. Moreover, the engineering parameters linked with each one of the discharges are limited by the reduced range that they have to but the separatrix power, P_{SOL}, has an enough range to be compared with results of JET, and laying out analogous trends on the scaling law.

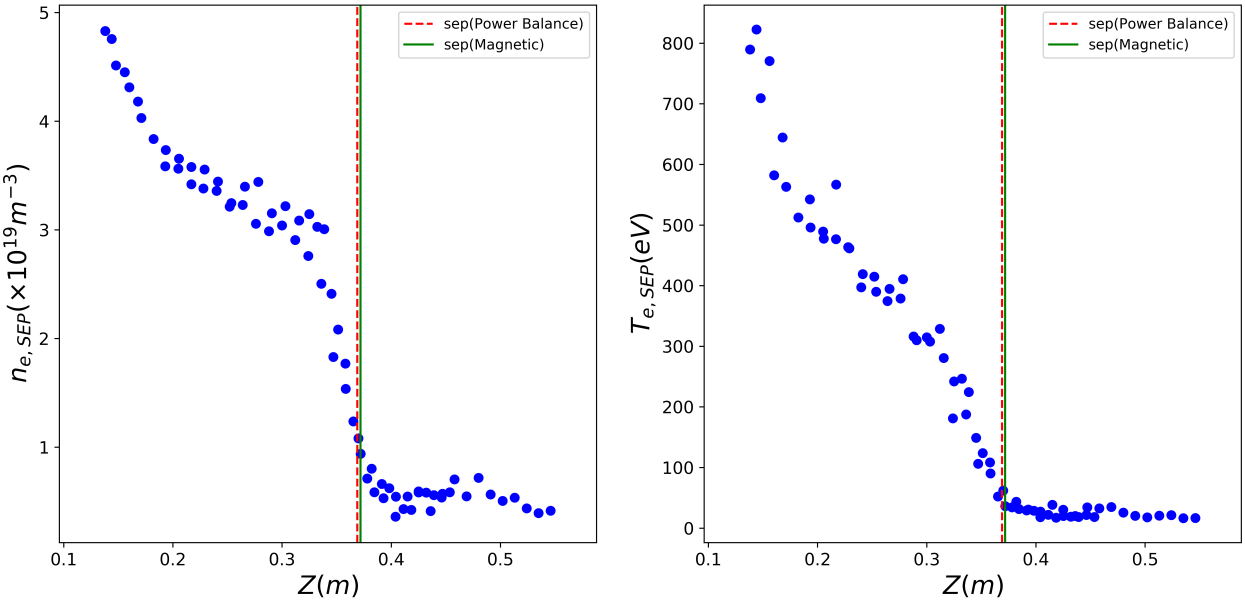

Figure 6.1: TCV pulse number 61850 is displaying a H-mode regime on the profiles of electron density and temperature. The separatrix position provided by the magnetic reconstruction, solid vertical line, and that one by power balance method, dotted red line, are referenced on this graphic.

TCV PULSE	**61850**	**61932**
$\mathbf{P_{SOL}}$	0.98 MW	1.01 MW
$\mathbf{P_{NBI}}$	0.9 MW	0.93 MW
$\mathbf{n_{e,SEP}}$	$1.11 \times 10^{19}\mathrm{m}^{-3}$	$1.88 \times 10^{19}\mathrm{m}^{-3}$
$\mathbf{n_{e,PED}}$	$2.97 \times 10^{19}\mathrm{m}^{-3}$	$3.43 \times 10^{19}\mathrm{m}^{-3}$
$\mathbf{T_{e,SEP}}$	59.6 eV	85.2 eV
$\mathbf{B_T}$	1.4 T	1.4 T
$\mathbf{I_P}$	166.68 KA	166.15 KA
$\mathbf{q_{95}}$	4.65	4.64

Table 6.1: Summary of parameters for the determination of the radial separatrix position on TCV pulses 61850 and 61932. The resulting separatrix positions are shown in figures 6.1 and 6.2.

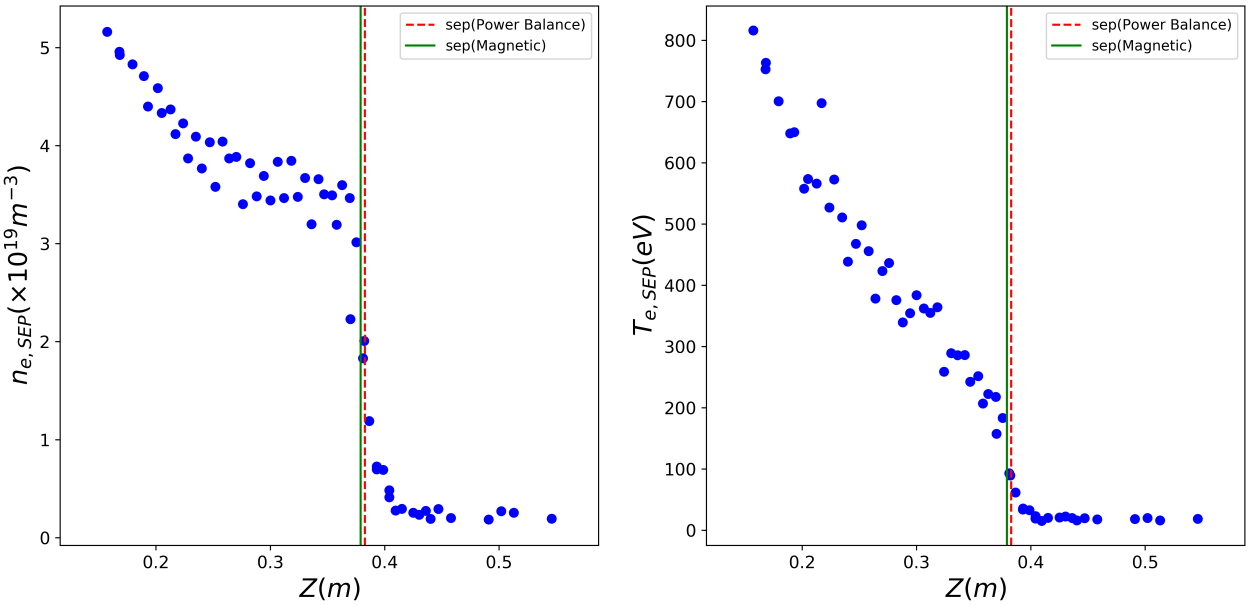

Figure 6.2: TCV pulse number 61932 is displaying a H-mode regime on the profiles of electron density and temperature. The separatrix position provided by the magnetic reconstruction, solid vertical line, and that one by power balance method, dotted red line, are referenced on this graphic.

6.1.1 TCV discharges

The TCV dataset presented in this thesis is a very challenged set of pulses extracted from many different cmapigns that between them save similarities to can perform engineering parameters scans but many other unexplored parameters might influence the dishcarges.

The TCV dataset shows in figure 6.3 a linear correspondence among electron separatrix density, $n_{e,SEP}$, and pedestal density, $n_{e,PED}$. The limits of $n_{e,SEP}/n_{e,PED}$ are 19% and 62%, keeping the enclosed behavior for $n_{e,SEP}$ showed on JET dataset and in [Leonard2017]. On side of $T_{e,SEP}$, the data is weakly scattered and the averaged electron temperature is $80eV$ evidencing an even less scattering for higher values of pedestal density that follows the correlation between the increasing of confinement quality and the reduction of the $T_{e,SEP}$ range. This dataset shows a reduction of this range of values for $n_{e,PED} \gtrsim 6 \times 10^{19}\mathrm{m}^{-3}$.

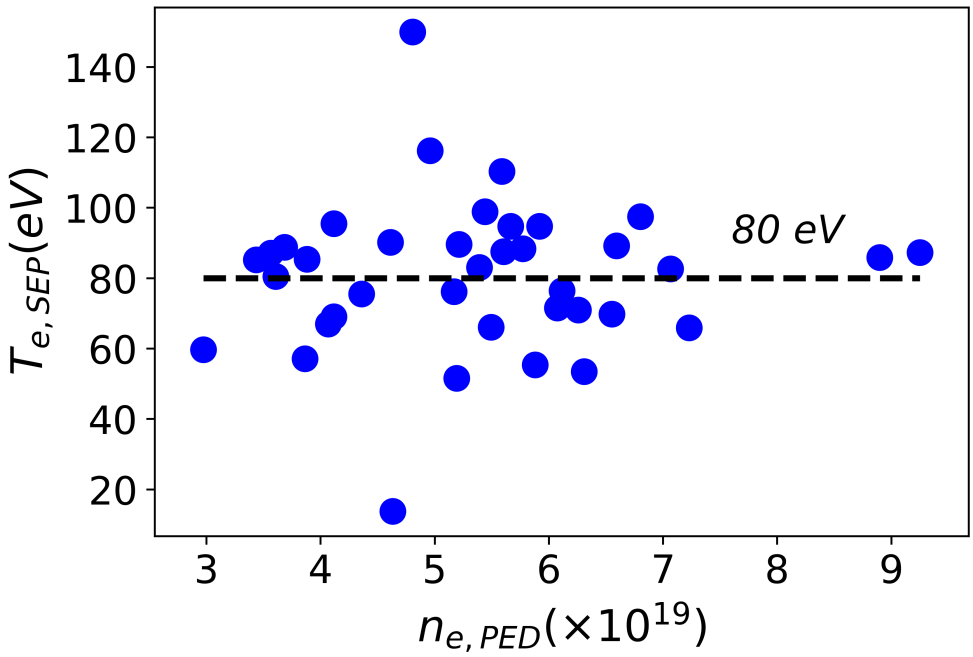

Figure 6.3: The average of electron separatrix is $80\,eV$ and for $n_{e,PED} \geq 6.0 \times 10^{19}\mathrm{m}^{-3}$ the range of $T_{e,SEP}$ is reduced.

The importance of TCV dataset lies in even when their ranges for their engineering parameters are shorts, if the trends bring values not far from those provided by JET tokamak

then the results, like scaling laws, might be considered supported unless partially because some proportionalities have been keeping even when particular relations like $I_P - B_T$ of JET are not validated for this dataset.

The limits of densities set for the ratio $n_{e,SEP}/n_{e,PED}$ as shown figure 6.4 are very relevant since they appeared in different machines and just changing a bit the values of these limits thereby can be considered that these limits are related not only with the H-mode operation or engineering parameters but with the geometry of the type of magnetic configuration.

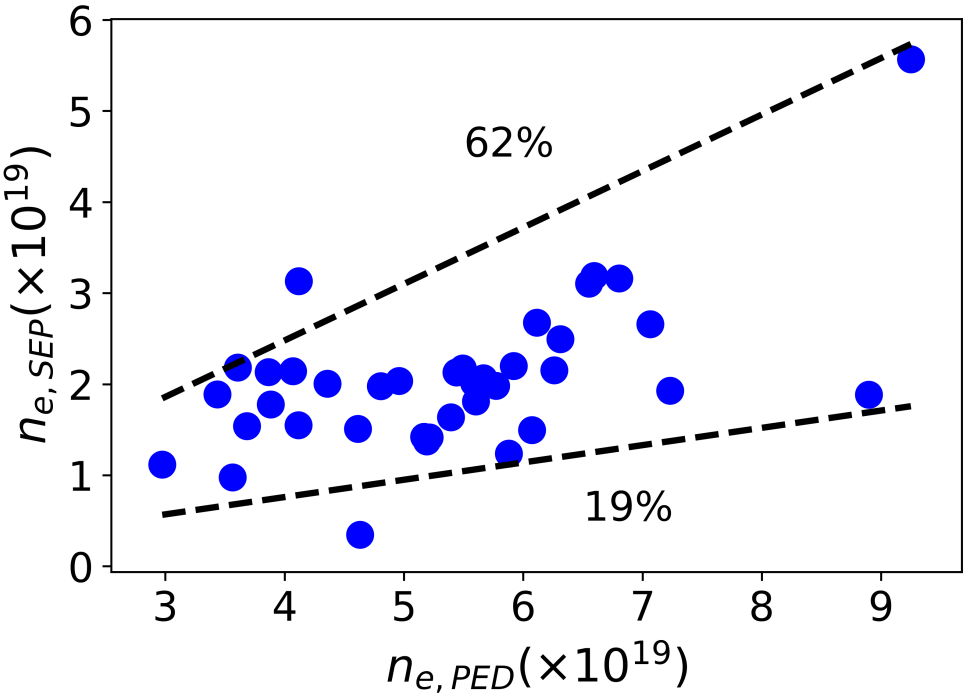

Figure 6.4: Total TCV dataset for eletron separatrix and pedestal densities. The dataset is enclosed by two limits set like $19\% \geq n_{e,SEP}/n_{e,PED} \geq 62\%$.

The range of I_P(KA) for this dataset is reduced but even for this limiting feature on figure 6.5 a faint and clear decreasing of $n_{e,SEP}$, $\gtrsim 1.0 \times 10^{19}\mathrm{m}^{-3}$ and $\lesssim 3.0 \times 10^{19}\mathrm{m}^{-3}$, appears when $n_{e,PED}$ ranges from $\gtrsim 4.0 \times 10^{19}\mathrm{m}^{-3}$ to $\lesssim 7.5 \times 10^{19}\mathrm{m}^{-3}$. On the relation between $I_P - B_T$ as shown in left-figure 6.6 this TCV dataset shows the preponderance of operating for $B_T \sim 1.425$T with a reduced presence of pulses operating with $B_T \sim 1.325$T thereby a dependency between $n_{e,SEP}$ and I_P, similar to that found for JET dataset, might evidence that even operating with a constrained parameters like $I_P - B_T$ the evolution of $n_{e,PED}$ does not change unless as function of I_P.

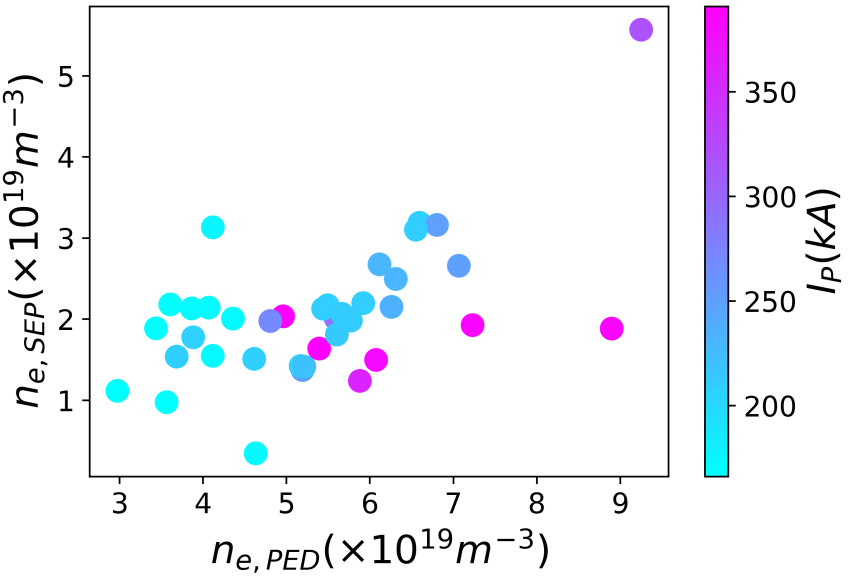

Figure 6.5: The $n_{e,SEP}$ displays a faint but clear decreasing by effect of an incresing of I_P.

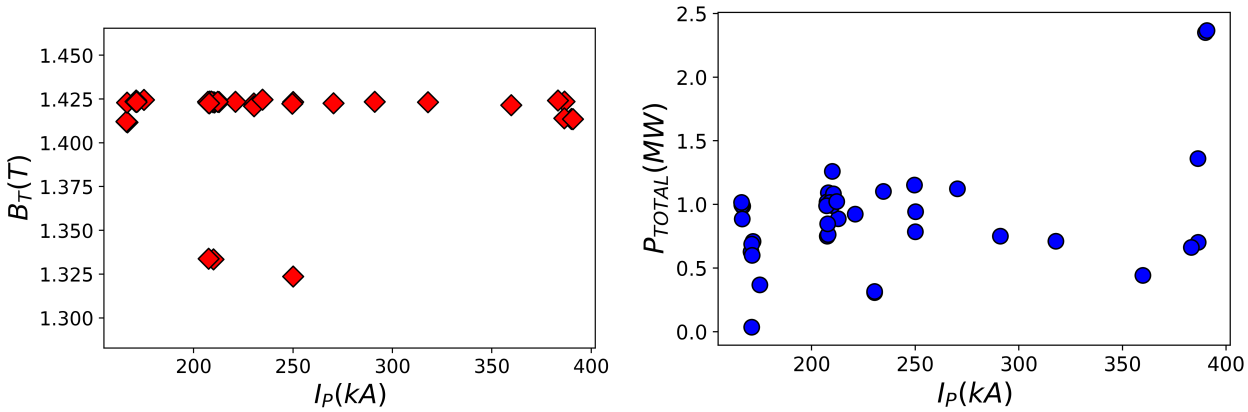

Figure 6.6: (LEFT) Almost constant relation between $B_T\,(T)$ and $I_P\,(MA)$, set with some pulses working with $B_T = 1.325$T. (RIGHT) Growing trend between $P_{TOTAL}\,(MW)$ and $I_P\,(MA)$ remarking that both factors can increase effectiveness of fusion reaction and consequently an increasing of confinement quality but with some pulses within region $[300\,\text{KA}, 380\,\text{KA}]$ that might represents pulses operating under $B_T = 1.325\,\text{T}$.

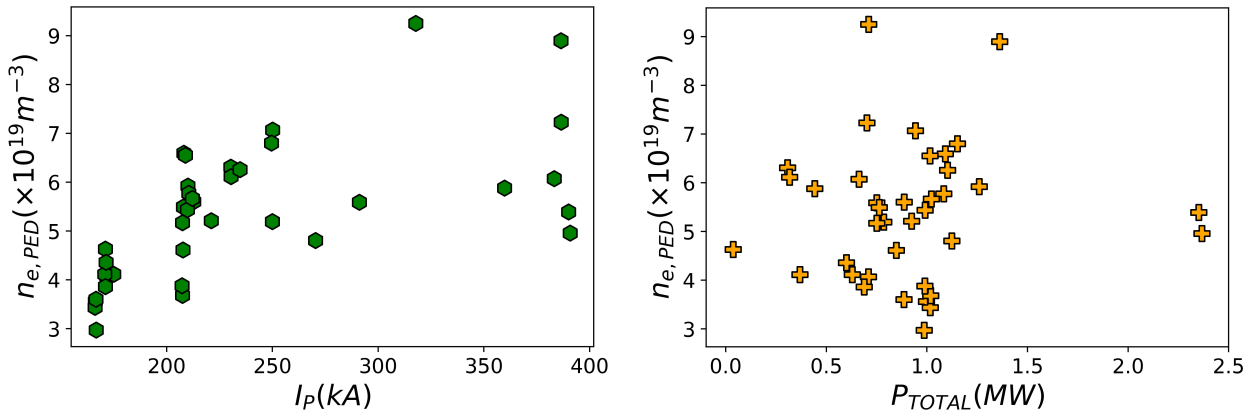

Figure 6.7: (LEFT) Growing relation between $n_{e,PED}$ and I_P, displaying a prolific impact of I_P on the quality of confinement. (RIGHT) A direct relation of $n_{e,PED}$ and P_{TOTAL} exposing a beneficial effect of increasing P_{TOTAL} on quality of confinement but some pulses for high P_{TOTAL}, $\in [2.0\,\text{MW}, 2.5\,\text{MW}]$, might be associated to $B_T = 1.325$T.

Due to the toroidal magnetic field B_T is almost constant, the trend between P_{TOTAL} and I_P as shown figure 6.6 is expectedbecause it displays a growing behavior with some data out of tendency for I_P values between 350KA and 400KA that may be associated to the reduced data points with $B_T \sim 1.325$T. Also, the figures 6.7 conserve the coherence exposed for JET dataset like the impact of I_P on the increasing of quality of confinement by consequence of more plasma fusing whose was generated increasing P_{TOTAL}.

The result of scaling law for TCV dataset support the non-negligibility of figure 6.5 because

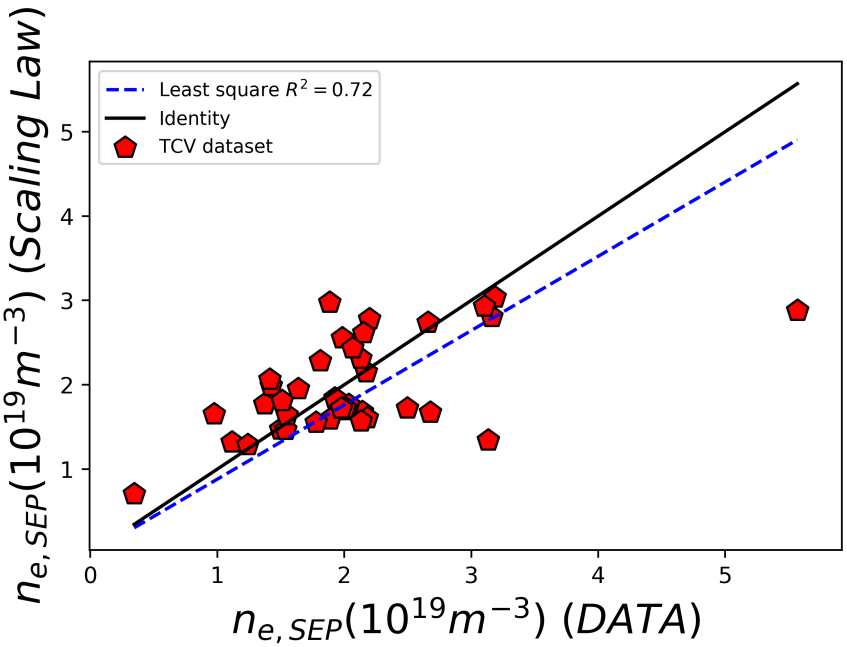

Figure 6.8: The experimental separatrix density versus the expectation from scaling law of equation in 6.1. The dashed line represents 72% of the expected value.

even working with a reduced range of I_P this range brings a dependency of $n_{e,SEP}$ near to that proposed for JET dataset. Besides the impact of P_{TOTAL}, being this part of diagnostic system, is coherent with results showed to JET dataset and exposed with figures 5.10 and 5.11. The values out of trend showed in figure 6.8 referenced the pulses erlated with $B_T \sim$ 1.325T.

$$n_{e,SEP} \propto n_{e,PED}^{1.21} P_{TOT}^{0.35} I_P^{-0.74} \tag{6.1}$$

In addition, an increasing on P_{SOL} as shown in figure 6.9 leads an increase on $T_{e,SEP}$ that saves coherence with results for JET dataset shown in figures 5.27, 5.28 and 5.29, and this trend happens despite of reduced range for P_{SOL} on TCV dataset.

Finally the TCV dataset supports the JET trends and scaling laws despite that this current TCV dataset evidences of range limitations. This results let to extrapolate the scope of scaling laws considering the operational conditions of each one of the new tokamaks to be considered.

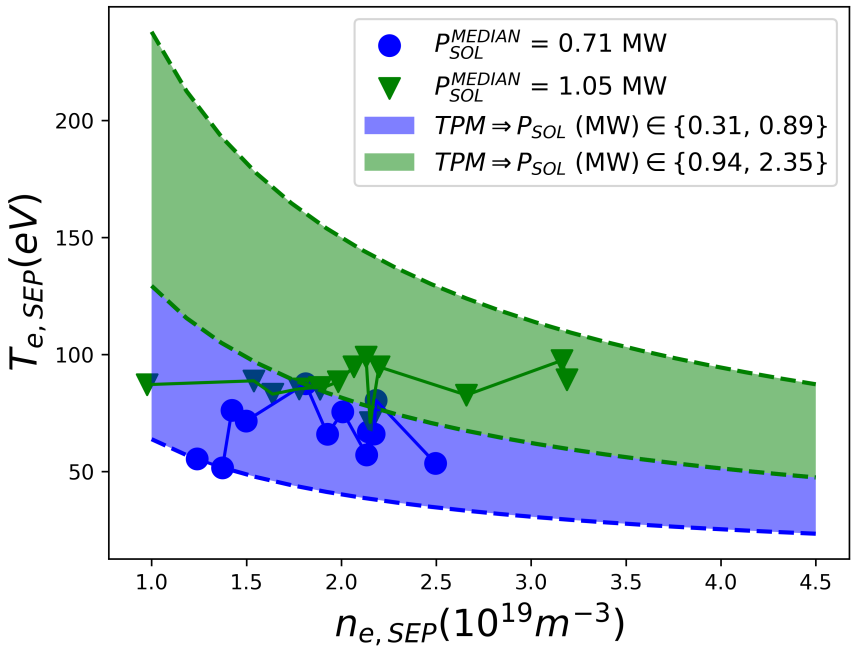

Figure 6.9: The $T_{e,SEP}$ increases while P_{SOL} increases and for low values of P_{SOL}, $\in [0.31\,\text{MW}, 0.89\,\text{MW}]$, then $T_{e,SEP}$ follows the trend leads by two-point model decreasing $T_{e,SEP}$ by effect of an increasing $n_{e,SEP}$.

6.1.2 Global scaling law: TCV + JET

The two data sets previously presented, JET and TCV, showed similar qualitative behaviour for the scaling laws relating $n_{e,SEP}/n_{e,PED}$ with engineering parameters P_{TOT} and I_P. Then a global scaling law is performed and it is figured out in equation 6.2 showing a coherent trend of the exponents of the engineering parameters comparing them with the exponents for the individual data sets. An acceptable good agreement is shown in figure 6.10 comparing this with figures 6.8 and 5.26. The points out of trend might be related with a mis-describing of the plasma regimes for the pulses considered since they are encompassed with just a unique representation, Kinetic-corrected Spitzer, for the parallel heat flux but they can be close to a detachment state that is far from the imposed description for the parallel heat flux. Then to improve the analysis of this dataset a next-step will be set to previously determine the plasma regime closer to each pulse and to reach this goal a processing of divertor electron temperature and density will be important.

$$n_{e,SEP}/n_{e,PED} \propto P_{TOT}^{0.24} I_P^{-0.20} \tag{6.2}$$

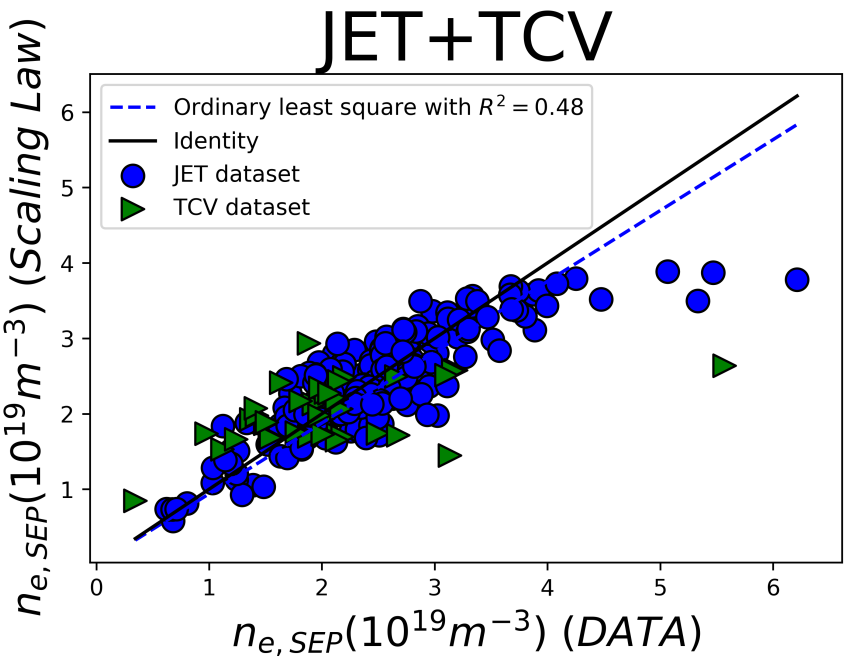

Figure 6.10: The correspondence between the separatrix electron density from scaling law and the empirical one show an acceptable agreement with some points for higher density out of trend that can be related with closer to detached density regimes being mis-described by the Kinetic-corrected Spitzer expression for the parallel heat flux.

Chapter 7

Summary and Conclusions

In this thesis I studied a large dataset of plasmas discharges in H-mode coming from JET and TCV tokamaks. The main aim of the work was to establish a scaling law about the ratio between the electron density at the outer midplane separatrix and at the top of the pedestal as a function of engineering parameters. The choice of looking at this ratio is motivated by the fact that on one side the density at the top pedestal is an indicator of core confinement and on the other side the separatrix density is strictly related to the divertor conditions.

It is essential to mention that in the dataset we considered there are not discharges that have been part of a dedicated experiment during JET or TCV campaigns. Each one of the discharges presented here was identified within of different experiments where some features were taken care of, e.g., being standard like operate under a baseline, work for ILW, etc. However, some parameters that were not identified or quantified can hold an influence over the dataset considered in this study but this condition do not avoid to display the relations that H-mode data can drive under the influence of engineering parameters.

During this study mid-plane $n_{e,SEP}$ is measured and characterized as a function of $n_{e,PED}$ and engineering parameters like P_{TOT}, B_T and I_P. In order to determine the separatrix density I applied a power balance method which is described in chapter 4. I have shown that, as expected, with such a method the separatrix position is influenced from the choice of the heat fux expression. We compared the separatrix position predicted by the power balance method using several heat flux expressions and we chose the kinetically corrected

Spitzer one. This choice has been analysed on numerical simulation results obtained with the edge transport code SOLEDGE-EIRENE. In that case the separatrix position obtained with the power balance method is compared with the position known from the mesh-grid built on a given magnetic equilibrium and used for running the simulation. With this sort of verification I have sown that for typical JET H-mode discharges the power balance method using a kinetically corrected Spitzer expression works very well.

In chapter five I present in details the analysis of JET H-mode discharges that I considered for this work. A first analysis of the dataset shows that some engineering parameters cannot be considered as independent for our analysis because a lot of discharges were realized considering the same typical values of such parameters, as for example the toroidal magnetic field and the plasma current. In this way we first identify two main engineering parameters that will be used for the scaling law on the ratio between $n_{e,SEP}$ and $n_{e,PED}$, that are the plasma current I_P and the total injected power P_{TOTAL}.

Concerning general trends we have shown for example that $n_{e,SEP}$ increases while P_{TOTAL} increases, while on the separatrix temperature no clear trend is observed with respect to the increase of the power. Another interesting feature is the decrease of $n_{e,SEP}$ when B_T or I_P increase. The scaling law obtained from this first analysis shows a ratio $n_{e,SEP}$ over $n_{e,PED}$ weakly dependent from the injected power P_{TOTAL} while quite sensitive to plasma current I_P which appears at the power $\alpha \sim (-0.6)$.

As shown in figure 5.26, this first scaling laws seems to fit quite well the experimental data for low and medium values of n_{SEP}, while at high density a strong discrepancy appears. In order to get further insigth on such behaviour we have analyzed the discharges in terms of divertor magnetic configuration. The ratio betwenn n_{SEP} n_{PED} seems sensitive to the magnetic configuration as shown in figure 5.21. A clear difference is observed between experiments with a corner-corner divertor magnetic configuration with respect to the horizontal-vertical ones or vertical-vertical ones. This result suggested me to introduce a parameter taking into account the quality of H-mode, that is H_{98} parameter.

Indeed the new scaling law I obtained considering not only P_{TOTAL} and I_P but also H_{98} parameters, shows a much better agreement for all the range of pedestal densities considered in this study. Besides the H-mode operation in JET reveals a robust correlation with plasma current, $\sim I_P^{-0.58}$ and $\sim I_P^{-0.43}$, for the three different magnetic configurations, and a close correlation for TCV, $I_P^{-0.74}$. The trend that $n_{e,SEP}/n_{e,PED}$ follows on I_P and P_{TOTAL}, cardinal engineering parameters, might function as a blueprint for optimization next steps of tokamak performance, and even the parameter H_{98} that was useful for set the influence of P_{TOTAL} over $n_{e,SEP}$ can be replace for another tentative engineering parameters holding the dependence between $n_{e,SEP}$ and P_{TOT}, bringing us a new tuning tool for the tokamak operation.

Few of the main results obtained in the analysis of JET and TCV H-mode discharges are listed below:

1. From the analysis of separatrix density as a function of pedestal density (see figure 5.3), one can see that separatrix density is enclosed between 30% and 80% of top pedestal density in the JET dataset we consiedered. Such interval is in agreement with previous studies like the oneperformed by T. Leonard (see ref. [**?**]) and coauthors on DIIID tokamak. The analysis of this density ratio can be used to characterize a particle H-mode operation in a tokamak.

2. The analysis of electron temperature at the outer midplane separatrix as a function of separatrix or pedestal density (see for example figure 5.5), displays a quite scattered behaviour at low density while for higher densities the values from different discharges seem closer. Likewise the electron separatrix temperature follows a P_{SOL} dependency, theoretical 'iso-heating curves' as expected from two point model predisctions, that represents the state of heating under which some discharge is operating, and that reduce the range of $T_{e,SEP}$ while $n_{e,SEP}$ or $n_{e,PED}$ increase as is indicated in equation (2.87).

3. In the first scaling law I obtained for the ratio between $n_{e,SEP}$ and $n_{e,PED}$ using the engineering parameters P_{TOTAL} and I_P, I observed a very weak dependence from the total power. Considering the parameter H_{98}, that quantifies the quality of confinement, I recover the clear evidence of the impact of power on plasma density as shown in many figures I presented.

4. To give few results coming from the analysis with respect to magnetic divertor configuration one can mention the behaviour of separatrix electron density for Corner-Corner magnetic configuration with respect to plasma current or toroidal magnetic field. From figure 5.15 one observes the decreasing of the separatrix density with respect to top pedestal density corresponding to an increase of plasma current, indicating stronger density gradients at the edge. This behaviour is similar for all the divertor configurations but more pronounced for the corner-corner one.

5. As shown in figure 5.21, the magnetic and wall divertor configuration is associated with a different quality of H-mode plasma. This can be recasted in terms of the H_{98} parameter. On electron separatrix density it has a relevant influence because most of discharges for each one of the configurations hold a hierarchical relationship setting up that Vertical-Vertical configuration is closer to maximum limit for $n_{e,SEP}/n_{e,PED}$ while Corner-Corner configuration is closer to minimum limit, leaving Vertical-Horizontal configuration within an intermediate state. One further remark about this result is the one related to ELMs impact and exposed in [66] where a minimum limit of $n_{e,SEP}/n_{e,PED}$ is correlated to type-I ELM regime while a maximum limit is linked to grassy-ELM regime, needing a strong particle transport in the pedestal to access it.

6. Three different magnetic configurations were explored. Each one of the configurations are characterized by the striking point position as shown in figure 5.14. The striking point position will affect the pumping capability as is figured out by figure 5.20. The corner-corner conf. has the best pumping. The divertor magnetic configuration shows

a clear impact on electron separatrix density. Fixing a pedestal density the electron separatrix density increases while magnetic configuration scans the Corner-Corner, Vertical-Horizontal and Vertical-Vertical configuration respectively as is shown in figures 5.23, 5.24 and 5.25. On figure 5.25 we show the H_{98} factor versus $n_{e,SEP}/n_{e,PED}$ is independent of the magnetic [67] configuration previously considered providing us with a signal that $n_{e,SEP}/n_{e,PED}$ is a robust dimensionless parameter to match core performance with heat load on the wall of the machine. In general, the dependence of confinement on $n_{e,SEP}$ evidences that higher energy confinement is only possible at low values of $n_{e,SEP}$, $n_{e,PED}$ and $n_{e,SEP}/n_{e,PED}$, displaying a strong correlation between $n_{e,SEP}$ and H_{98} than $n_{e,PED}$ and H_{98}.

To conclude, I have explored a large dataset of H-mode plasma discharges in JET, obtaining a scaling law for the ratio between separatrix electron density and top pedestal one in terms of engineering parameters. This scaling law can be used to find and hopefully predict optimal scenarios both for core and edge plasmas, for present and future devices. Further studies have to be performed to include other devices in the scaling law and improve its predictability.

Appendix A

Drude theory of thermal conductivity applied to plasma

Following Fourier law ansatz, we should have next expression for heat flux:

$$\vec{q} = -k\vec{\nabla}T \tag{A.1}$$

For this model electrons transport heat given by collisions, and with each one of these collisions electrons transfer energy represented by temperature at the last collision electron given. Now, the variation of heat flux, $\frac{d\vec{q}}{dt}|_{total}$,would be splitted in two contributions mainly, diffusion and collisions, and it will be represented as follow:

$$\frac{d\vec{q}}{dt}|_{total} = \Big(\frac{d\vec{q}}{dt}\Big)_{diff} + \Big(\frac{d\vec{q}}{dt}\Big)_{coll} \tag{A.2}$$

· $\Big(\frac{d\vec{q}}{dt}\Big)|_{diff}$ (working with gradient of temperature where collision are neglectible.)

Considering a displacement $\vec{r}$ of electrons during a time interval $\vec{t}$ with an average velocity $\vec{v}$, so the energy at $\vec{r}$ will be represented by $\epsilon(\vec{r})$ and $\vec{r}$, $\vec{t}$ and $\vec{v}$ are related in $\vec{r} = -\vec{v}t$ where sign $-$ is due to inverse movement of electron.

The variation of energy for a particle i is given by:

$$\delta\epsilon_i = \vec{r_i} \cdot \vec{\nabla}\epsilon = \vec{r} \cdot \vec{\nabla}T\Big(\frac{\partial\epsilon}{\partial T}\Big) = -t\vec{v_i} \cdot \vec{\nabla}T\Big(\frac{d\epsilon}{dT}\Big). \tag{A.3}$$

The total energy flux is given by:

$$\vec{q}|_{diff} = \Sigma_i \vec{v_i} \delta\epsilon_i = -t\Sigma_i \vec{v_i}\Big(\vec{v_i} \cdot \vec{\nabla} T\big(\frac{d\epsilon}{dt}\big)\Big) \tag{A.4}$$

$$\begin{aligned}
\Big(\frac{d\vec{q}}{dt}\Big)_{diff} &= -\Big(\frac{d\epsilon}{dT}\Big) \cdot \Sigma_i \vec{v_i}\big(\vec{v_i} \cdot \vec{\nabla} T\big) \\
&= -\frac{d\epsilon}{dt} \cdot \frac{n\overline{v^2}}{3} \vec{\nabla} T \\
&= -\frac{d(n\epsilon)}{dt} \cdot \frac{\overline{v^2}}{3} \vec{\nabla} T \\
&= -\frac{dE}{dt} \cdot \frac{\overline{v^2}}{3} \vec{\nabla} T
\end{aligned}$$

On the other side, temporal variation of heat flux by effect of collisions could be approach considering that Coulomb collisions change direction of momentum in an time interval, τ, between two consecutive collisions, and since electrons will transfer energy by each impact so it would be a dissipative process,

$$\Big(\frac{d\vec{q}}{dt}\Big)_{coll} = \frac{-\vec{q}}{\tau}$$

Summarizing previous analysis in expression for total heat flux variation:

$$\Big(\frac{d\vec{q}}{dt}\Big)_{total} = -\Big(\frac{dE}{dt}\Big)\frac{1}{3}\overline{v^2}\vec{\nabla} T - \frac{\vec{q}}{\tau}, \tag{A.5}$$

in steady state:

$$\left.\Big(\frac{d\vec{q}}{dt}\Big)_{total} = 0\right\} \quad \vec{q} = -\frac{1}{3} c_v \overline{v^2} \tau \vec{\nabla} T \tag{A.6}$$

and taking c_v for a monoatomic gas, $c_v = \frac{3}{2} n k_B$,

$$\vec{q} = -\frac{n k_B}{2} \overline{v^2} \tau \vec{\nabla} T \tag{A.7}$$

A.1 Electric field by effect of gradient of temperature - (Seebeck effect-Drude model)

Following indications in [68], an electric current will be generated by effect of electron motion that initially was generated by effect of temperature gradient. Due to existence of gradient temperature there would be two points with extreme values of temperature, and two options appear to analyse the system, one is consider a 'closed circuit' but for this case we would need an external force to work against the system to returned an electron to the initial point. In the other case, we consider an open circuit, where by effect of accumulation of charged in the end extreme point the flux of charged will be cancelled, but remaining an electric field that will be proportional to the gradient of temperature,

$$\vec{E} = \gamma \vec{\nabla} T, \quad \gamma < 0. \tag{A.8}$$

In analogy to the past case, we will replace heat flux with electric current in the analysing. When system reach a steady state, we have:

$$\frac{d\vec{i}}{dt}|_{total} = \frac{\vec{i}_{thermal}}{dt}_{diff} + \frac{d\vec{i_E}}{dt}|_{field} = 0. \tag{A.9}$$

Assuming an electron moves a distance $\vec{r}$ during a interval time t with a velocity $\vec{v}$, where they are related as $\vec{r} = -t\vec{v}$ due to electron has an inverse motion by effect of negative charge. Considering gradient of temperature $\vec{\nabla} T$ is parallel a particular axis $\hat{x}$, so in this direction electrons will suffer a variation of velocity by effect of temperature change, and finally we'll have $\vec{\nabla} v_x || \quad \vec{\nabla} T || \quad + \hat{x}$. Calculating the excess of velocity at axis $+\hat{x}$,

$$\begin{aligned}
\delta v_x &= -t\vec{v} \cdot \vec{\nabla} v_x \\
&= -t v_x \nabla v_x \quad \text{gradient is parallel to x - axis} \\
&= -\frac{1}{2} t \nabla v_x^2 \\
&= -\frac{1}{6} t \nabla \overline{v^2},
\end{aligned}$$

$$\frac{\partial v_x}{\partial t} = -\frac{1}{6}\nabla\overline{v^2} \quad \text{using} \quad \vec{i} = nev_x\hat{x}$$
$$\hookrightarrow \Big(\frac{\partial \vec{i}}{\partial t}\Big)_{diff} = ne\frac{\partial v_x}{\partial t}\hat{x}$$
$$\Big(\frac{\partial \vec{i}}{\partial t}\Big)_{diff} = \frac{1}{6}ne\vec{\nabla}\overline{v^2}$$
$$\Big(\frac{\partial \vec{i}}{\partial t}\Big)_{diff} = \frac{1}{6}ne\frac{\partial\overline{v^2}}{\partial T}\vec{\nabla}T.$$

By effect of electric current we have:

$$\Big(\frac{\partial \vec{i}}{\partial t}\Big)_{E-field} = ne\frac{e\vec{E}}{m}, \tag{A.10}$$

in a steady state:

$$\frac{d\vec{i}}{dt}|_{total} = \frac{\vec{i}_{thermal}}{dt}_{diff} + \frac{d\vec{i_E}}{dt}|_{field} = 0. \tag{A.11}$$

$$\frac{ne^2\vec{E}}{m} = -\frac{1}{6}ne\frac{\partial\overline{v^2}}{\partial T}\vec{\nabla}T$$
$$\vec{E} = -\frac{1}{6e}\frac{\partial}{\partial T}(m\overline{v^2})\vec{\nabla}T$$
$$\vec{E} = -\frac{1}{3e}\frac{c_v}{n}\vec{\nabla}T$$

$$\vec{E} = -\frac{k_B}{2e}\vec{\nabla}T \tag{A.12}$$

A.2 Relaxation Processes

A.2.1 Momentum loss

For an initially stationary target (fixed ion), the resulting velocity in lab frame of projectile is:

$$v'_L = \Big(\Big[\frac{m_1v_1}{m_1+m_2}\Big]_{C.M.} + \frac{m_2v_1}{m_1+m_2}\cos(\varrho_c), \frac{m_2v_1}{m_1+m_2}\sin(\varrho_c)\Big)$$

Loss of x-momentum in 1 - collision is:

$$\begin{aligned}\Delta p_x &= m_1\big(v_1 - v'_{Lx}\big)\\ &= m_1 v_1\Big(1 - \Big(\frac{m_1}{m_1+m_2} + \frac{m_2}{m_1+m_2}\cos\varrho_c\Big)\Big)\\ &= p_x\frac{m_2}{m_1+m_2}\big(1-\cos\varrho_c\big)\\ &= p_x\frac{m_2}{m_1+m_2}\frac{\varrho_c^2}{2}\\ &= p_x\frac{m_2}{m_1+m_2}\frac{2b_{90}^2}{b^2}\end{aligned}$$

$$\begin{aligned}\frac{dp}{dl} &= n_2 p\int_{b_{min}}^{b_{max}}\frac{m_2}{m_1+m_2}\frac{2b_{90}^2}{b^2}2\pi b db\\ &= n_2 p\frac{m_2}{m_1+m_2}4\pi b_{90}^2\ln\Lambda\\ \frac{dp}{dt} &= \frac{v dp}{dl} = n_2 v_1^2\frac{m_1 m_2}{m_1+m_2}4\pi b_{90}^2\ln\Lambda\end{aligned}$$

The collision frequency is :

$$\begin{aligned}\nu_{mom} &= v_1\frac{1}{p}\frac{dp}{dl} = n_2 v_1\frac{m_2}{m_1+m_2}4\pi b_{90}^2\ln\Lambda\\ &= n_2 v_1\frac{m_2}{m_1+m_2}4\pi\Big(\frac{q_1 q_2}{4\pi\epsilon_0\frac{m_1 m_2}{m_1+m_2}v_1^2}\Big)^2\ln\Lambda\end{aligned}$$

and the collision time $\tau_{mom} = 1/\nu_{mom}$.

A.2.2 Thermal distribution collisions

Initial results was determined using fixed targets but actually we need to take into account Maxwellian distributions of both species. Simplified assumptions will be needed to applied in the system.

A.2.3 e $\Longrightarrow$ i collisions

Due to difference in kinetic energy of electrons and ions, we can consider ions as a background and ignore ion motion. Only distribution of electrons will be considered.

The Maxwellian electron distribution will be drifted by effect of background displacement:

$$f_e(\vec{v}) = n_e\Big(\frac{m_e}{2\pi T_e}\Big)^{3/2} \exp -\frac{m(\vec{v}-\vec{V_d})^2}{2k_BT}. \tag{A.13}$$

Remembering previous results, each electron is losing momentum to the ions with a ratio collision frequency:

$$\nu_p = n_{ni}\frac{q_e^2 q_i^2}{(4\pi\epsilon_0)^2}\frac{4\pi(m_i+m_e)}{m_i m_e^2 v_3}\ln\Lambda \tag{A.14}$$

Taking;

$$-\frac{1}{p}\frac{dp}{dt} = n_{ni}\frac{q_e^2 q_i^2}{(4\pi\epsilon_0)^2}\frac{4\pi(m_i+m_e)}{m_i m_e^2 v_3}\ln\Lambda$$
$$-\frac{dp}{dt} = \int f_e(\vec{v})\nu_p m_e \vec{v} d^3\vec{v}.$$

Only considering velocity over one direction, $\vec{V_d}$, $v_e \approx \sqrt{k_BT_e/m_e} \gg V_d$, and defining a new dimensionless variables $\vec{u} = \frac{\vec{v}}{v_e}$ and $\vec{u_d} = \frac{\vec{V_d}}{v_e}$.

the new form of Maxwell expression will be:

$$f_e = n_e\frac{1}{(2\pi)^{3/2}v_e^3}\exp -\frac{1}{2}(\vec{u}-\vec{u_d})^2$$
$$f_e = n_e\frac{1}{(2\pi)^{3/2}v_e^3}\exp -\frac{1}{2}(u^2 - 2\vec{u}\cdot\vec{u_d} + u_d^2), \quad u \gg u_d$$
$$f_e \approx n_e\frac{1}{(2\pi)^{3/2}v_e^3}\exp -\frac{1}{2}(u^2 - 2\vec{u}\cdot\vec{u_d})$$
$$f_e \approx n_e\frac{1}{(2\pi)^{3/2}v_e^3}\exp(\vec{u}\cdot\vec{u_d})\cdot\exp(-\frac{1}{2}u^2)$$
$$f_e \approx n_e\frac{1}{(2\pi)^{3/2}v_e^3}(1+\frac{\vec{u}\cdot\vec{u_d}}{1!})\exp(-\frac{1}{2}u^2)$$
$$f_e \approx n_e\frac{1}{(2\pi)^{3/2}v_e^3}(1+\vec{u}\cdot\vec{u_d})\exp(-\frac{1}{2}u^2),$$

assuming $\vec{u_d}||\hat{x}-axis$ and $f_0 = \frac{n_e}{(2\pi)^{3/2}v_e^3}e^{-u^2/2}$,

$$f_e = (1+u_x u_d)f_0. \tag{A.15}$$

The momentum loss will be:

$$\begin{aligned}
-\frac{dp_x}{dt} &= \int f_e \nu_{mom} m_e v_x d^3v \\
&= \nu_{mom}(v_t) m_e \int (1 + u_x u_d) f_0 \frac{v_e^3}{v^3} v_x d^3\vec{v} \\
&= \nu_{mom}(v_t) m_e v_d \int \frac{u_x^2}{u^3} f_0 d^3\vec{v}, \quad \text{using symmetry} \\
&= \nu_{mom}(v_t) m_e v_d \frac{1}{3} \int \frac{u_x^2 + u_y^2 + u_z^2}{u^3} f_0 d^3\vec{v} \\
&= \frac{\nu_{mom}(v_t) m_e v_d}{3} \int \frac{1}{u} f_0 d^3\vec{v} \\
&= \frac{\nu_{mom}(v_t) m_e v_d}{3} \int \frac{v_e}{v} f_0 4\pi v^2 dv \\
&= \frac{2\pi \nu_{mom}(v_t) m_e v_d v_e}{3} \int_0^\infty f_0 dv^2 \\
&= \frac{2\pi \nu_{mom}(v_t) m_e v_d v_e}{3} \int_0^\infty \frac{n_e}{(2\pi)^{3/2} v_e^3} e^{-\frac{v_x^2}{2v^2}} dv^2 \\
&= \frac{2}{3} \frac{\nu_{mom}(v_t)}{(2\pi)^{1/2}} \times p
\end{aligned}$$

The collision frequency would be

$$-p\frac{dp}{dt} = \overline{\nu_{ei}} = \frac{1}{3}\left(\frac{2}{\pi}\right)^{1/2} \nu_{mom}(v_t) \tag{A.16}$$

using previous value of $\nu_p(v_t)$,

$$\begin{aligned}
\overline{\nu_{ei}} &= \frac{1}{3}\left(\frac{2}{\pi}\right)^{1/2} n_i v_t \frac{m_i}{m_e + m_i} 4\pi \Big(\frac{q_e q_i}{4\pi\epsilon_0 \frac{m_e m_i}{m_e + m_i} v_t^2}\Big)^2 \ln \Lambda_e \\
&= \frac{1}{3}\sqrt{\frac{2}{\pi}} n_i \Big(\frac{ze^2}{4\pi\epsilon_0}\Big)^2 \frac{4\pi}{m_e^{1/2} (k_B T_e)^{3/2}} \ln \Lambda_e.
\end{aligned}$$

Applying the previous result to (A.7), we have :

$$\begin{aligned}
\kappa &= \frac{n_e k_B}{2} \frac{k_B T_e}{m_e} \cdot 3\sqrt{\frac{\pi}{2}} \frac{(4\pi\epsilon_0)^2 m_e^{1/2} (k_B T_e)^{3/2}}{n_i z^2 e^4 4\pi \ln \Lambda_e}, \quad \text{with } z n_i \approx ne, \\
&= 12 k_B \Big(\frac{\pi}{2}\Big)^{3/2} \frac{(k_B T_e)^{5/2}}{m_e^{1/2}} \frac{\epsilon_0^2}{ze^4 \ln \Lambda}
\end{aligned}$$

Bibliography

[1] H. Bufferand *et al.*, "Numerical modelling for divertor design of the west device with a focus on plasma–wall interactions," *Nuclear Fusion*, vol. 55, p. 053025, 2015.

[2] G. Ciraolo *et al.*, "H-mode west tungsten divertor operation: deuterium and nitrogen seeded simulations with soledge2d-eirene," *Nuclear Materials and Energy*, vol. 12, pp. 187–192, 2017.

[3] H. Bufferand *et al.*, "Implementation of drift velocities and currents in soledge2d–eirene," *Nuclear Materials and Energy*, vol. 12, pp. 852—-857, 2017.

[4] R. Goldston, "Reactor compatibility of the h-mode," *Plasma Phys. Control. Fusion*, vol. 38, p. 1161–1172, 1996.

[5] M. Greenwald, "Density limits in toroidal plasmas," *Plasma Phys. Control. Fusion*, vol. 44, p. R27–R80, 2002.

[6] S.I. Braginskii, "Transport processes in a plasma," *Reviews of Plasma Physics*, pp. 1–205, 1965.

[7] P.Helander and D.Sigmar, *Collisional Transport in Magnetized Plasmas*. Cambridge University Press, first edition ed., 2002.

[8] A. B. Mikhailovskii and V. S. Tsypin, "Transport equations and gradient instabilities in a high pressure collisional plasma," *Plasma Phys.*, vol. 13, p. 785, 1971.

[9] F.I. Parra, "Lecture notes for mmathphys "collisionless plasma physics"," 2017.

[10] P. Stangeby, "The plasma boundary of magnetic fusion devices, p.213."

[11] J. Balbin-Arias *et al.*, "Investigation of the dependency of jet midplane separatrix density as a function of engineering parameters," *Contributions to plasma physics*, p. e201900157, 2020.

[12] G.D. Porter *et al.*, "Characterization of the separatrix plasma parameters in diii-d," *PHYSICS OF PLASMAS*, vol. 5, no. 5, p. 1410, 1998.

[13] P.C. Stangeby *et al.*, "Identifying the location of the omp separatrix in diii-d using power accounting," *Nuclear Fusion*, vol. 55, p. 093014, 2015.

[14] A. Kallenbach *et al.*, "Edge2d modelling of edge profiles obtained in jet diagnostic optimized configuration," *Plasma Phys. Control. Fusion*, vol. 46, p. 431–446, 2004.

[15] A. Kallenbach *et al.*, "Parameter dependences of the separatrix density in nitrogen seeded asdex upgrade h-mode discharges," *Plasma Physics and Controlled Fusion*, vol. 60, p. 045006, 2018.

[16] M. Kocan *et al.*, "Impact of a narrow limiter sol heat flux channel on the iter first wall panel shaping," *Nuclear Fusion*, vol. 55, p. 033019, 2015.

[17] K. Jirakova *et al.*, "Systematic errors in tokamak magnetic equilibrium reconstruction: a study of efit++ at tokamak compass," *3rd European Conference on Plasma Diagnostics*, 2019.

[18] C.K. Tsui *et al.*, "Poloidal asymmetry in the narrow heat flux feature in the tcv scrape-off layer," *PHYSICS OF PLASMAS*, vol. 24, p. 062508, 2017.

[19] P. J. Catto and A.N. Simakov, "Drift ordered short mean free path description for magnetized plasma allowing strong spatial anisotropy," *Phys. Plasmas*, vol. 11, pp. 1–205, 2004.

[20] P. Dellar, "Drift ordered short mean free path description for magnetized plasma allowing strong spatial anisotropy," *Lecture notes for Part 1 of MMathPhys "Kinetic Theory"*, 2015.

[21] P.C. Stangeby *et al.*, "The relation between upstream density and temperature widths in the scrape-off layer and the power width in an attached divertor," *Nuclear Fusion*, vol. 50, p. 125003, 2010.

[22] F. Wagner *et al.*, "Regime of improved confinement and high beta in neutral-beam-heated divertor discharges of the asdex tokamak," *Phys. Rev. Lett.*, vol. 49, no. 19, pp. 1408–1412, 1982.

[23] P. H. Diamond and Y. Liang, "Self-regulating shear flow turbulence: A paradigm for the l to h transition," *Phys. Rev. Lett.*, vol. 72, no. 16, pp. 2565–2568, 1994.

[24] M. Keilhacker, "H-mode confinement in tokamaks," *Plasma Physics and Controlled Fusion*, vol. 29, no. 10, pp. 1401–1413, 1987.

[25] D. Swain and G. Neilson, "An efficient technique for magnetic analysis of non-circular, high-beta tokamak equilibria," *Nuclear Fusion*, vol. 22, no. 8, pp. 1015–1030, 1982.

[26] R. J. Groebner *et al.*, "Role of edge electric field and poloidal rotation in the l-h transition," *Physical Review Letters*, vol. 64, no. 25, pp. 3015–3018, 1990.

[27] A.W. Leonard *et al.*, "Compatibility of separatrix density scaling for divertor detachment with h-mode pedestal operation in diii-d," *Nuclear Fusion*, vol. 57, p. 9pp, 2017.

[28] ASDEX team, "The h-mode of asdex," *Nuclear Fusion*, vol. 29, no. 11, pp. 1959 – 2040, 1989.

[29] E.J. Doyle *et al.*, "Modifications in turbulence and edge electric fields at the l-h transition in the diii-d tokamak," *Physics of Fluids B 3*, vol. 3, no. 8, pp. 2300 – 2307, 1991.

[30] H. Bigliari and P. Diamond, "Influence of sheared poloidal rotation on edge turbulence," *Physics pf Fluids*, vol. 2, no. 1, 1990.

[31] Sanae and I. Itoh, "Model of l - to h-mode transition in tokamak," *Physical Review Letters*, vol. 60, no. 22, pp. 2276 – 2279, 1988.

[32] K. C. Shaing and J. E. C. Crume, "Bifurcation theory of poloidal rotation in tokamaks: A model for the l-h transition," *Physical Review Letters*, vol. 63, no. 21, pp. 2369 – 2372, 1989.

[33] A. B. Hassam, "Spontaneous poloidal spin-up of tokamaks and the transition to h mode," *Physical Review Letters*, vol. 66, no. 3, pp. 309 – 312, 1989.

[34] P. H. Diamond and Y. Kim, "Theory of mean poloidal flow generation by turbulence," *Physics of Fluids B*, vol. 3, no. 7, pp. 1626 – 1633, 1991.

[35] B. A. Carreras and V. E. Lynch, "Electron diamagnetic effects on the resistive pressure-gradient-driven turbulence and poloidal flow generation," *Physics of Fluids B*, vol. 3, no. 6, pp. 1438 – 1444, 1991.

[36] M. Keilhacker *et al.*, "Confinement and beta-limit studies in asdex h-mode discharges," *Plasma Phys. and Contr. Nucl. Fus. Res.*, vol. 1, p. p.71, 1994.

[37] C. Paz-Soldan *et al.*, "Plasma performance and operational space without elms in diii-d," *Plasma Physics and Controlled Fusion*, vol. 63, p. 083001, 2021.

[38] G.P. Maddison *et al.*, "Plasma performance and operational space without elms in diii-d," *Plasma Physics and Controlled Fusion*, vol. 44, p. 1937–1952, 2002.

[39] D. C. McDonald *et al.*, "Recent progress on the development and analysis of the itpa global h-mode confinement database," *Nuclear Fusion*, vol. 47, p. 147, 2007.

[40] M. Jakobs *et al.*, "Fusion burn equilibria sensitive to the ratio between energy and helium transport," *Nuclear Fusion*, vol. 54, p. 122005, 2014.

[41] SPCwiki, "Scaling laws."

[42] ITER Physics Expert Groups on Confinement and Transport, "Chapter 2: Plasma confinement and transport," *Fusion Engineering and Design*, vol. 39, p. 2175, 1999.

[43] A. C. C. Sips, "Chapter 2: Plasma confinement and transport," *Fusion Engineering and Design*, vol. 47, p. A19, 2005.

[44] B. N. Sorbom *et al.*, "Recent progress on the development and analysis of the itpa global h-mode confinement database," *Fusion Engineering and Design*, vol. 100, pp. 378–405, 2015.

[45] A. M. Garofalo *et al.*, "Access to sustained high-beta with internal transport barrier and negative central magnetic shear in diii-d," *Fusion Engineering and Design*, vol. 13, p. 056110, 2006.

[46] J. Mlynar, "Focus on: Jet. efd-r(07)01."

[47] CEA website, "https://www-fusion-magnetique.cea.fr/gb/cea/jet/jet.htm."

[48] J.D. Jackson, *Classical Electrodynamics*. John Wiley & Sons, Inc, third edition ed., 1998.

[49] I.H. Hutchinson, *Principles of Plasma Diagnostics*. Cambridge University Press, second edition ed., 2005.

[50] Institute of Plasma Physics of the CAS, "Thomson scattering diagnostics."

[51] H. Murmann *et al.*, "The thomson scattering systems of the asdex upgrade tokamak," *Rev. Sci. Instrum.*, vol. 63, pp. 4941—-4943, 1992.

[52] T. N. Carlstrom *et al.*, "Design and operation of the multipulse thomson scattering diagnostic on diii-d," *Rev. Sci. Instrum.*, vol. 63, pp. 4901—4906, 1992.

[53] F. Orsitto *et al.*, "Thomson-scattering diagnostic on the frascati tokamak upgrade," *APPLIED OPTICS*, vol. 34, no. 15, pp. 2712 – 2720, 1995.

[54] T. N. Carlstrom *et al.*, "The multipulse thomson scattering diagnostic on the diii-d tokamak," *The 14th IEEE/NPSS Symposium Fusion Engineering*, vol. 2, pp. 1195–1198, 1991.

[55] M.A. Makowski *et al.*, "The scaling of the heat flux width in diii-d," *Journal of Nuclear Materials*, vol. 438, p. S208–S211, 2013.

[56] H.J. Sun *et al.*, "Study of near scrape-off layer (sol) temperature and density gradient lengths with thomson scattering," *Plasma Phys. Control. Fusion*, vol. 57, p. 125011, 2015.

[57] M. Day *et al. Contrib. Plasma Phys.*, vol. 36, p. 419, 1996.

[58] A. Kallenbach *et al.*, "Multi-machine comparisons of h-mode separatrix densities and edge profile behaviour in the itpa sol and divertor physics topical group," *Journal of Nuclear Materials*, p. 337–339, 2005.

[59] Eurofusion-Openwiki, "List of Recommended Signals."

[60] PL. Spitzer Jr., *Physics of Fully Ionized Gases.* Dover Publications Inc., second edition ed., 2006.

[61] L. Spitzer and R. Harm *Phys. Rev.*, vol. 89, p. 977, 1953.

[62] S.C. Robert *et al. Phys. Rev.*, vol. 80, p. 230, 1950.

[63] S.K. Erents *et al. JET–P*, vol. 98, p. 35, 1998.

[64] V. A. Soukhanovskii *et al. J. Nuc. Mater.*, vol. 475, pp. 337–339, 2005.

[65] W. Fundamenski *Fusion Sci. Technol.*, vol. 53, p. 1023, 2008.

[66] G.S. Xu *et al. Physical Review Letters*, vol. 122, p. 255001, 2019.

[67] W. Suttrop *et al. PHYSICS OF PLASMAS*, vol. 9, p. 2103, 2002.

[68] De Groot, "Thermodynamics of irreversible processes, p.143."